

REPORT DOCUMENTATION PAGE

1a. REPORT SECURITY CLASSIFICATION Unclassified			1b. RESTRICTIVE MARKINGS	
2a. SECURITY CLASSIFICATION AUTHORITY			3. DISTRIBUTION/AVAILABILITY OF REPORT Approved for public release; distribution is unlimited.	
2b. DECLASSIFICATION/DOWNGRADING SCHEDULE				
4. PERFORMING ORGANIZATION REPORT NUMBER(S)			5. MONITORING ORGANIZATION REPORT NUMBER(S)	
6a. NAME OF PERFORMING ORGANIZATION Naval Postgraduate School		6b. OFFICE SYMBOL (If applicable) 35	7a. NAME OF MONITORING ORGANIZATION Naval Postgraduate School	
6c. ADDRESS (City, State, and ZIP Code) Monterey, CA 93943-5000			7b. ADDRESS (City, State, and ZIP Code) Monterey, CA 93943-5000	
8a. NAME OF FUNDING/SPONSORING ORGANIZATION		8b. OFFICE SYMBOL (If applicable)	9. PROCUREMENT INSTRUMENT IDENTIFICATION NUMBER	
8c. ADDRESS (City, State, and ZIP Code)			10. SOURCE OF FUNDING NUMBERS	
			Program Element No	Project No
			Task No.	Work Unit Accession Number
11. TITLE (Include Security Classification) MODELING THE TROPICAL OCEAN RESPONSE TO WESTERLY WIND FORCING				
12. PERSONAL AUTHOR(S) Claudia S. Whitney				
13a. TYPE OF REPORT Master's Thesis		13b. TIME COVERED From To	14. DATE OF REPORT (year, month, day) December 1992	15. PAGE COUNT 133
16. SUPPLEMENTARY NOTATION The views expressed in this thesis are those of the author and do not reflect the official policy or position of the Department of Defense or the U.S. Government.				
17. COSATI CODES			18. SUBJECT TERMS (continue on reverse if necessary and identify by block number)	
FIELD	GROUP	SUBGROUP	Oceanography, Numerical Modeling, Tropical Air-Sea Interaction, Westerly Wind Events	
19. ABSTRACT (continue on reverse if necessary and identify by block number)				
<p>A primitive equation ocean general circulation model, with mixed layer physics, has been developed and applied to an investigation of the equatorial ocean. The major physical problem addressed with this model is the response of the upper ocean to westerly wind events, such as those that occur during tropical cyclones and during El Nino events.</p> <p>In the model development phase, several configurations of the mixed layer physics, domain size, and wind stress were tested. The best overall simulations were produced when both Richardson number-dependent mixing and a bulk mixed layer model were included. Small model domains were found to be especially sensitive to the prescribed lateral boundary conditions and wind stress. Smaller domains required more realistic wind stress fields in order to achieve reasonable current structures. In addition, the off-equatorial currents were particularly responsive to changes in the zonal gradient of the wind stress. The final configuration of the model produces realistic simulations of climatological three-dimensional temperature and current structures in the equatorial ocean.</p> <p>In the model application phase, synoptically varying winds for the tropical Pacific were used to force the model. The winds came from the Navy's Operational Global Atmospheric Prediction System's (NOGAPS) daily analyses for the 1991-92 El Nino, which included several strong westerly wind events. The strong temporal and spatial variability in these winds produced complex fluctuations of the model's temperatures, currents, and internal waves, including reversals of the South Equatorial Current and equatorially trapped Kelvin waves. Model verification was performed by comparison with an observational study of in situ equatorial Pacific buoy data. This comparison showed that synoptic scale variations in the wind stress are needed to simulate the ocean's strong response to westerly wind events.</p>				
20. DISTRIBUTION/AVAILABILITY OF ABSTRACT <input checked="" type="checkbox"/> UNCLASSIFIED/UNLIMITED <input type="checkbox"/> SAME AS REPORT <input type="checkbox"/> OTIC USERS			21. ABSTRACT SECURITY CLASSIFICATION Unclassified	
22a. NAME OF RESPONSIBLE INDIVIDUAL J. T. Murphree			22b. TELEPHONE (Include Area code) (408) 646-2723	22c. OFFICE SYMBOL MR/Me

Approved for public release; distribution is unlimited.

Modeling the Tropical Ocean
Response to
Westerly Wind Forcing

by

Claudia S. Whitney
Lieutenant, United States Navy
B.S., University of California, Irvine, 1985

Submitted in partial fulfillment
of the requirements for the degrees of

MASTER OF SCIENCE IN METEOROLOGY
and
MASTER OF SCIENCE IN PHYSICAL OCEANOGRAPHY

from the

XXXX XXXXX

ABSTRACT

A primitive equation ocean general circulation model, with mixed layer physics, has been developed and applied to an investigation of the equatorial ocean. The major physical problem addressed with this model is the response of the upper ocean to westerly wind events, such as those that occur during tropical cyclones and during El Niño events.

In the model development phase, several configurations of the mixed layer physics, domain size, and wind stress were tested. The best overall simulations were produced when both Richardson number dependent mixing and a bulk mixed layer model were included. Small model domains were found to be especially sensitive to the prescribed lateral boundary conditions and wind stress. Smaller domains required more realistic wind stress fields in order to achieve reasonable current structures. In addition, the off-equatorial currents were particularly responsive to changes in the zonal gradient of the wind stress. The final configuration of the model produces realistic simulations of climatological three-dimensional temperature and current structures in the equatorial ocean.

In the model application phase, synoptically varying winds for the tropical Pacific were used to force the model. The

1/20/15
W 5625
C.1

winds came from the Navy's Operational Global Atmospheric Prediction System's (NOGAPS) daily analyses for the 1991-92 El Niño, which included several strong westerly wind events. The strong temporal and spatial variability in these winds produced complex fluctuations of the model's temperatures, currents, and internal waves, including reversals of the South Equatorial Current and equatorially trapped Kelvin waves. Model verification was performed by comparison with an observational study of in situ equatorial Pacific buoy data. This comparison showed that synoptic scale variations in the wind stress are needed to simulate the ocean's strong responses to westerly wind events.

TABLE OF CONTENTS

I.	INTRODUCTION	1
A.	EQUATORIAL OCEAN DYNAMICS	1
B.	ENSO AND WESTERLY WIND EVENTS	5
C.	TROPICAL OCEAN MODELING	8
II.	MODEL FUNDAMENTALS	12
III.	RESULTS	21
A.	MODEL DEVELOPMENT	21
1.	Development Run DN	22
2.	Development Run DR	23
3.	Development Run DM	25
4.	Development Run DRM	25
5.	Development Run DRM2	27
6.	Development Run DNL	29
7.	Development Run DRML	30
8.	Development Runs Summary	32
B.	MODEL EXPERIMENTS	32
1.	Experiment 1 (E1)	33
2.	Experiment 2 (E2)	36
3.	Experiment 3 (E3)	38
4.	Experiment 4 (E4)	40

5. Experiments Summary	44
IV. SUMMARY	109
A. DISCUSSION	109
B. CONCLUSIONS	112
C. RECOMMENDATIONS	113
APPENDIX	119
A. EXPERIMENT 1 WIND STRESS CODE	119
B. EXPERIMENT 2 WIND STRESS CODE	119
C. EXPERIMENT 3 WIND STRESS CODE	120
REFERENCES	121
INITIAL DISTRIBUTION LIST	125

I. INTRODUCTION

A. EQUATORIAL OCEAN DYNAMICS

The importance of the tropics in the general circulation of the atmosphere has long been recognized. In the tropics, incoming solar radiation exceeds outgoing solar radiation producing a net gain of energy in this region (Gill, 1982). The transport of excess energy towards the poles, where there is a net loss of energy, is a major factor determining our weather and climate (Gill, 1982). The oceans play a major role in this energy transport from the tropical regions towards the poles, and thus have a significant influence on our global climate (Gill, 1982).

As the atmospheric and oceanic processes influencing climate do not occur in isolation, the importance of tropical air-sea interaction is fundamental to global weather and climate. Continuous feedbacks between the atmosphere and the ocean make the coupling between the oceanic mixed layer and the atmospheric planetary boundary layer a very complex process. Chu and Garwood (1990) discuss both positive and negative feedback mechanisms between clouds and the oceanic mixed layer. Clouds reduce incoming solar radiation at the sea surface, causing a relative decrease in the sea surface temperature. A decrease in the sea surface temperature

increases mixed layer entrainment which cools the mixed layer. Cooling of the mixed layer reduces the evaporation rate and reduces the clouds. This is a negative feedback mechanism. Precipitation reduces the surface salinity which stabilizes the upper ocean and reduces mixed layer deepening. As the mixed layer shallows, energy becomes concentrated in a thinner layer which increases the sea surface temperature. The rise in sea surface temperature enhances evaporation which produces more clouds and precipitation. This is a positive feedback mechanism.

Air-sea interaction includes not only the exchange of energy between the atmosphere and ocean, but also the exchange of momentum and moisture. In the tropical regions, significant heat, momentum and moisture fluxes between the atmosphere and the ocean occur. In the tropical western Pacific, major momentum fluxes occur during westerly wind events.

The tropical western Pacific is an area where large poleward transports of heat occur in the ocean and large releases of latent heat occur in the atmosphere. These large transports and releases of heat play a key role in our global weather and climate. In addition, the tropical Pacific Ocean has been identified as the predominant basin in the El Niño Southern Oscillation (ENSO) phenomenon (Webster and Lukas, 1992). This study will concentrate on one facet of tropical air-sea interaction: the effect of momentum fluxes in the

form of westerly wind events on the upper ocean, including the oceanic mixed layer.

The fundamentals of ocean mixed layer mechanics are more easily understood from a one-dimensional perspective. Deepening of the mixed layer can occur due to either dynamical (e.g., wind mixing) or thermodynamical (e.g., sea surface cooling) processes. Shallowing of the mixed layer often occurs through sea surface heating which reduces turbulent mixing and entrainment. Shallowing may also occur when precipitation exceeds evaporation, because a net fresh water influx will decrease the surface salinity and density, and thus, increase the near-surface stability. Over the equatorial oceans, there is, on average, a net downward heat flux and a westward wind stress (Gill, 1982; Trenberth et al., 1989; Stricherz et al., 1992).

From a three-dimensional perspective, the general ocean circulation also plays an extensive role in determining the properties of the mixed layer. In the equatorial region, a typical westward wind stress imposed on the sea surface will cause an Ekman transport of water to the north in the northern hemisphere and to the south in the southern hemisphere. This net horizontal divergence of water away from the equator will cause upwelling at the equator in order to preserve continuity. Thus, in the absence of advective and moisture fluxes, the dynamics and thermodynamics work to shallow the mixed layer.

Another important factor in the tropical ocean circulation is that the Coriolis parameter vanishes at the equator. Thus, the geostrophic approximation, which dominates in the extra-equatorial oceans, is altered at the equator. Consequently, the dominant balance in the momentum equations is more complex and includes non-linear advection. In addition, high frequency motions can be especially important in the equatorial oceans (e.g., diurnal processes in the mixed layer [Garwood et al., 1989]).

All of these elements contribute to making the equatorial ocean circulation a very complex phenomenon. The mixed layer response to each of these elements can be quite difficult to determine due to the numerous factors which can come in to play. Garwood et al. (1985) concluded that, for a one-dimensional, steady state, non-entraining mixed layer, equatorial mixed layer depth decreases in response to westerly winds and increases in response to easterly winds. Additionally, Garwood et al. (1985) proposed that the interaction between planetary rotation and the zonal wind stress contributes to the deep mixed layer in the central equatorial Pacific Ocean. However, the mixed layer response to various localized wind forcings can be obscured by buoyancy damping as well as Ekman pumping and other large scale events, such as ENSO.

B. ENSO AND WESTERLY WIND EVENTS

The ENSO phenomenon is a very complex sequence of air-sea interaction events. While many theories have been proposed to explain ENSO, a single comprehensive theory does not yet exist. One aspect of ENSO involves a weakening of the surface pressure gradient between Darwin and Tahiti, with the pressure at Darwin increasing and the pressure at Tahiti decreasing. This results in a relaxation in the westward trade winds, which allows the deep warm pool of water in the western Pacific to move eastward. The mixed layer deepens in the central and eastern Pacific and the thermocline tilt (upward to the east) is reduced (Philander, 1981). The effects of ENSO are more well known than its causes. However, westerly wind bursts are thought to play an important role in the ENSO phenomenon (Harrison and Giese, 1991).

The concept of westerly wind bursts was first introduced to describe anomalous low level synoptic scale westerly winds along the equator in the western Pacific (Riehl, 1979). The westerly burst concept has since been expanded to include periods of weakened easterlies (Luther et al., 1983). An abrupt change in the wind magnitude from strong easterlies to weak easterlies (i.e. a westerly wind anomaly with respect to the mean) may also produce the same type of effects as a period of actual westerly winds (Luther et al., 1983).

The views on the origin of westerly wind bursts are quite varied. One proposed source is extratropical forcing in the

form of a southward shift of the Siberian anticyclone that induces pressure rises in the western Pacific (Chu, 1988). Trade wind surges in the northern hemisphere that push the intertropical convergence zone south of 10°S also produce westerly winds, as the northern trades recurve after crossing the equator (Riehl, 1979). In addition, westerly winds are clearly created when a pair of tropical cyclones develop on opposite sides of the equator (Keen, 1982). However, episodes of westerlies along the equator may also precede or follow tropical cyclone occurrences without being closely connected in time (Harrison and Giese, 1991).

As pointed out by Murakami (1989), westerly events are not uncommon occurrences. Rasmusson and Carpenter (1982) have shown that westerly wind bursts are more common during ENSO periods. Westerly wind events may occur with such frequency that they are a significant factor in the near equatorial zonal wind variability and contribute significantly to the observed monthly mean wind variations associated with ENSO (Harrison and Giese, 1991).

The direct and indirect effects of westerly wind bursts are topics of active research. The observed remote eastern Pacific sea level and ocean current response to a westerly wind event in the western Pacific have been examined by McPhaden et al. (1988). The remote response has also been explored in terms of ocean general circulation models with forcing centered both on and off the equator (Harrison and

Giese, 1988; Giese and Harrison, 1990; Giese and Harrison, 1991). Keen (1982) has proposed that a single westerly wind event, created by a cross-equatorial cyclone pair, may trigger the onset of an ENSO event. In addition, Giese and Harrison (1990) have suggested that a series of westerly wind events may, through their cumulative effects, have an important influence on the initiation and perpetuation of an ENSO event.

Wyrkti (1975) first suggested that a relaxation in the easterly trades, i.e., a westerly event, may cause warming in the eastern Pacific associated with ENSO. McCreary (1976) showed in a modeling study that synoptic scale westerly wind bursts over the western Pacific may excite oceanic Kelvin waves which propagate eastward across the Pacific reaching the coast of South America in two to three months. Cooper (1992) found in an observational study of the 1991-92 ENSO that westerly wind events produced distinct local and remote responses. The local responses included a reversal in the South Equatorial Current, downwelling, and deepening of the thermocline. The remote responses included excitation of an equatorial Kelvin wave. Horizontal advection of the ambient sea surface temperature gradient due to anomalous surface currents associated with Kelvin waves has been suggested as one method of raising the sea surface temperature in the eastern Pacific (Harrison and Schopf, 1984). An alternate mechanism to raise the sea surface temperature is the downwelling associated with Kelvin waves and the associated

reduction of entrainment at the base of the mixed layer (McCreary, 1983). While the precise connection between westerly wind episodes and the sea surface temperature anomalies during an El Niño event is not clearly understood, westerly wind events are clearly important for understanding tropical air-sea interaction.

C. TROPICAL OCEAN MODELING

One method for developing this understanding is the use of numerical models of the ocean and atmosphere. There have been many modeling efforts applied to the ocean over the past several decades, only a few of which will be discussed here. Various types of models (e.g., level, layer) with various types of coordinate systems (e.g., depth, isopycnal) have been applied to the tropical oceans. Additionally, there have been many studies of the ocean's response to the wind.

Haney (1974) developed a primitive equation model that spanned the equator and was forced by asymmetric winds and thermal fluxes. His model satisfactorily simulated midlatitude western boundary currents, an equatorial undercurrent, and a northern equatorial countercurrent. Cane (1979) developed a primitive equation beta-plane model to study the wind-driven circulation in an equatorial ocean. He determined that the non-linear response to zonal winds involved an eastward equatorial undercurrent. Additionally, Cane concluded that easterly winds cause a basin-wide zonal

pressure gradient affiliated with the undercurrent in which the dynamics are non-local. He also concluded that westerly winds induce local dynamics coupled to the sub-surface eastward flow.

Semtner and Holland (1980) used a 14 level, eddy-resolving primitive equation model to study the turbulent equilibrium of an equatorial ocean forced by steady zonal winds. Their results showed realistic mean flows and eddy structures, including an equatorial undercurrent with mean velocities as large as 120 cm/s and a net transport of 28 Sverdrups (Sv). Schopf and Cane (1983) utilized a primitive equation model with a mixed layer parameterization to study the interaction between dynamics and mixed layer physics in the equatorial ocean utilizing simple wind stresses and surface heating patterns. They found that surface heating inhibits mixed layer deepening and prevents momentum mixing uniformly to the main thermocline. They concluded that the maintenance of this stratification by surface heating is important in maintaining a strong and distinct equatorial undercurrent.

Latif (1987) demonstrated the importance that the total wind field plays in a primitive equation model. His model showed a strong sensitivity to the choice of the wind field when forced with either objectively or subjectively analyzed winds. Similarly, Gordon and Corry (1991) showed significant sensitivity of modeled near-surface conditions to the choice of surface heat and momentum fluxes. They compared their

ocean model's response to climatological fluxes and fluxes generated by an atmospheric general circulation model.

As westerly wind events are fundamentally a near-surface tropical feature, the modeling efforts which are of most interest are those that focus on the tropical upper ocean. Recently, Miller et al. (1992) applied a layered general circulation model, with an isopycnal vertical coordinate and an embedded bulk surface mixed layer model, to the tropical Pacific. The model reproduced the major climatological features of the ocean. In addition, it gave reasonable simulations of certain features of the sea surface temperature, sea level, and near-surface velocity anomalies. Zhang and Endoh (1992) applied a free surface general circulation model, formulated with a sigma vertical coordinate and without the rigid lid approximation, to the tropical Pacific Ocean. Their model simulated major features of the observed thermal structure, general circulation, and sea level.

The focus of this research is to examine the upper ocean response to westerly wind events. The relationship between westerly wind events and downwelling, Kelvin waves, and upper ocean temperature and current responses are of particular interest. One unique feature of this research includes the use of an ocean general circulation model with explicit mixed layer physics to address the impact of both idealized and realistic wind stresses on equatorial dynamics. Realistic

synoptic variability in the winds is obtained by incorporating the wind stress perturbations for a three month period during the 1991-92 ENSO that includes several westerly wind events. This study explores the upper ocean temperature and current responses to this time and space varying wind stress to better understand tropical air-sea interactions in general, and westerly wind events interactions in particular.

This study has two goals. The first goal is to develop a numerical ocean general circulation model with complete mixed layer physics for use in tropical air-sea interaction studies. The second goal is to understand the effects of synoptic scale westerly wind events on the upper equatorial ocean through numerical modeling techniques. Chapter II presents the fundamentals of the numerical model. Chapter III addresses model development, model applications and results. Chapter IV presents discussion, conclusions, and suggestions for further research and investigation.

II. MODEL FUNDAMENTALS

The model used in this study is a primitive equation multi-level ocean general circulation model (OGCM) with an embedded bulk mixed layer model. The OGCM is based on the work by Haney (1974) in which he used a 6-level primitive equation based model to study the ocean response to large-scale heat and momentum fluxes.

The mixed layer model embedded within the general ocean circulation model is fundamentally the Garwood (1977) model, developed from the turbulent kinetic energy equation. The mixed layer is the fully turbulent region below the sea-air interface, and is vertically homogeneous (i.e., the values of temperature and horizontal velocity are vertically uniform). Mixed layer conditions may be changed by advection. Additionally, the mixed layer may deepen or shallow as entrainment increases or decreases. When the mixed layer shallows, the temperature profile is adjusted to conform with the fixed level structure of the general ocean circulation model. This adjustment conserves heat, momentum, and potential energy.

In the formulation of the mixed layer model, the water column beneath the mixed layer is assumed to be dynamically stable while the turbulent mixed layer is dynamically unstable. Dynamic stability is ensured beneath the mixed

layer by forcing vertical fluxes of heat and momentum between model levels in order to prevent the gradient Richardson number from becoming less than the critical value of 0.25. These fluxes are assumed to be equally efficient at mixing heat and momentum.

Adamec et al. (1981) first integrated Haney's OGCM and Garwood's mixed layer model to create an ocean circulation model with an embedded mixed layer. Meaningful communication between the fixed-level, dynamic portion of the model and the mixed layer portion of the model is critical and is accomplished in two phases. First, upper ocean advective and diffusive change are calculated dynamically and converted to input for the mixed layer model. Second, the mixed layer model computes changes in mixed layer temperature, velocity, and depth due to surface fluxes and entrainment and transfers the information back to the dynamic portion of the model. See Adamec et al. (1981) for a more complete description of the embedding techniques.

In this study, the model of Adamec et al. (1981) has been adapted to the equatorial region. The basic model assumptions include:

- the ocean is hydrostatic and incompressible
- density is a linear function of temperature only
- vertical velocity is zero at the ocean's surface and bottom
- vertically averaged motion is zero

Consequently, there is no barotropic mode, and salinity effects on density are neglected. Additionally, the subgrid scale horizontal turbulent fluxes of both heat and momentum are parameterized using constant eddy coefficient formulations beneath the ocean mixed layer. Laplacian diffusion is used in the horizontal momentum and temperature tendency equations with the forms:

$$A_m \nabla^2 u, \quad A_m \nabla^2 v, \quad A_h \nabla^2 T.$$

The vertical turbulent fluxes of heat and momentum are also parameterized using eddy viscosity and conductivity coefficients:

$$\overline{w'u'} = -k_m \frac{\partial u}{\partial z}, \quad \overline{w'v'} = -k_m \frac{\partial v}{\partial z}, \quad \overline{w'T'} = -k_h \frac{\partial T}{\partial z}.$$

The model domain configuration is depicted in Figure 2.1. The domain is rectangular in the horizontal plane, with variable latitudinal and longitudinal extents. The model is nearly symmetric about the equator. Zonal grid spacing is 50 km, and meridional grid spacing is 25 km. No grid points occur on the equator. The model has 15 unequally spaced levels at depths extending from 10 m to 3500 m, with greater resolution in the upper ocean. The ocean bottom and sides are prescribed as flat.

The lateral boundary conditions for momentum are no slip along the eastern and western boundaries and free slip along the northern and southern boundaries. The lateral boundary

conditions for heat are no diffusion across the eastern and western boundaries and diffusion into the northern and southern boundaries. Additionally, there are no vertical fluxes of mass, momentum, or heat at the bottom.

Figure 2.2 depicts a schematic representation of the embedded mixed layer. The variable, ζ , represents u, v or T . If the base of the mixed layer lies within the k^{th} model level, the value of ζ in the mixed layer portion is denoted ζ_1 ; the value just below the mixed layer is denoted ζ_2 ; the integrated average over the model level is $\bar{\zeta}$; mixed layer depth is denoted h (Adamec et al., 1981).

The model is initiated from a state of rest with an initial temperature field that is horizontally uniform and has the vertical profile used by Semtner and Holland (1980):

$$T(z) = 4.0 + 20.0(e^{-\frac{z}{500\text{ m}}}).$$

Figure 2.3 depicts this initial temperature profile. The main thermocline lies in the upper 500 m.

The two key forcings used to drive the model are wind stress and surface heat flux. The initial model development process was conducted using a uniform westward wind stress, constant in space and time, with a magnitude of 0.6 dyns/cm^2 . Additional wind stress fields were used in the model experiment phase, as described in Chapter III. The surface heat flux is proportional to the air-sea temperature

difference, following the Haney formulation (1971). The net downward heat flux, Q , is prescribed by

$$Q = \gamma (T_a - T_s)$$

where

- γ = heat flux coefficient ($\text{W m}^{-2} \text{ } ^\circ\text{C}^{-1}$)
- T_a = constant air temperature ($^\circ\text{C}$)
- $T_s(x, y, 10\text{m}, t)$ = sea surface temperature ($^\circ\text{C}$)

A constant air temperature of 25°C is prescribed over the model domain. The sea surface temperature is given by the calculated model temperature at 10 m (i.e., at the first level of the model).

Time stepping is done with a leapfrog scheme, with an Euler backwards scheme applied every eleven time steps to prevent solution separation in time. In addition, the numerical scheme uses an Arakawa B grid to implement the spatial finite differencing. The key model parameters and their values are given in Table 2-1. For additional details about the combined OGCM and embedded mixed layer model, see Adamec et al. (1981).

TABLE 2-1. MODEL PARAMETERS

Parameter	Symbol	Value	Units
east-west grid spacing	dx	50	km
north-south grid spacing	dy	25	km
time step	dt	600	s
heat flux coefficient	γ	6.94×10^{-4}	$\text{Wm}^{-2}\text{ }^{\circ}\text{C}^{-1}$
horizontal eddy viscosity	A_h	5.0×10^7	cm^2s^{-1}
vertical eddy viscosity	k_v	1.0	cm^2s^{-1}
horizontal eddy conductivity	A_h	1.0×10^7	cm^2s^{-1}
vertical eddy conductivity	k_v	1.0	cm^2s^{-1}
thermal expansion coefficient	α	3.0×10^{-4}	cm^2s^{-1}
reference density	ρ	1.0276	gm cm^{-3}

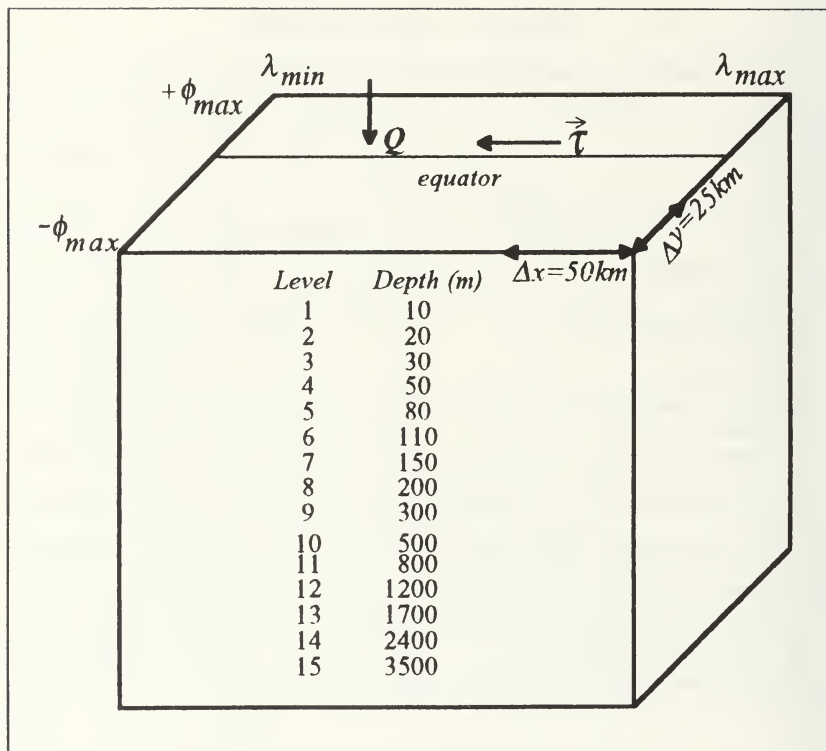


Figure 2.1. Model domain schematic:

$+\phi_{max}$ and $-\phi_{max}$ are the north and south latitudinal boundaries.
 λ_{max} and λ_{min} are the east and west longitudinal boundaries.

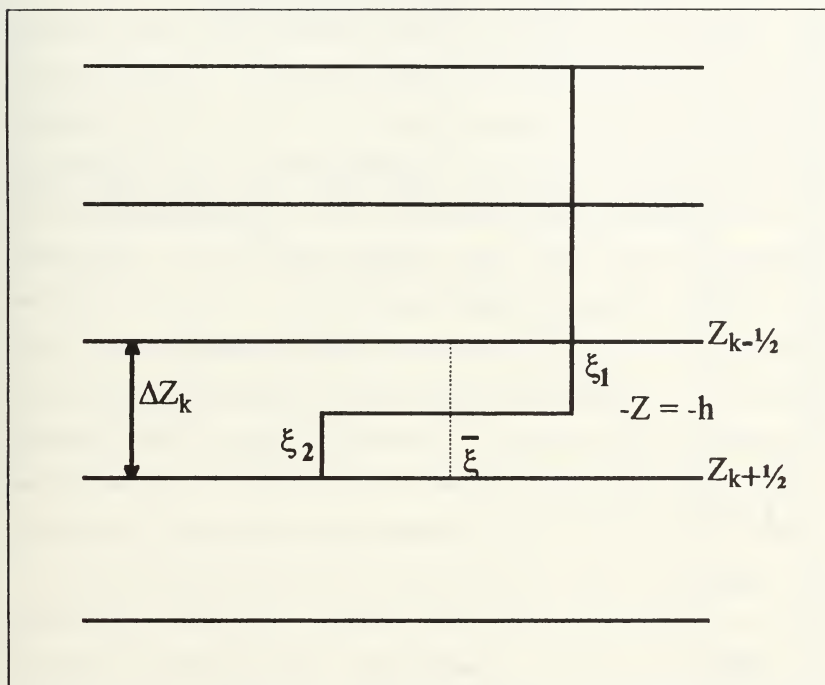


Figure 2.2. Schematic illustration of the embedded mixed layer: depth h , located within the k th level of the circulation model (after Adamec et al., 1981).

INITIAL TEMPERATURE PROFILE

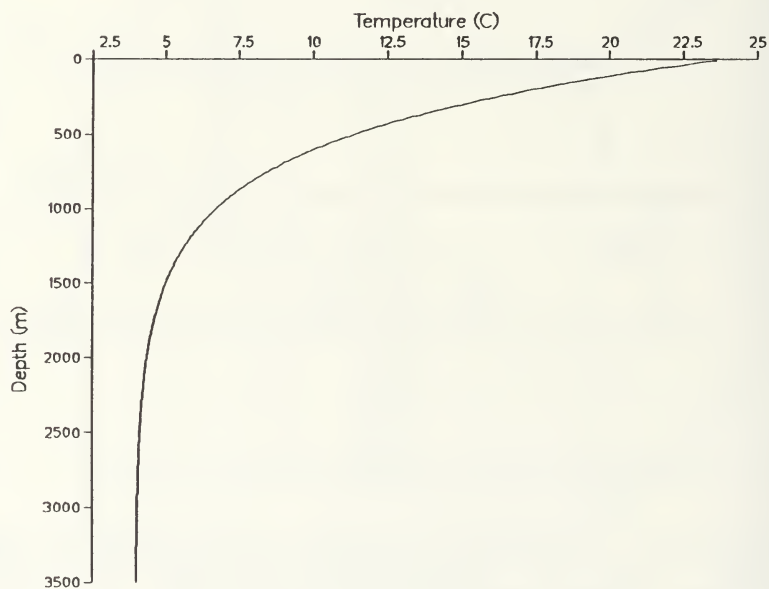


Figure 2.3. Initial temperature profile.

III. RESULTS

A. MODEL DEVELOPMENT

Various domain sizes as well as combinations of model physics were investigated during the model development and spin up stages. Two domain sizes were used. A small domain extended from 10°S to approximately 10°N and spanned approximately 30° of longitude. A larger domain extended from 20°S to approximately 20°N and spanned approximately 60° of longitude. The small domain was used for the initial development runs. Richardson number-dependent mixing and mixed layer dynamics were the principal physical processes that were investigated during model development. A uniform westward wind stress, constant in space and time, with a magnitude of 0.6 dyns/cm^2 was used for all development runs. A summary of the model development runs is given in Table 3-1.

At the beginning of the developmental phase, the model was numerically unstable. Thus, the model was reduced to its simplest configuration, development run DR, in order to identify and correct the problems. Complexity was progressively added to the model, in the form of Richardson number-dependent mixing and mixed layer physics. The large domain developmental runs were performed to determine the

effects of the limited longitudinal and latitudinal extent of the small domain.

Table 3-1. DEVELOPMENT RUNS SUMMARY

Development Run	Richardson No. Mixing	Mixed Layer Physics	Domain Size	Initial State	Days
DN	Off	Off	Small	Rest	0 - 360
DR	On	Off	Small	DN Day 360	360 - 720
DM	Off	On	Small	DN Day 360	360 - 361
DRM	On	On	Small	Dn Day 360	360 - 361
DRM2	On	On	Small	Rest	360 - 361
DNL	Off	Off	Large	Rest	0 - 360
DRML	On	On	Large	Rest	0 - 360

1. Development Run DN

During the initial 360-day spin up model run, neither Richardson number-dependent mixing nor mixed layer mixing were included. Thus, the model was executed only as a general ocean circulation model. Initiated from a state of rest, development run DN was carried out to model day 360, by which time it had achieved a steady-state condition with numerical stability. At day 360, double cold tongues, symmetric about the equator, were evident at 10 m (Figure 3.1). The corresponding horizontal currents at day 360 (Figure 3.1)

showed strong westward flow diverging away from the equator. Wave features, along the poleward flanks of the cold tongues, formed in the eastern basin and propagated westward during the 360 day model run. Along the equator the westward currents were confined to the upper 20 m, as shown in Figure 3.2. Additionally, there was a slight decrease in the depth of the westward currents from west to east. Figure 3.3 shows a strong return flow by the equatorial undercurrent (EUC) beneath the westward surface currents. The EUC extended down to about 250 m in the west and 80 m in the east, with its core at about 20 m. Figure 3.3 shows westward currents symmetric about the equator and extending from the surface to about 150 m with relative maxima centered at approximately 30 m. Along the equator, the main thermocline shallowed from west to east as shown in Figure 3.4. The isotherms in Figure 3.5 indicate upwelling beneath the double cold tongues.

2. Development Run DR

After the initial 360 day spin up stage, additional physics were included in the model. Richardson number-dependent mixing was performed if the calculated Richardson number was less than the critical Richardson number of 0.25. Development run DR was initialized from day 360 of development run DN and was run for an additional 360 days to day 720. At day 720, the model fields had achieved a steady state and a single cold tongue was present near the surface along the

equator, emanating from the eastern boundary and protruding westward across the basin (Figure 3.6). The horizontal currents at 10 m were westward everywhere (Figure 3.6). The strongest currents were at the equator, with decreasing intensities north and south, showing the model's representation of the South Equatorial Current (SEC). There was much less divergence along the equator than in development run DN; however, there were clear divergence zones at about 2.5°N and 2.5°S . With the inclusion of Richardson number-dependent mixing, the core of the EUC deepened to 150 m, with a speed exceeding 35 cm/s in some locations, as shown in Figures 3.7 and 3.8. Figure 3.9 shows a shallowing of the main thermocline along the equator at day 720, similar to day 360 of development run DN. The main thermocline lies roughly along the EUC.

Figure 3.10 indicates upwelling beneath the single cold tongue along the equator, similar to the upwelling beneath the dual cold tongues in development run DN. Figure 3.11 shows the vertical velocity structure at 10 m. Upwelling occurs along the equator, along approximately 2.5°N and 2.5°S , and along approximately 5°N and 5°S . The zonal bands of upwelling are interleaved with weak downwelling. Downwelling also dominates along the poleward and western boundaries. The core of the zonally oriented upwelling and downwelling bands can also be seen in a cross section of vertical velocity (Figure 3.12).

3. Development Run DM

An intended next stage of test and development for the model was to include mixed layer entrainment while excluding Richardson number-dependent mixing in order to examine the relative roles of these individual processes. As for development run DR, development run DM was initialized from day 360 of run DN. Development run DM became numerically unstable and was discontinued after less than 24 hours of model time.

4. Development Run DRM

The next model development run included both Richardson number-dependent mixing and mixed layer dynamics. Again, this version of the model was initialized from day 360 of development run DN and was executed for an additional 360 days out to model day 720. By day 720 the model had achieved a steady state and, as in development run DR, a single cold tongue protruded westward along the equator from the eastern boundary at 10 m (Figure 3.13). The temperature contour patterns at 10 m were quite similar to those in development run DR (Figure 3.6). However, development run DRM was 0.5°C to 1.0°C degrees cooler across the domain. Additionally, the structure of the horizontal current field at day 720 for development run DRM (Figure 3.13) was similar to, though slightly weaker than, the horizontal current field for development run DR at the same time (Figure 3.6). In

development run DRM, the model's SEC has lost intensity compared to development run DR (cf. Figure 3.13 and 3.6). Figures 3.14 and 3.15 show the core of the EUC at approximately 200 m with a magnitude exceeding 25 cm/s at day 720 of development run DRM. With the inclusion of the mixed layer physics, the EUC core deepened approximately 50 m and the maximum core speed weakened approximately 10 cm/s. Figure 3.16 again shows that the main thermocline has an upward tilt from west to east and is located just above the EUC at day 720.

Similar to development run DR (Figure 3.10), upwelling beneath the equatorial cold tongue was evident at day 720 of development run DRM, as shown in Figure 3.17. Figure 3.18 portrays the vertical velocity structure of development run DRM at 10 m at day 720. With the addition of the mixed layer physics, there was more small scale structure evident than in run DR (Figure 3.11). Small areas of intermittent upwelling are adjacent to small areas of intermittent downwelling, possibly indicating some persistent numerical instability. This instability seems to have no significant effect upon the temperature and horizontal velocity fields, and it is evident only in the vertical velocity and mixed layer depth fields. These features will be discussed further in Chapter IV.

Of greater significance, the downwelling along the poleward boundaries weakened and was no longer evident at the western boundary. The zonal upwelling bands between 5°S and

5°N were not evident at 10 m at day 720. However, Figure 3.19 shows the zonal upwelling bands between 5°S and 5°N did exist between 20 m and 110 m. (Note that the evidence for downwelling and upwelling bands in meridional cross sections, such as Figure 3.19 are very dependent upon the location of the cross section.) Figure 3.20 depicts contours of mixed layer depth at day 720 for development run DRM. Deeper mixed layer depths are evident in the western domain decreasing towards the eastern boundary. The mixed layer depth contours roughly parallel the 10 m temperature contours. The inclusion of the mixed layer physics improved certain features of the model dynamics, such as the vertical redistribution of heat and momentum within the turbulent boundary layer. But the mixed layer physics also created some problematic features, such as the isolated shallow mixed layer cells seen in Figure 3.20. These features will be discussed further in Chapter IV.

5. Development Run DRM2

An additional development run, DRM2, was completed using both Richardson number-dependent mixing and mixed layer dynamics. This development run was initiated from a state of rest, as was the initial spin up model run, DN. The purpose of development run DRM2 was to remove any spurious nonlinear effects created by the transformation of the double cold tongue, evident at day 360 of development run DN, to a single cold tongue evident at day 720 of development run DRM. The

final stable states of run DRM and DRM2 were compared (i.e., day 360 of run DRM2 versus day 720 of run DRM) to identify any significant differences. At day 360 of DRM2, the 10 m temperature contours show colder water extended further westward than at day 720 of development run DRM (Figure 3.21 versus Figure 3.13). Development run DRM2 was approximately 0.5°C cooler overall and up to 1.0°C cooler in some locations along the equator. The qualitative temperature and current patterns were comparable to development run DRM results. Figures 3.22 and 3.23 show that the depth, speed, and zonal extent of the core of the EUC were also very similar - 200 m depth, greater than 25 cm/s velocity, and observable over all but the westernmost part of the basin (compared with Figures 3.14 and 3.15). Other similarities between development run DRM and DRM2 include a main thermocline that shallows from west to east just above the EUC and upwelling beneath the cold tongue (Figures 3.24 and 3.25).

Figure 3.26 shows the vertical velocity at 10 m for development run DRM2. Hints of arc shaped upwelling bands near 5°S and 5°N, evident at day 360 of development run DRM2, were more evident in development run DR than in development run DRM. The zonal upwelling bands that were apparent beneath 10 m in development run DRM (Figure 3.19) are not evident at day 360 of development run DRM2 (Figure 3.27). (Note though that cross section location may again be a factor.) Finally, Figure 3.28 shows contours of mixed layer depth for

development run DRM2. As in development run DRM (Figure 3.20), the contours roughly parallel the temperature contours and show problematic small scale features which will be discussed in Chapter IV. Over most of the domain, the mixed layer depths in run DRM2 were approximately 10 m shallower than in development run DRM.

6. Development Run DNL

In the next stage of development, the large domain was used (i.e., domain size was doubled in both the x and y directions). The model physics for development run DNL were identical to development run DN, but on the large domain, to diagnose the effects of the limited domain size and possible interactions between equatorial and boundary circulations in the less realistic smaller domain. Run DNL developed double cold tongues at 10 m, similar to those in run DN (compare Figures 3.29 and 3.1). The horizontal current structure (Figure 3.29) was also similar, with strong westward flow diverging from the equator. For the first time in the development phase, weak countercurrent flow existed at approximately 7°N and 7°S in the western portion of the basin. The eastward flow at 7°N and 7°S appear to be the model's representation of the North Equatorial Countercurrent (NECC) and South Equatorial Countercurrent (SECC). Propagating wave features were again evident along the poleward flanks of the cold tongues. These waves may be the the model's

representation of tropical instability waves (Legeckis et al., 1983). In the vicinity of the wave features, a stronger meridional temperature gradient was evident. Along the equator, westward currents were again constrained in the upper 20 m, with a slight decrease in depth from west to east (Figure 3.30). Figures 3.30 and 3.31 show a strong EUC core located at 20 m extending down to about 400 m in the west and 100 m in the east, which is significantly deeper than in development run DN (compare to Figures 3.2 and 3.3). Weaker westward flows surrounded this eastward current down to 200 m (Figure 3.31). From west to east, the main thermocline once again was located just above the EUC and shallowed to the east (Figure 3.32). In addition, a secondary thermocline was apparent above 20 m.

Figure 3.33 indicates upwelling beneath the double cold tongues and downwelling at the poleward boundaries. Figures 3.34 and 3.35 depict the structure of the vertical velocity field at day 360 for development run DNL. Upwelling occurred at the equator in patches. In addition, upwelling and downwelling occurred in bands oriented southwest to northeast north of the equator and northwest to southeast south of the equator, in association with the waves seen in Figure 3.29.

7. Development Run DRML

In the final development run, DRML, Richardson number-dependent mixing and mixed layer dynamics were implemented in

a large domain version of DRM2. At 10 m, the basic stabilized temperature and horizontal currents patterns (Figure 3.36) were similar to those in run DRM2 (Figure 3.21). Due to the increased size of the domain, the features that developed over the 360 day period of run DRML also became more intense. At the eastern boundary, 18.5°C water upwelled at the equator while in run DRM2 the upwelled water was 20°C. The maximum magnitude of the zonal velocity increased in the larger domain by approximately 15 cm/s to more than 40 cm/s, while the location of the maximum strength of the EUC remained approximately 12.5° from the eastern boundary (Figure 3.37). The core of the EUC was located at 200 m (Figure 3.37 and 3.38), compared to 150 m during development run DRM2. Again, the main thermocline was just above the EUC and shallowed from west to east (Figure 3.39). Figure 3.40 indicates upwelling beneath the equatorial cold tongue and downwelling on the poleward boundaries. In development run DRM2, downwelling at the poleward boundaries was not as apparent in the vertical temperature structure (Figure 3.25).

Figures 3.41 and 3.42 depict the vertical velocity structure. The vertical velocity has a much smaller horizontal scale than in development run DRM2. Upwelling is evident at the eastern boundary; downwelling is evident at the poleward and western boundaries. Figure 43 shows deeper mixed layer depths in the west that shallow toward the eastern boundary. Again, the mixed layer depth contours roughly

parallel the 10 m temperature contours as was seen in development run DRM2.

8. Development Runs Summary

During the developmental phase, various combinations of model physics and domain sizes were used to produce the best simulation of the equatorial ocean. Richardson number dependent mixing was crucial in producing a realistic depiction of an equatorial cold tongue and equatorial upwelling. Mixed layer physics produced cooler upper ocean temperatures than without mixed layer physics due to increased mixing within the turbulent boundary layer. A larger domain size in run DNL produced the first indications of off-equatorial countercurrents akin to the SECC and NECC. Additionally, a larger domain size produced features with greater intensity: e.g., an EUC maximum velocity of more than 40 cm/s in run DRML, more representative of the real ocean.

B. MODEL EXPERIMENTS

At the end of the developmental process, an initial state and model formulation were chosen to conduct model experiments on wind forcing. Day 360 of developmental run DRM2 was used to initialize the first experimental model run. Although development run DR appeared to have smoother temperature and horizontal velocity fields than did development runs DRM or DRM2, it lacked the complete set of mixed layer dynamics that were of primary interest for this study. The much greater run

times required for the large domain model mandated that the majority of the experimental model runs be done on the small domain. The experimental run are summarized in Table 3-2.

Four model experiments were conducted using the small domain. The goal of the experiments was to determine the model's upper ocean response to different wind stresses. The wind stress used to force the model became progressively more complex and realistic with each successive experiment. For the first experiment, denoted E1, the zonal wind stress was specified analytically as a function of y as shown in Figure 3.44. In the second experiment, E2, the zonal wind stress was specified analytically to vary with both x and y as shown in Figure 3.45. In the third experiment, E3, the zonal wind stress remained the same and a meridional wind stress, specified analytically to vary with both x and y , was added. Figure 3.46 portrays the wind stress field used in Experiment E3. For the final experiment, E4, a time varying wind stress, based on operational atmospheric boundary layer wind analyses, was used to force the model.

1. Experiment 1 (E1)

The first complexity added to the wind stress was a meridional variation (Figure 3.44). (See the Appendix for the actual wind stress formulation.) This new wind stress was ramped in linearly over a period of two weeks to minimize the

Table 3-2. EXPERIMENT RUNS SUMMARY

Experiment	Wind Stress	Initial State	Period (in days)
E1	$\tau = \tau_x(y)$	DRM2 Day 360	360 - 720
E2	$\tau = \tau_x(x, y)$	DRM2 Day 360	360 - 720
E3	$\tau = \tau_x(x, y) + \tau_y(x, y)$	E2 Day 720	720 - 1080
E4	$\tau = \tau_x'(x, y, t) + \tau_x(x, y)$ $+ \tau_y'(x, y, t) + \tau_y(x, y)$	E3 Day 1080	1080 - 1170

shock to the model. The model was then run out to day 720, by which time the model had adjusted to the new wind stress and stabilized.

At day 720, the temperature and current structure of the model was significantly different from the initial temperature field (Figure 3.47). At 10 m, a cold tongue extended westward from the eastern boundary. However, the temperature throughout the domain increased from 0.5°C to 2.5°C, compared to the initial temperature field (Figure 3.21). In addition, warm water extended from the west along 5°N and 5°S towards the eastern boundary. At the equator, the flow was westward over most of the domain but strongly eastward near the western boundary. Countercurrents, the model's version of the SECC and NECC, formed in the vicinity of 5°S and 5°N (Figure 3.47) and transported water from the west to the east, corresponding to the warm water extensions.

Along the poleward boundaries, the flow was progressively more westward towards the western boundary.

The depth of the EUC also changed significantly during run E1. At the end of development run DRM2, the core of the EUC was positioned at 200 meters (Figure 3.22). At day 720 of E1, the core of the EUC is located at 50 m (Figure 3.48). Thus, the EUC core shallowed 150 m during run E1. The speed of the EUC also changed. At the end of development run DRM2, the maximum speed of the EUC was in excess of 25 cm/s (Figure 3.22). At day 720 of E1, the maximum speed of the EUC decreased to less than 20 cm/s (Figures 3.48 and 3.49). Figure 3.49 shows the model's countercurrents along 5°S and 5°N extending to a depth of 80 m, and the westward flow at the poleward boundaries extending to 150 m. The westward flow at the poleward boundaries is 10 to 15 cm/s stronger than at the end of the development run DRM2 (Figure 3.23).

In addition to the horizontal temperature and current changes, the zonal temperature profile also changed, though in more subtle ways (compare Figure 3.50 and 3.24). Figure 3.50 shows that the main thermocline shallows from west to east, as seen previously, but the main thermocline is now about 50 m higher and below the EUC core. The vertical temperature structure from north to south (Figure 3.51) indicates upwelling along the equator beneath the cold tongue and downwelling along the poleward boundaries.

Figures 3.52 and 3.53 depict the vertical velocity structure. Upwelling dominates along the equator and eastern boundary while downwelling dominates along the poleward boundaries and most of the western boundary. The structure of the mixed layer depth (Figure 3.54) has also changed considerably. The mixed layer depth contours no longer resemble the 10 m temperature contours, as was seen in developmental runs DRM and DRM2. The mixed layer depth structure showed a strong qualitative similarity to the wind stress field. Shallow mixed layer depths predominate in the equatorial region, where the wind stress is weakest, becoming deeper toward the poleward boundaries, where the wind stress is strongest.

2. Experiment 2 (E2)

At the next level of complexity, the zonal wind stress was specified to vary in both x and y . The wind stress decreased both from east to west and toward the equator (Figure 3.45). (See the Appendix for the actual wind stress formulation.) Again, the new wind stress was ramped in linearly over a period of two weeks, and the model was run out to day 720, by which time the model had stabilized.

At day 720, the 10 m temperature and current structure (Figure 3.55) showed similarities to, as well as differences from, the results of run E1 (Figure 3.47). The overall temperature pattern was quite similar -- cold water extended

westward along the equator and along the poleward boundaries with intervening warm water. The major differences were in the intensity of the features (compare Figures 3.47 and 3.55). The cold tongue along the equator did not extend as far westward; the 23.5°C contour extended only half way across the domain rather than almost 5/6ths of the way across the domain. Similarly, the cold water along the poleward boundaries did not extend as far westward. Additionally, warmer water of about 24°C dominated the western portion of the domain at day 720 of run E2.

The horizontal current structure at 10 m (Figure 3.55) also showed similarities to and differences from run E1. At day 720 of run E2, there was westward flow at the poleward boundaries and westward flow along the equator, except for a small area of strong eastward flow at the western boundary. However, the model's countercurrents along 5°S and 5°N were not as well developed as in run E1. Some counter flow did exist, but there was a much larger meridional component than existed in Experiment 1. Figure 3.56 shows that the core of the EUC shallowed to a depth of approximately 40 m and weakened approximately 5 cm/s, to less than 15 cm/s (cf. Figure 3.48 for run E1). In addition, Figure 3.57 also shows that the countercurrents along 5°S and 5°S are much weaker than in run E1 (Figure 3.49).

Figure 3.58 depicts the E2 zonal temperature profile. The zonal slope of the main thermocline was much smaller than

in E1 and all the development runs (Figures 3.50, 3.9, 3.16, 3.24, 3.32 and 3.39). However, Figure 3.59 shows weak upwelling beneath the equatorial cold tongue and downwelling at the poleward boundaries which is qualitatively similar to what was seen in run E1. The vertical velocity shown in Figures 3.60 and 3.61 also depicts weaker upwelling along the equator and the eastern boundary and downwelling along the poleward boundaries. The mixed layer depth structure at day 720 (Figure 3.62) again had a pattern qualitatively similar to the wind stress field. The mixed layer depth decreased from the poleward boundaries towards the equator and also decreased from east to west, as did the wind stress.

3. Experiment 3 (E3)

For Experiment 3, yet another level of complexity was added to the wind stress. A non-zero meridional wind stress component was introduced for the first time, yielding a total wind stress vector that converged toward the equator. The meridional component was also constructed to decrease in intensity both from east to west and approaching the equator. The wind stress field for Experiment 3 (Figure 3.46) was designed to approximate the annual mean wind stress for the western and central Pacific (Trenberth et al., 1989). (See the Appendix for the actual wind stress formulation.) The initial state for run E3 was day 720 of run E2. For run E3, the new wind stress was ramped in linearly over a period of

six weeks. The model was run for a total of 360 days with the new wind stress out to model day 1,080 by which time it had stabilized.

At day 1,080, the temperature and current patterns (Figure 3.63) were very similar to those in the initial conditions for this experiment. At 10 m, cold water extended westward along the equator and along the poleward boundaries with warm water protrusions centered at about 5°N and 5°S . Westward flow dominated along the equator, except at the western boundary where the flow reversed (Figure 3.63). Westward flow also dominated along the poleward boundaries. Weak countercurrents, the model's representation of the NECC and SECC, at about 4°N and 4°S were evident only in the western portion of the domain. Figure 3.64 shows that the core of the EUC has returned to 50 m, maintained its intensity, and decreased its zonal extent compared to run E2 (Figure 3.56). Figure 3.65 shows the westward flow along the poleward boundaries has decreased in intensity as well as maximum depth compared to run E2 (Figure 3.57). Maximum westward velocity at the poleward boundaries decreased to less than 15 cm/s and retreated to 110 m. This was a decrease of 5 cm/s and 40 m from the initial state (Figure 3.57).

In contrast to the initial state (Figure 3.58), Figure 3.66 shows that the main thermocline has shallowed from east to west as in run E1 (Figure 3.50). Figure 3.67 suggests upwelling beneath the equatorial cold tongue and downwelling

along the poleward boundaries, similar to the initial state (Figure 3.51). In the vicinity of 5°S and 5°N, weak depressions of the isotherms may be attributable to downwelling. The vertical velocity structure (Figures 3.68 and 3.69) again showed upwelling along the equator and eastern boundary and downwelling along the poleward boundaries. At day 1080 of run E3, the mixed layer depth structure (Figure 3.70) again showed a strong qualitative similarity to the wind stress field. The mixed layer depth decreased from the poleward boundaries towards the equator and also decreased from east to west, as did the wind stress. Thus, deeper mixed layer depths were associated with greater wind stress magnitudes.

4. Experiment 4 (E4)

For the final experiment, E4, a time-varying wind stress was used to force the model. The Navy Operational Atmospheric Global Prediction System (NOGAPS) marine layer winds for the period 1 December 1991 to 29 February 1992 were used to calculate a time-varying wind stress perturbation. An area in the western and central Pacific, extending from 160°E to 170°W and from 10°S to 10°N, was chosen for the model domain. There were several westerly wind events that occurred in this region during this December - February period. The strongest event occurred during early January and was

associated with the Axel and Betsy cross-equatorial typhoon pair.

The time-averaged wind field for the 91 day December - February period was calculated and then subtracted from the actual wind field for each of the 91 days to obtain a time-varying wind field perturbation. A wind stress perturbation was then calculated from each wind field perturbation. Finally, the time-varying wind stress perturbation was added to the analytic wind stress field used in run E3. This composite time-varying wind stress field was then used to force the model for the 91-day run, E4. The model handled the time-varying wind stress with no apparent problems.

Figures 3.71 through 3.74 show the wind stress fields used to force the model from day 1114 to day 1123, every 3 days. These model days correspond to 03, 06, 09 and 12 January 1992. At the beginning of the 10-day period, a westerly event is centered approximately at the equator and 167°E (Figure 3.71). By model day 1117 (06 January) this westerly event has dissipated (Figure 3.72). Figure 3.73 depicts the wind stress associated with Typhoon Axel at approximately 5°N and 175°E. Finally, Figure 3.74 shows the wind stress field after Typhoon Axel had moved west of the model domain's western boundary and a surge in the northeast tradewinds and equatorial easterly winds occurred.

Figures 3.75 through 3.78 show the temperature and horizontal current patterns corresponding to the wind stress patterns discussed above. At model day 1114 (03 Jan) a reversal in the SEC was apparent in the western basin (Figure 3.75). This corresponded well with the westerly wind stress event that propagated from west to east during the first few days of January and was depicted in Figure 3.71. Figure 3.76 shows the reversal in SEC diminished as the westerly wind stress event weakened (Figure 3.72). Figure 3.77 shows the horizontal currents approximately paralleled the wind stress associated with Typhoon Axel (Figure 3.73). Eastward flow extended along the equator, from the westward boundary to approximately 177°E , with the strongest westward flow located south-southwest of Axel's position, between 5°N and the equator (Figure 3.77). Figure 3.78 shows a diminished reversal of the SEC in the western basin as Typhoon Axel tracked west beyond the western boundary. Figure 3.78 also shows a protrusion of cold water extended approximately along 5°N in the wake of Typhoon Axel. Note that throughout the 10-day period (03 - 12 January), eastward currents dominated along the equator in the western basin, and the 24°C isotherm is pushed eastward from approximately 166°E to approximately 169°E (cf. Figures 3.75 and 3.78).

Figures 3.79 through 3.82 show the vertical velocity patterns corresponding to the wind stress, temperature and horizontal current fields discussed above. Figure 3.79 shows

an area of upwelling dominated the basin just north of the equator at model day 1114 (03 January). By model day 1117 (06 January), the upwelling area intensified and the maximum was located approximately at 1°N and 174°E (Figure 3.80). This upwelling area seems to correspond with the westerly wind event that propagated through the western basin during the first few days of January, although, the upwelling appeared to lag the wind stress by approximately two to three days. Figure 3.81 shows the upwelling area along the equator had diminished in zonal extent by model day 1120 (09 January). However, indications of upwelling and downwelling associated with Typhoon Axel were apparent. Finally, Figure 3.82 shows the downwelling along the equator had diminished further by model day 1123 (12 January), but a downwelling area was located in the same area as the cold water protrusion (Figure 3.78). At model day 1123 (12 January), equatorial upwelling extended from the eastern boundary to approximately the dateline (Figure 3.82) associated with the resurgence of the strong easterly wind stress (Figure 3.73). Additional downwelling and upwelling regions were evident in the wake of Typhoon Axel.

Animations of daily model output for the period of the January westerly wind events (not shown) reveal a clear oscillation between easterly and westerly wind regimes between 5°S and 5°N . The animations also show a strong correspondence between the reversal in the SEC and the downwelling areas.

Animation of the total current vector in an x-z cross section along the equator show indications of excitation of a Kelvin wave associated with the equatorial downwelling.

5. Experiments Summary

Throughout the experimental phase, progressively more complex and realistic wind stress fields were used to force the model. The more realistic wind stress used in the experimental phase produced more complex temperature and horizontal current patterns characteristic of the real ocean. Additionally, the model's vertical velocity patterns became more realistic as a result of the more realistic wind stress. The more realistic wind stresses produced a better overall model ocean. For example, better countercurrents, a less noisy vertical velocity field, better off-equatorial downwelling and less extreme upwelling at the equator were produced by the more realistic wind stresses. When a time-varying wind stress containing several westerly wind events was used to drive the model, complex fluctuations in the model's temperatures and currents were produced. Reversals in the SEC were apparent, and indications of equatorially trapped Kelvin waves were evident.

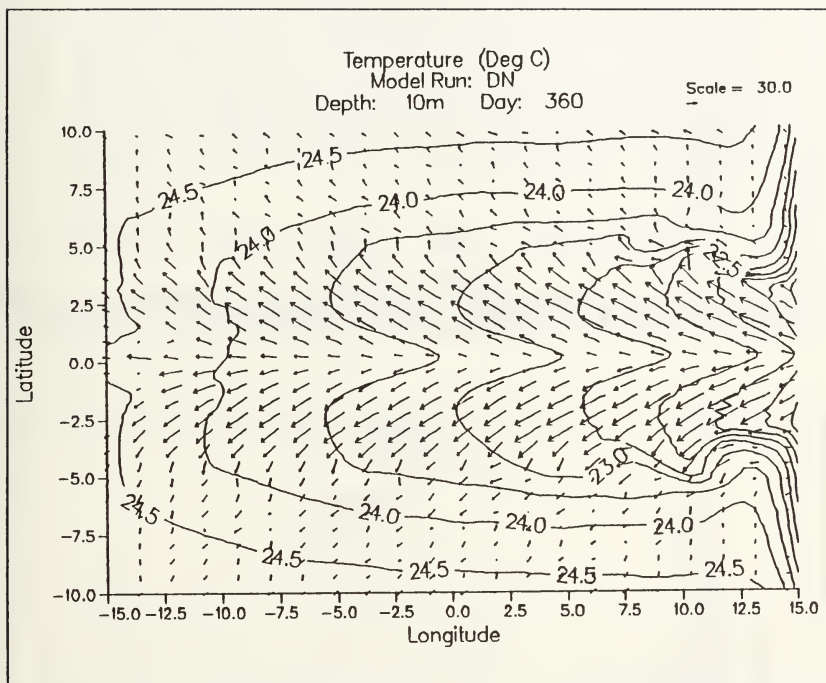


Figure 3.1. Development run DN 10 m temperature and horizontal currents (cm/s). Contour interval is 0.5°C.

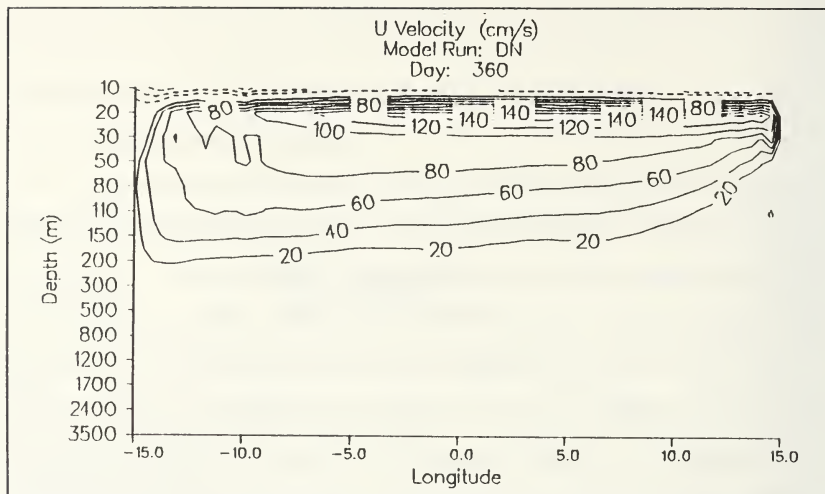


Figure 3.2. Development run DN zonal velocity y-z cross section along the equator. Contour interval is 20 cm/s.

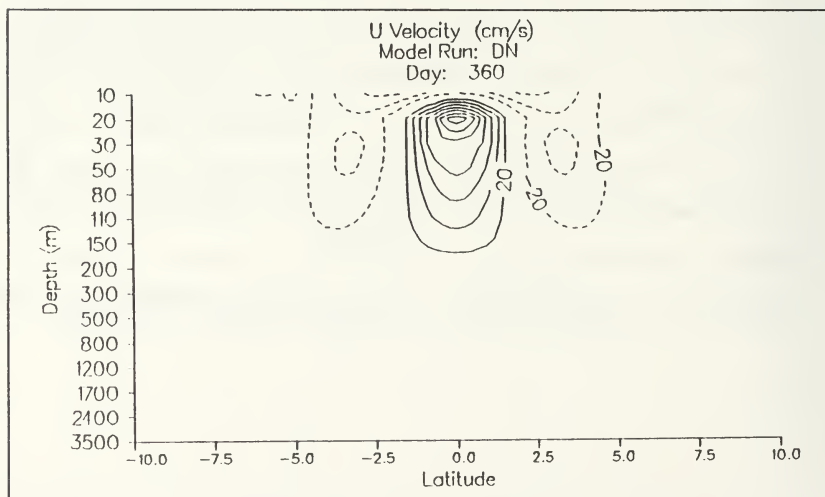


Figure 3.3. Development run DN zonal velocity y-z cross section through mid-basin. Contour interval is 20 cm/s.

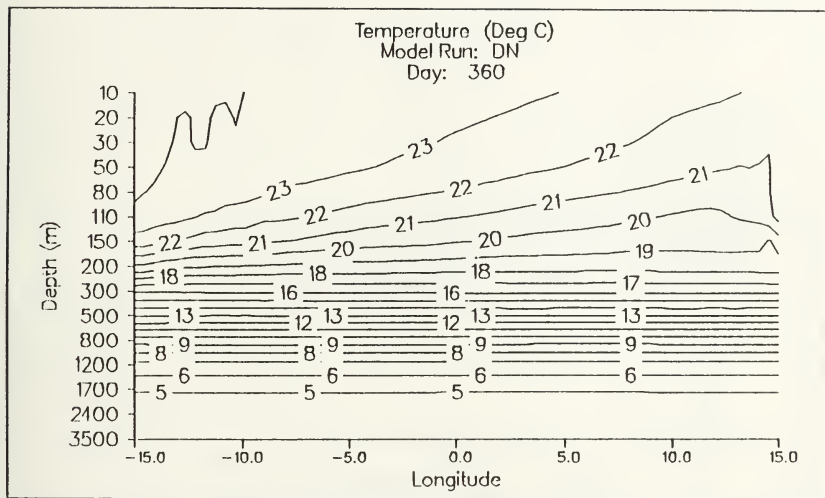


Figure 3.4. Development run DN temperature y-z cross section along the equator. Contour interval is 1.0°C .

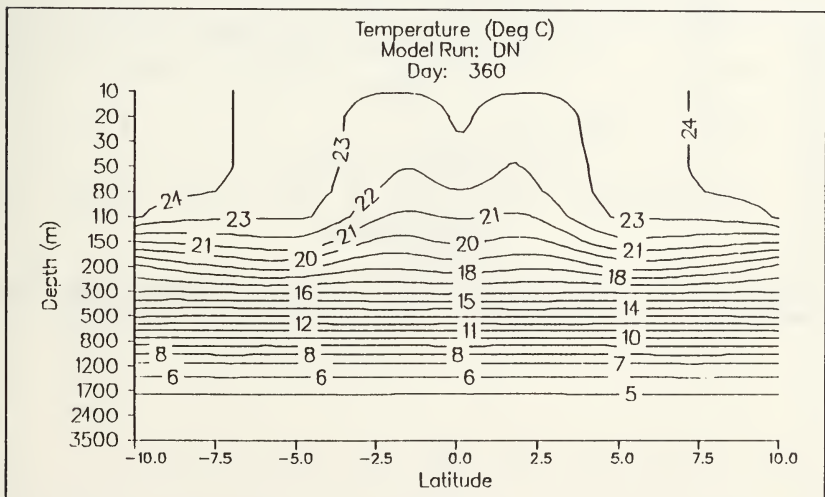


Figure 3.5. Development run DN temperature y-z cross section through mid-basin. Contour interval is 1.0°C .

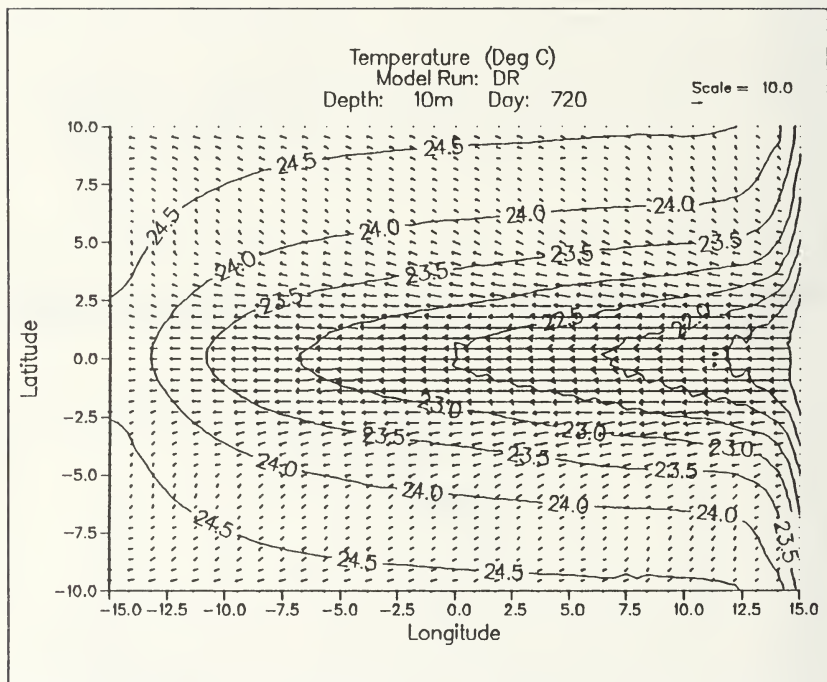


Figure 3.6. Development run DR 10 m temperature and horizontal currents (cm/s). Contour interval is 0.5°C.

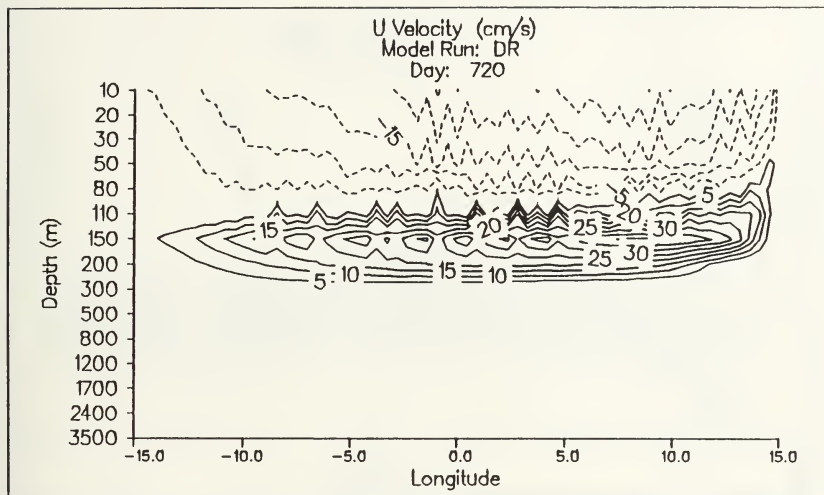


Figure 3.7. Development run DR zonal velocity x-z cross section along the equator. Contour interval is 5 cm/s.

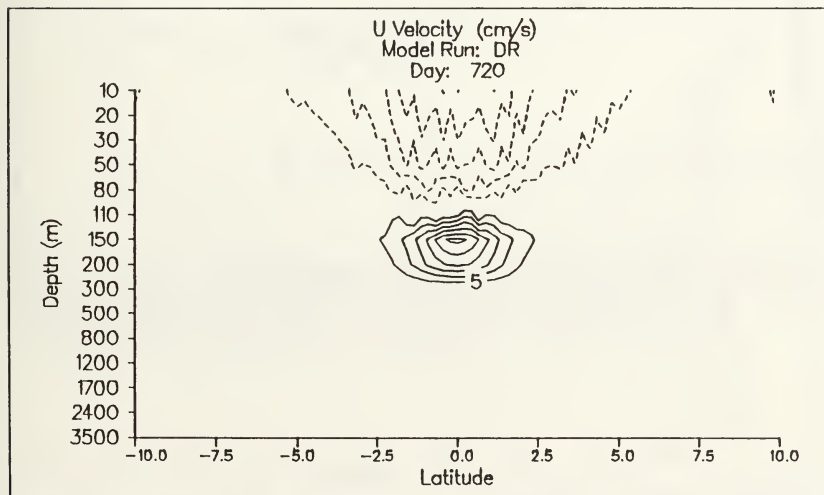


Figure 3.8. Development run DR zonal velocity y-z cross section through mid-basin. Contour interval is 5 cm/s.

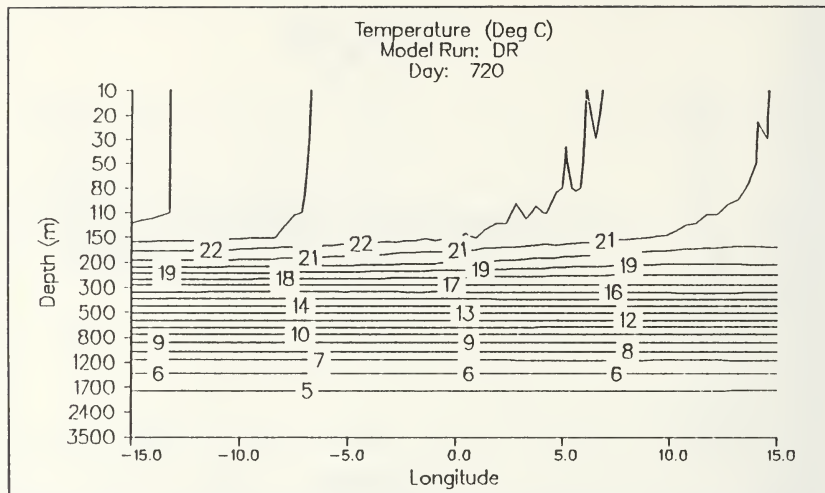


Figure 3.9. Development run DR temperature y-z cross section along the equator. Contour interval is 1.0°C.

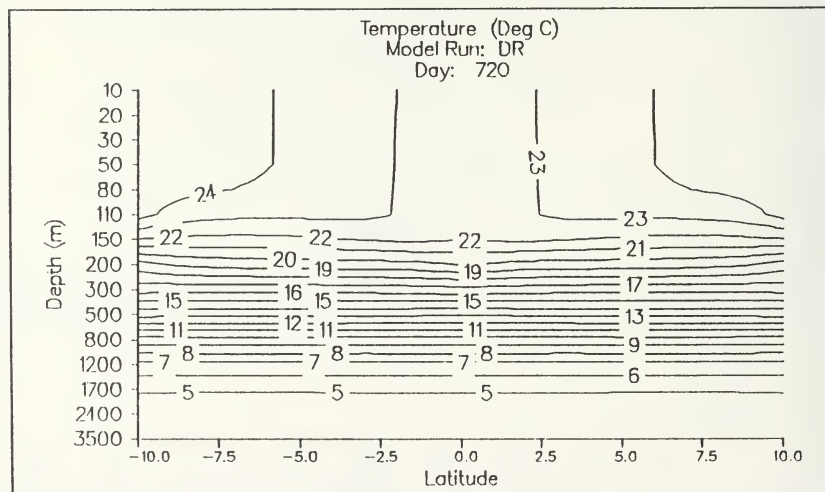


Figure 3.10. Development run DR temperature y-z cross section through mid-basin. Contour interval is 1.0°C.

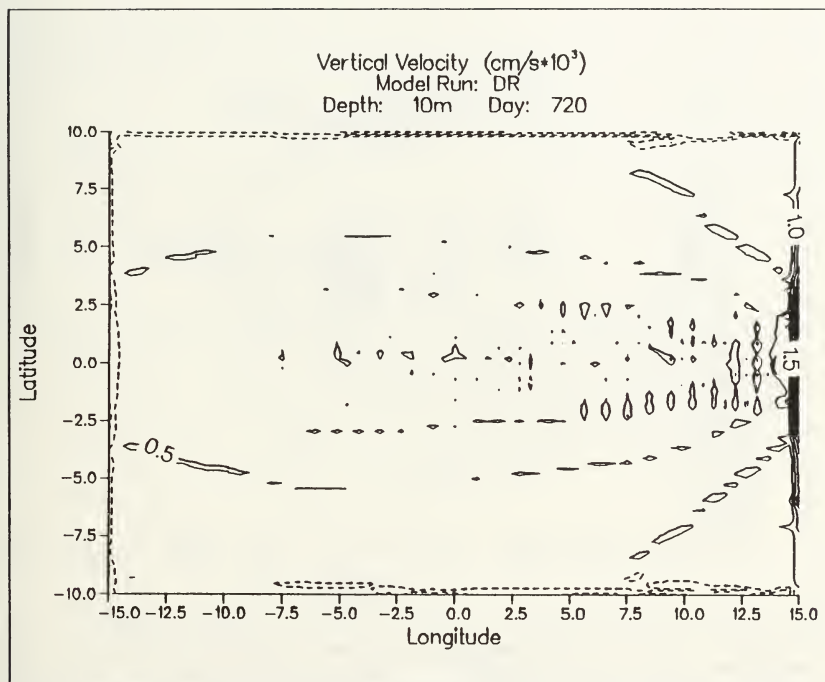


Figure 3.11. Development run DR 10 m vertical velocity. Contour interval is $0.5 \times 10^3 \text{ cm/s}$. Solid lines depict positive values; dashed lines depict negative values.

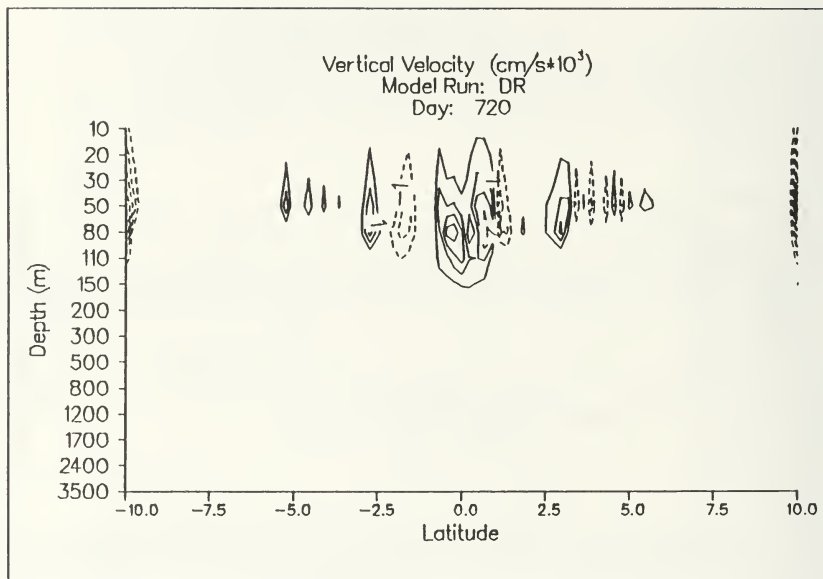


Figure 3.12. Development run DR vertical velocity y-z cross section through mid-basin. Contour interval is 1.0×10^3 cm/s. Solid lines depict positive values; dashed lines depict negative values.

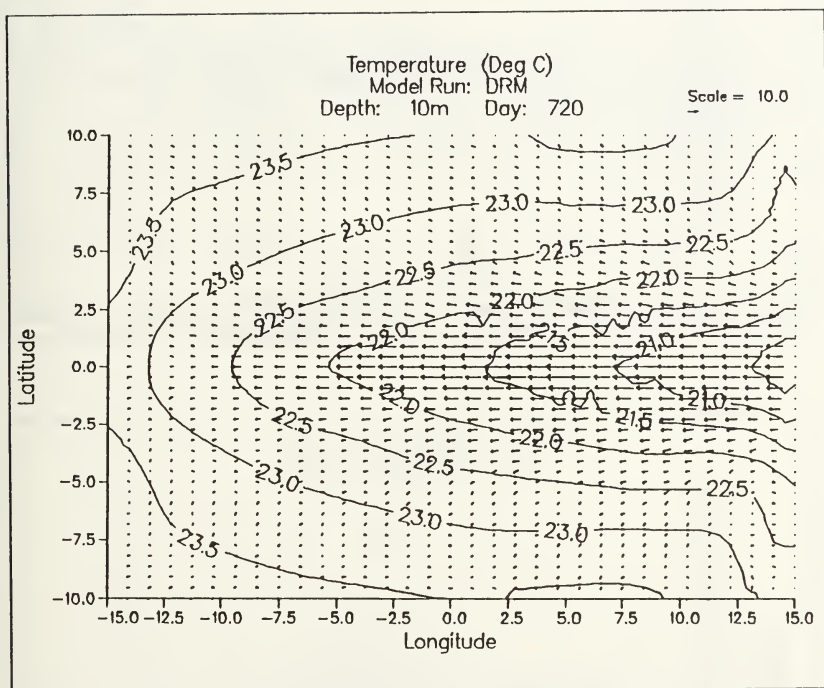


Figure 3.13. Development run DRM 10 m temperature and horizontal currents (cm/s). Contour interval is 0.5°C.

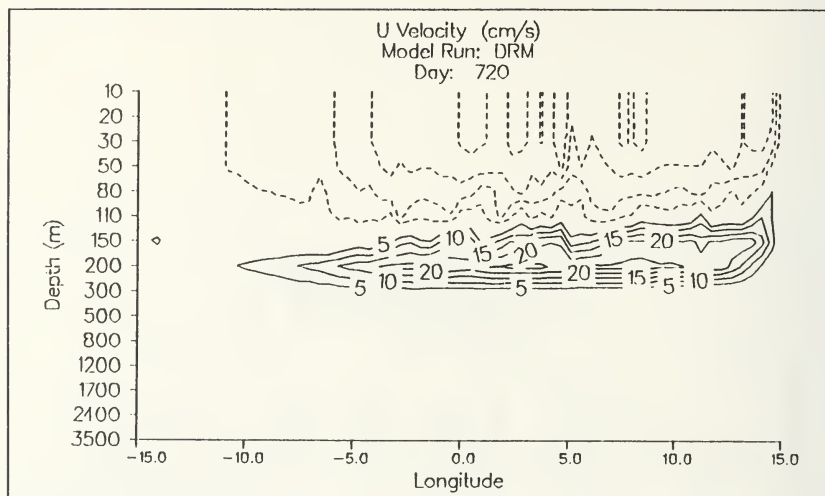


Figure 3.14. Development run DRM zonal velocity y-z cross section along the equator. Contour interval is 5 cm/s.

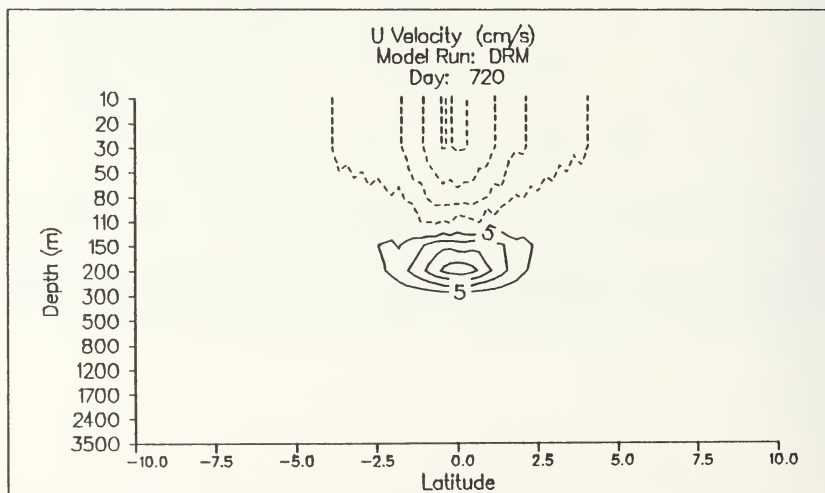


Figure 3.15. Development run DRM zonal velocity x-z cross section through mid-basin. Contour interval is 5 cm/s.

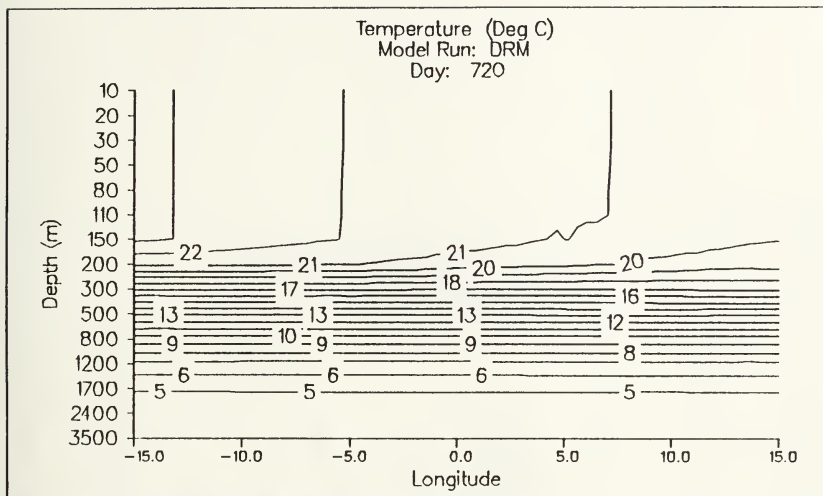


Figure 3.16. Development run DRM temperature x-z cross section along the equator. Contour interval is 1.0°C .

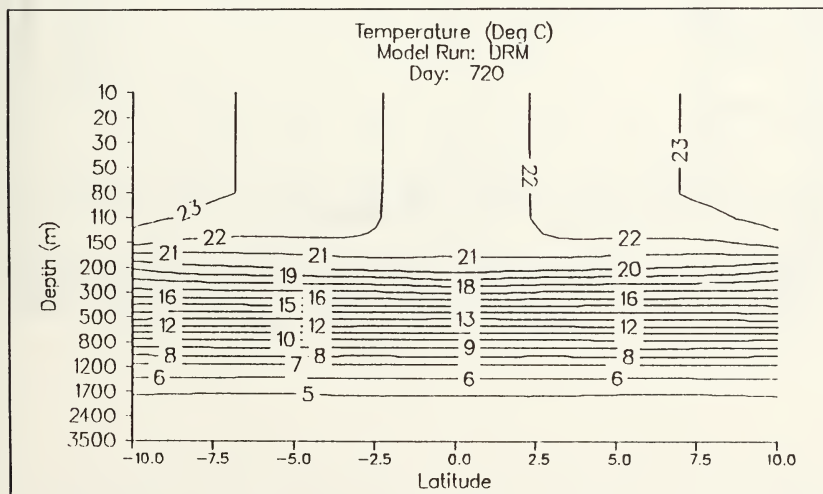


Figure 3.17. Development run DRM temperature y-z cross section through mid-basin. Contour interval is 1.0°C .

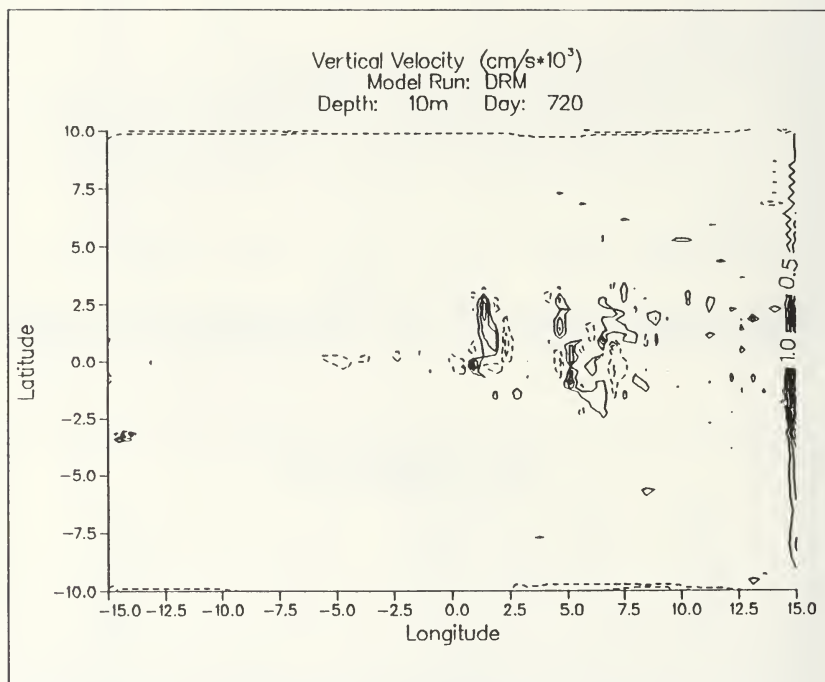


Figure 3.18. Development run DRM 10 m vertical velocity. Contour interval is 0.5×10^3 cm/s. Solid lines depict positive values; dashed lines depict negative values.

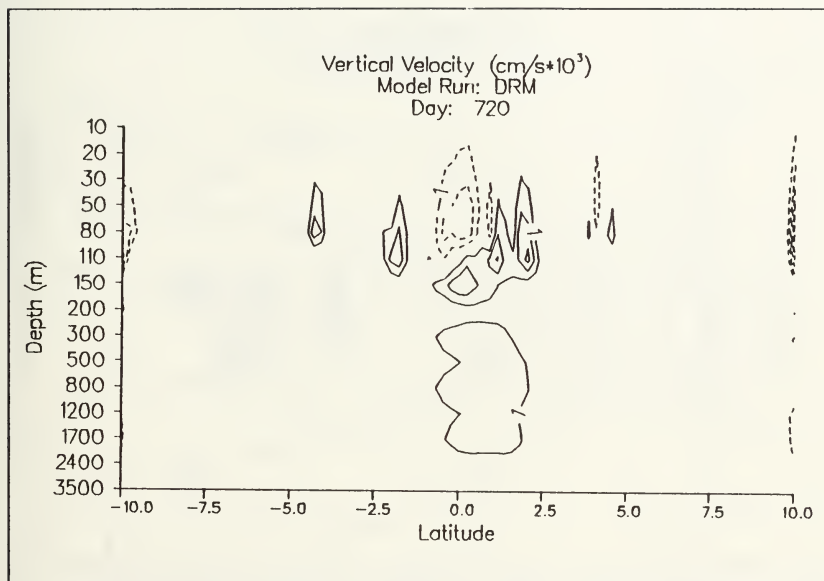


Figure 3.19. Development run DRM vertical velocity y-z cross section through mid-basin. Contour interval is 1.0×10^3 cm/s. Solid lines depict positive values; dashed lines depict negative values.

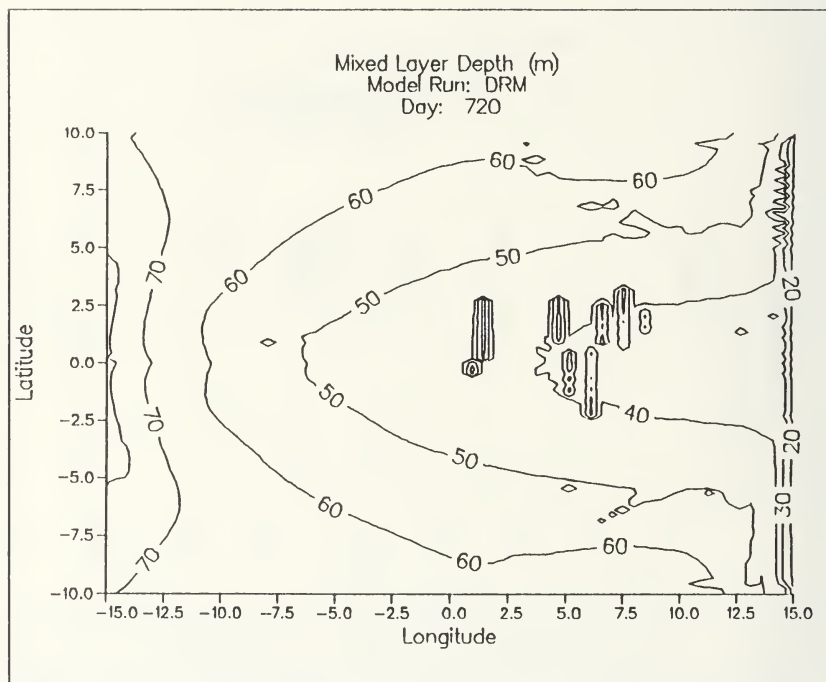


Figure 3.20. Development run DRM mixed layer depth. Contour interval is 10 m.

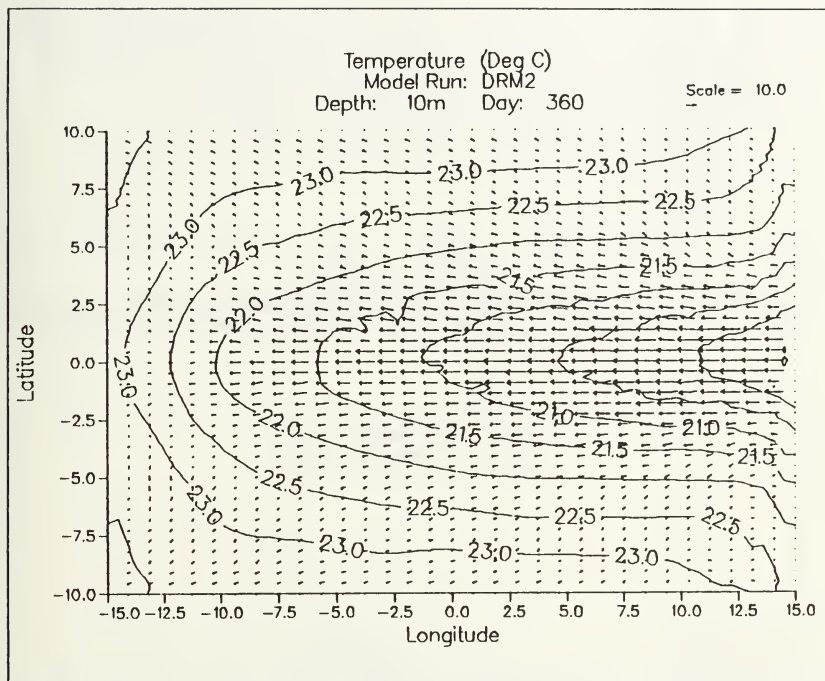


Figure 3.21. Development run DRM2 10 m temperature and horizontal currents (cm/s). Contour interval is 0.5°C.

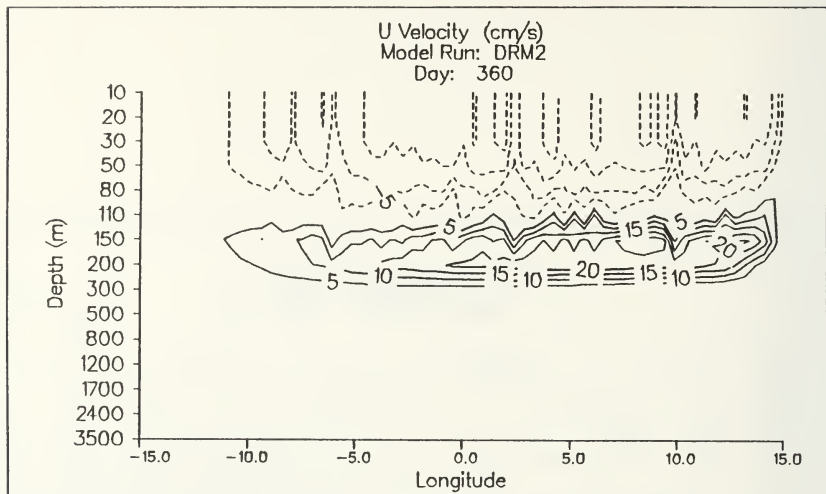


Figure 3.22. Development run DRM2 zonal velocity x-z cross section along the equator. Contour interval is 5 cm/s.

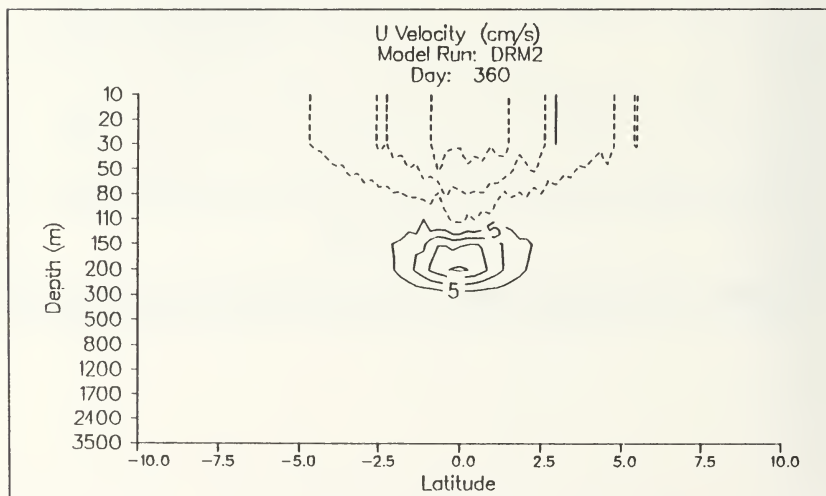


Figure 3.23. Development run DRM2 zonal velocity y-z cross section through mid-basin. Contour interval is 5 cm/s.

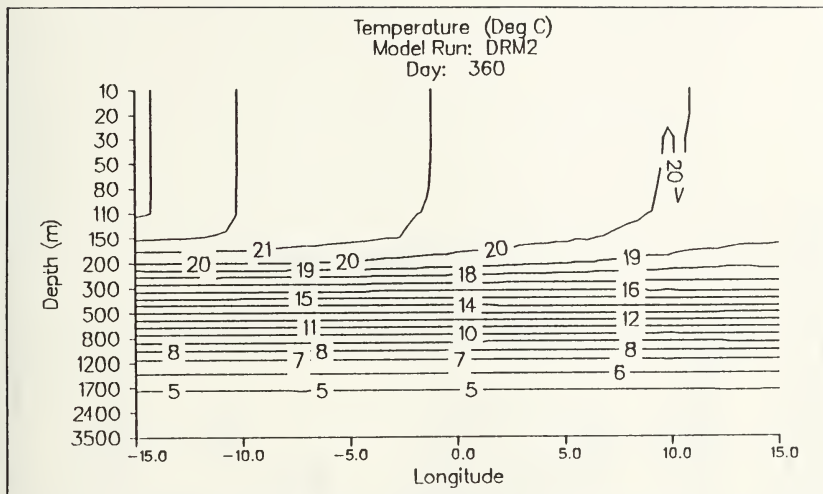


Figure 3.24. Development run DRM2 temperature x-z cross section along the equator. Contour interval is 1.0°C.

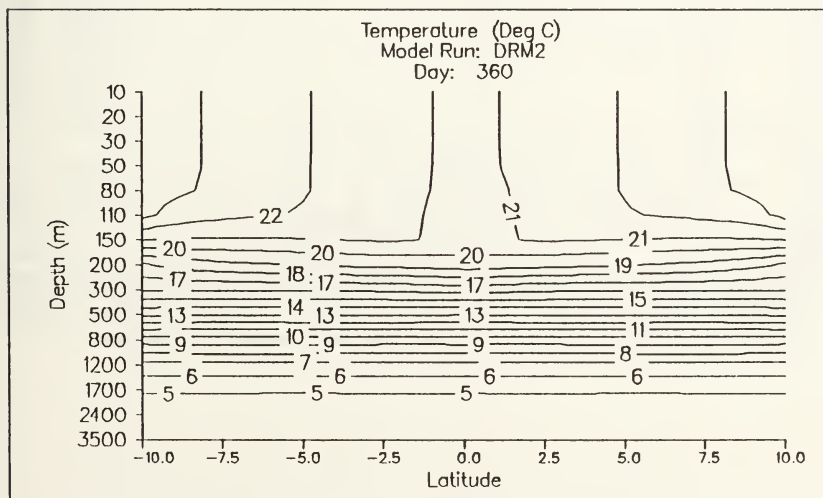


Figure 3.25. Development run DRM2 temperature x-z cross section through mid-basin. Contour interval is 1.0°C.

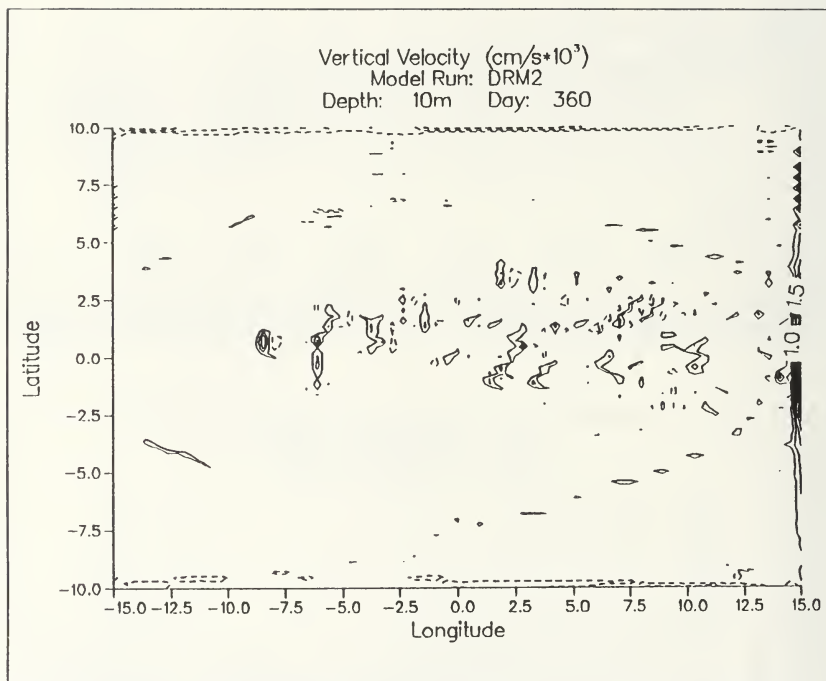


Figure 3.26. Development run DRM2 10 m vertical velocity. Contour interval is 0.5×10^3 cm/s. Solid lines depict positive values; dashed lines depict negative values.

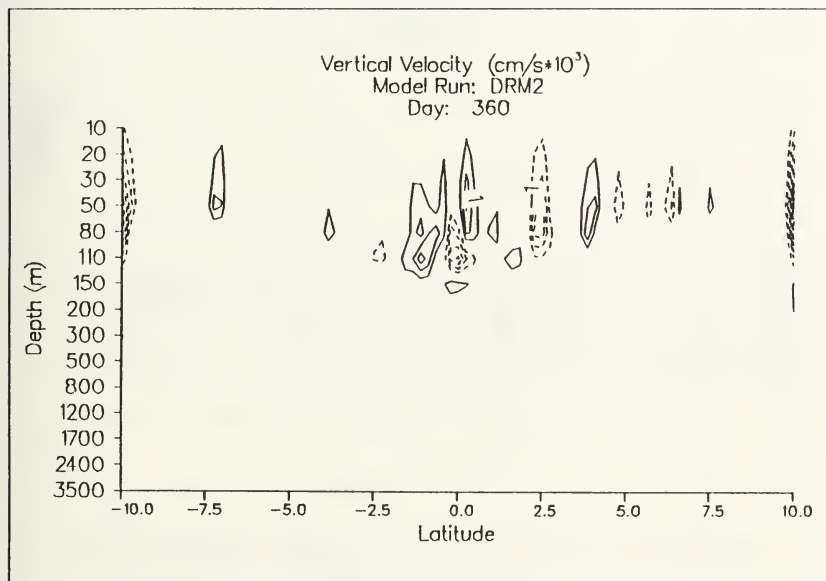


Figure 3.27. Development run DRM2 vertical velocity y-z cross section. Contour interval is 1.0×10^3 cm/s. Solid lines depict positive values; dashed lines depict negative values.

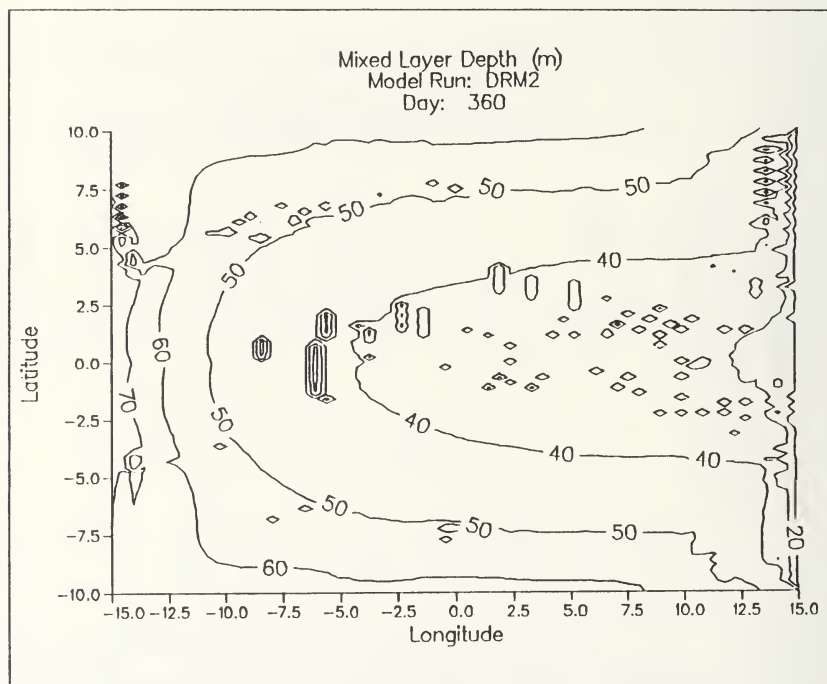


Figure 3.28. Development run DRM2 mixed layer depth. Contour interval is 10 m.

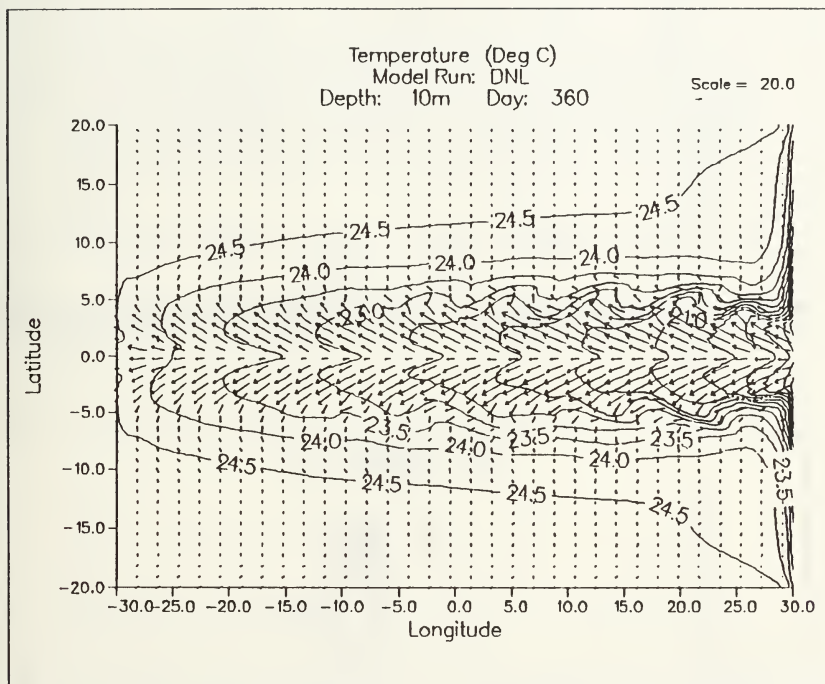


Figure 3.29. Development run DNL 10 m temperature and horizontal currents (cm/s). Contour interval is 0.5°C.

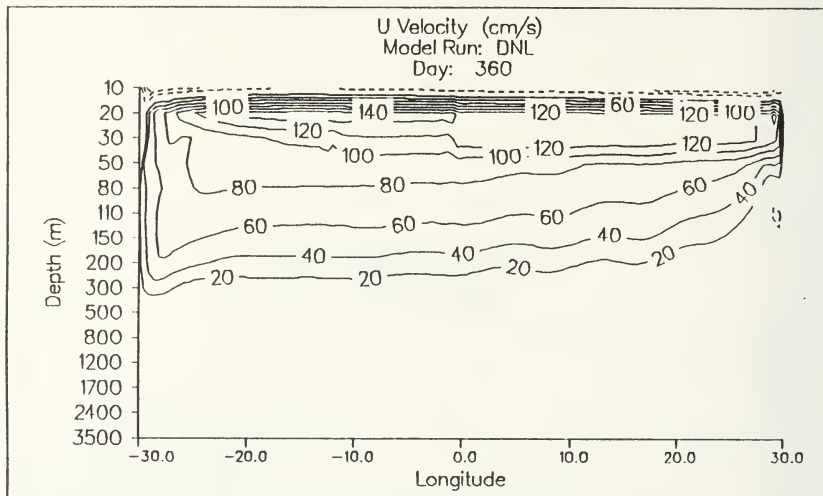


Figure 3.30. Development run DNL zonal velocity x-z cross section along the equator. Contour interval is 20 cm/s.

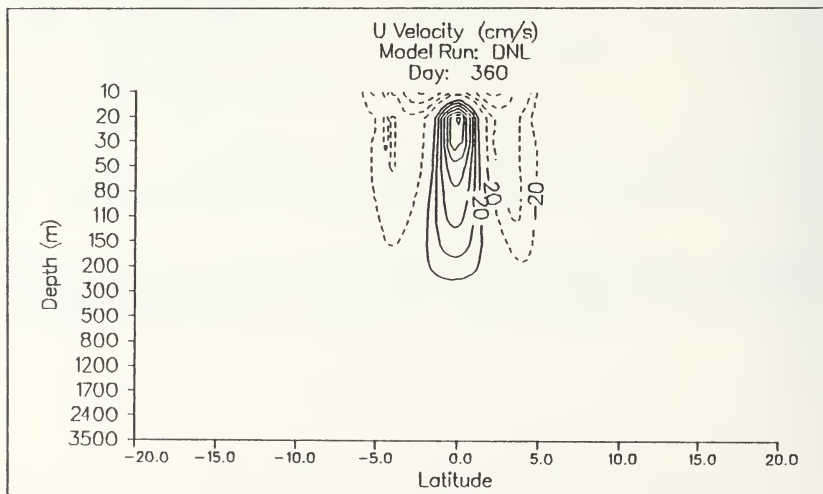


Figure 3.31. Development run DNL zonal velocity y-z cross section through mid-basin. Contour interval is 20 cm/s.

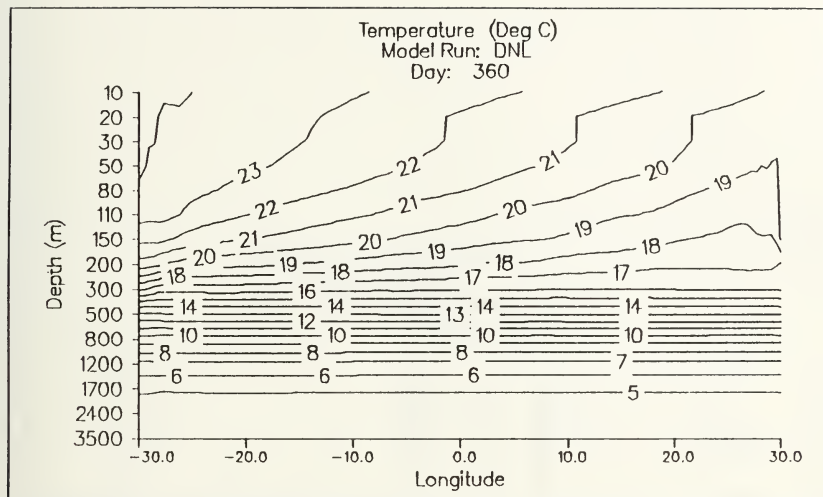


Figure 3.32. Development run DNL temperature x-z cross section along the equator. Contour interval is 1.0°C.

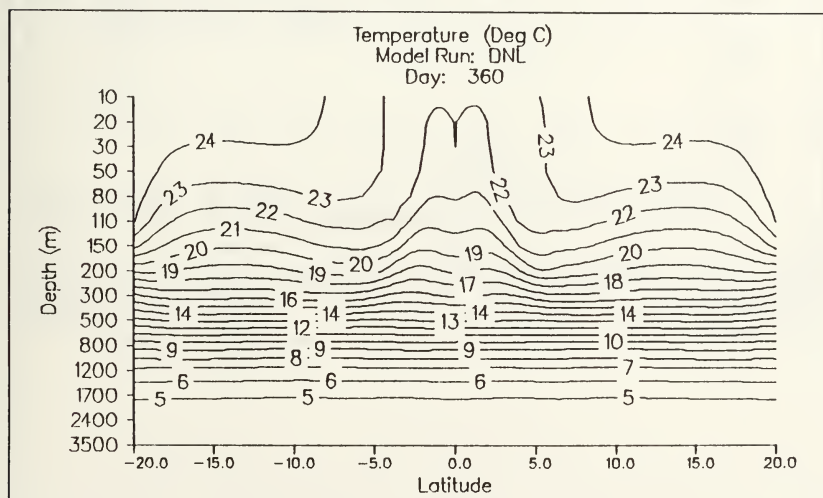


Figure 3.33. Development run DNL temperature y-z cross section through the mid-basin. Contour interval is 1.0°C.

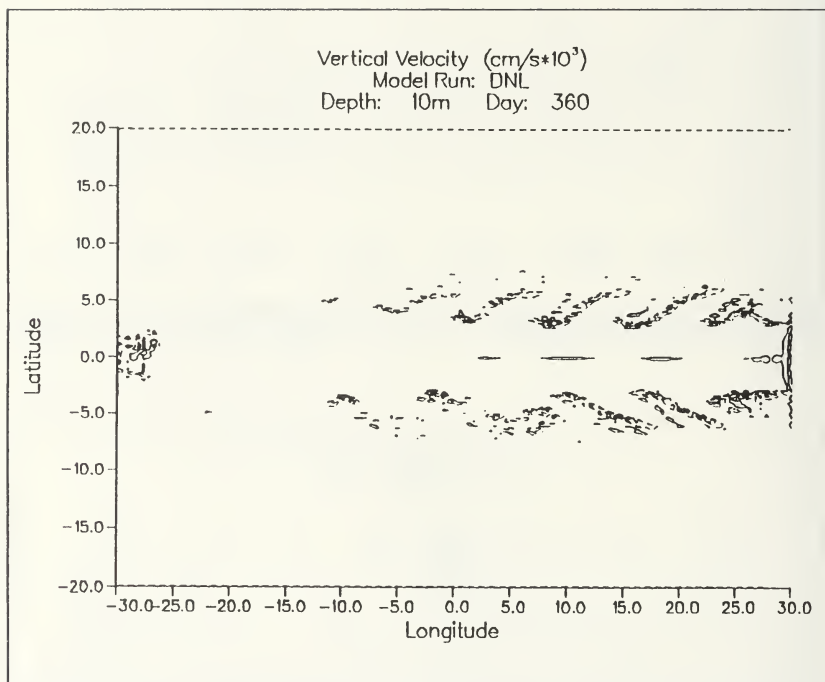


Figure 3.34. Development run DNL 10 m vertical velocity. Contour interval is $0.5 \times 10^3 \text{ cm/s}$. Solid lines depict positive values; dashed lines depict negative values.

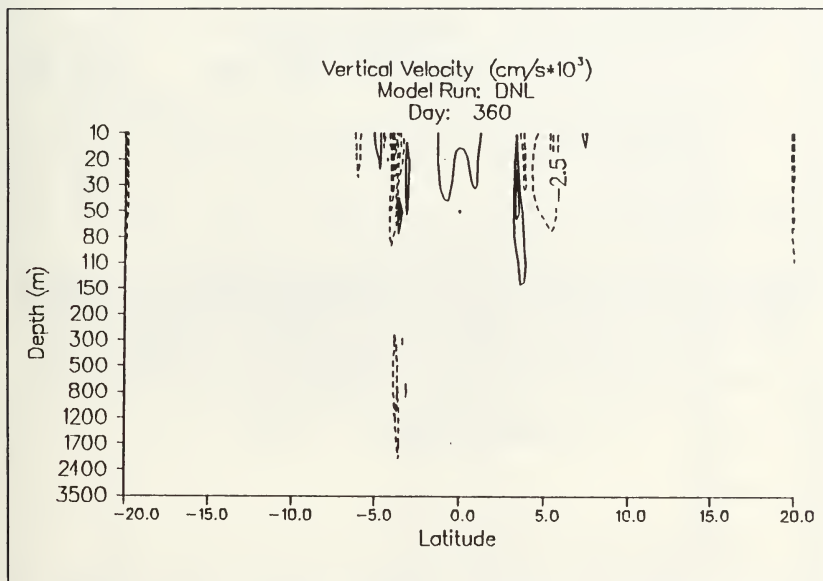


Figure 3.35. Development run DNL vertical velocity y-z cross section through mid-basin. Contour interval is 2.5×10^3 cm/s. Solid lines depict positive values; dashed lines depict negative values.

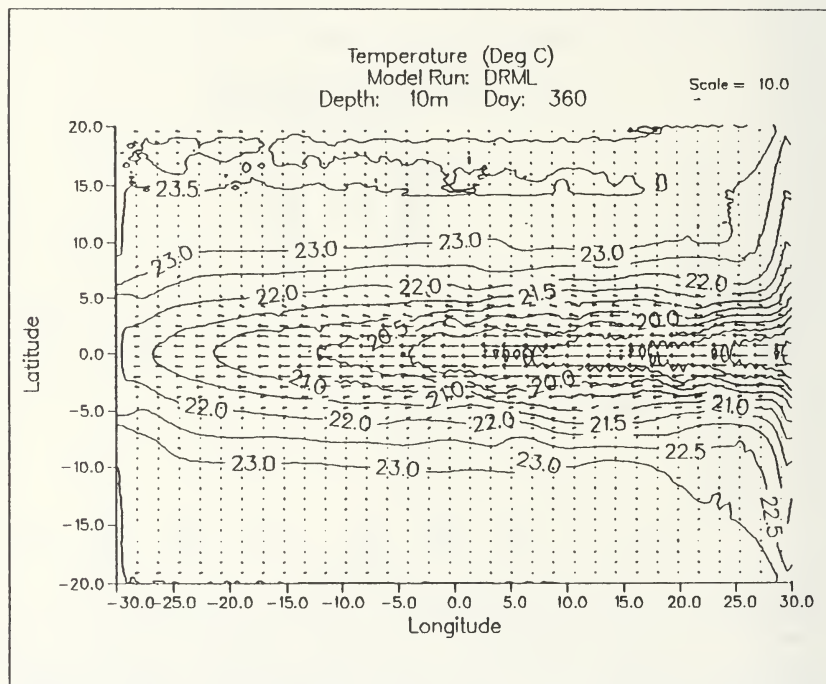


Figure 3.36. Development run DRML 10 m temperature and horizontal currents (cm/s). Contour interval 0.5°C.

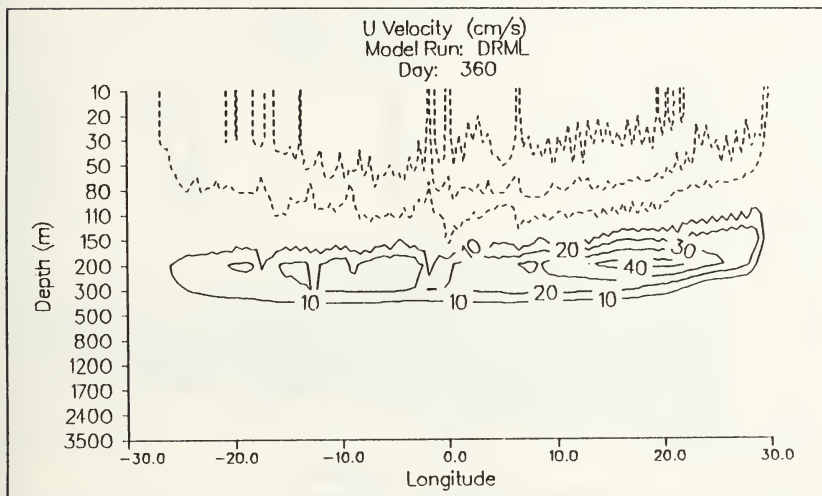


Figure 3.37. Development run DRML zonal velocity x-z cross section along the equator. Contour interval is 10 cm/s.

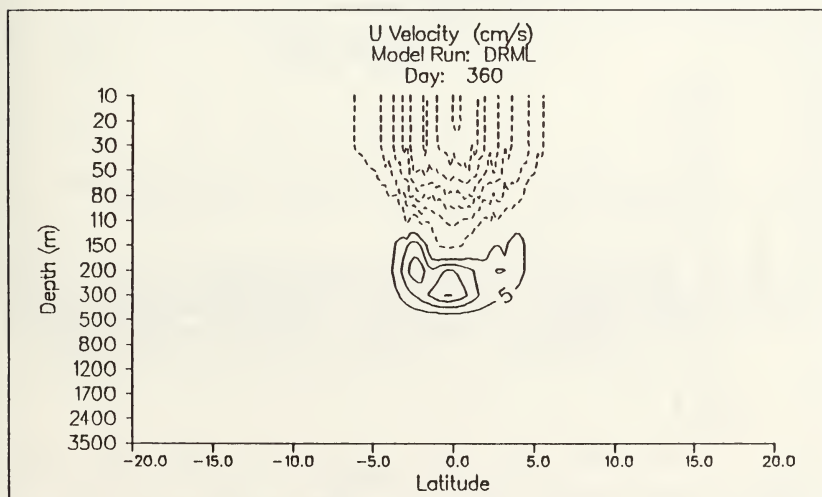


Figure 3.38. Development run DRML zonal velocity y-z cross section through mid-basin. Contour interval is 5 cm/s.

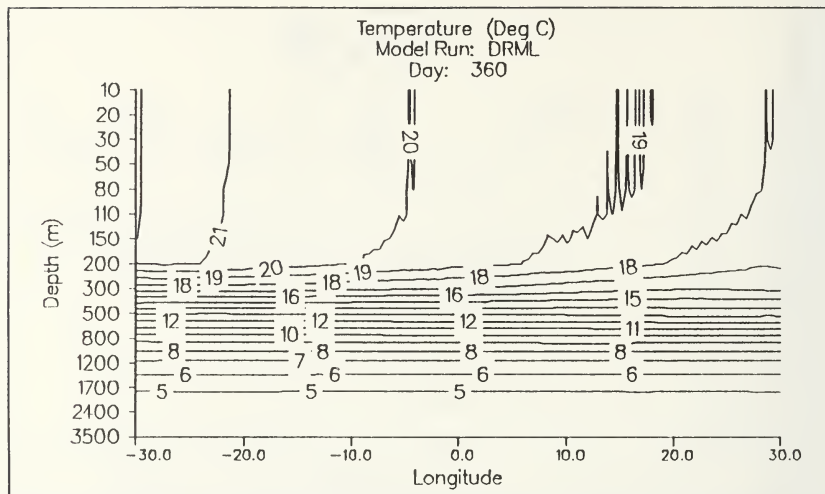


Figure 3.39. Development run DRML temperature x-z cross section along the equator. Contour interval is 1.0°C .

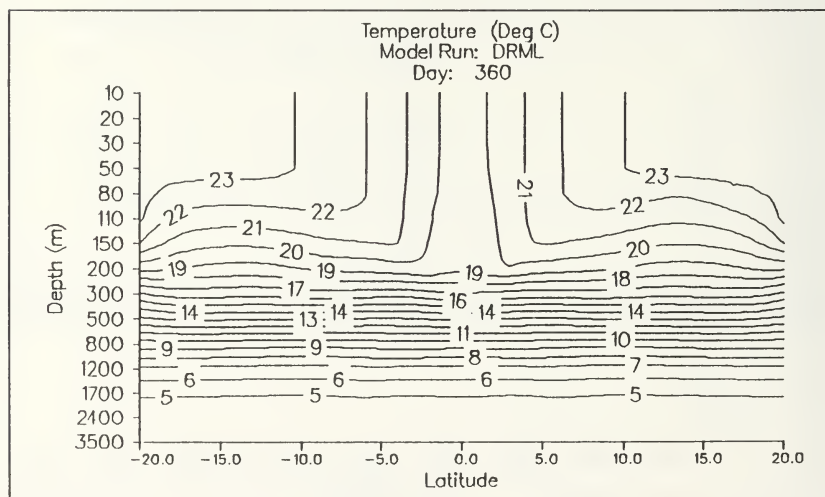


Figure 3.40. Development run DRML temperature y-z cross section through mid-basin. Contour interval is 1.0°C .

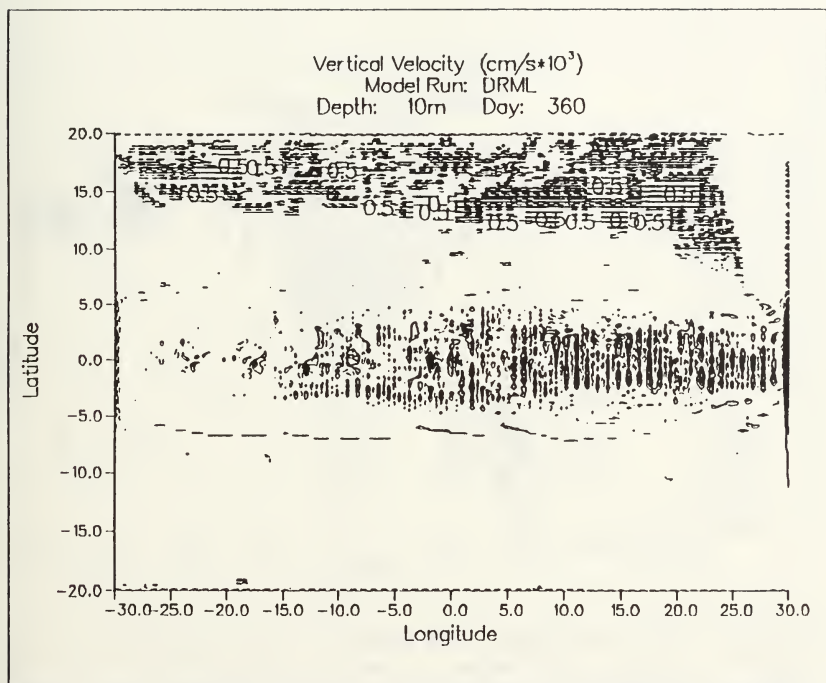


Figure 3.41. Development run DRML 10 m vertical velocity. Contour interval is $0.5 \times 10^3 \text{ cm/s}$. Solid lines depict positive values; dashed lines depict negative values.

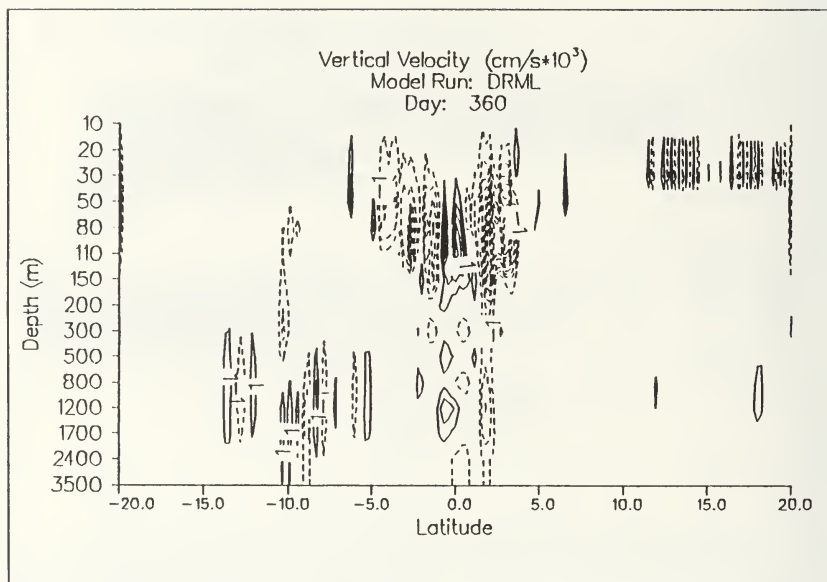


Figure 3.42. Development run DRML vertical velocity y-z cross section through mid-basin. Contour interval is 1.0×10^3 cm/s. Solid lines depict positive values; dashed lines depict negative values.

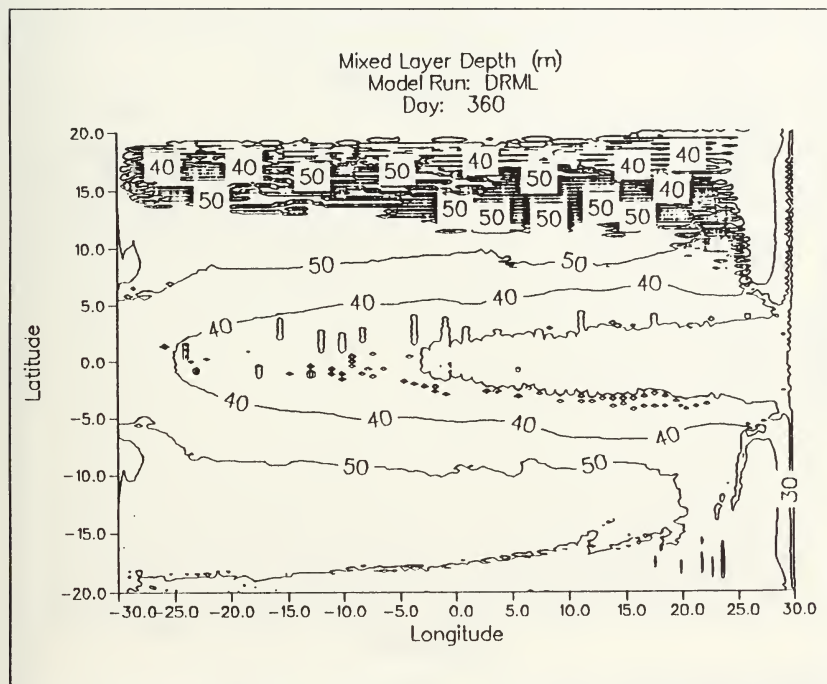


Figure 3.43. Development run DRML mixed layer depth. Contour interval is 10 m.

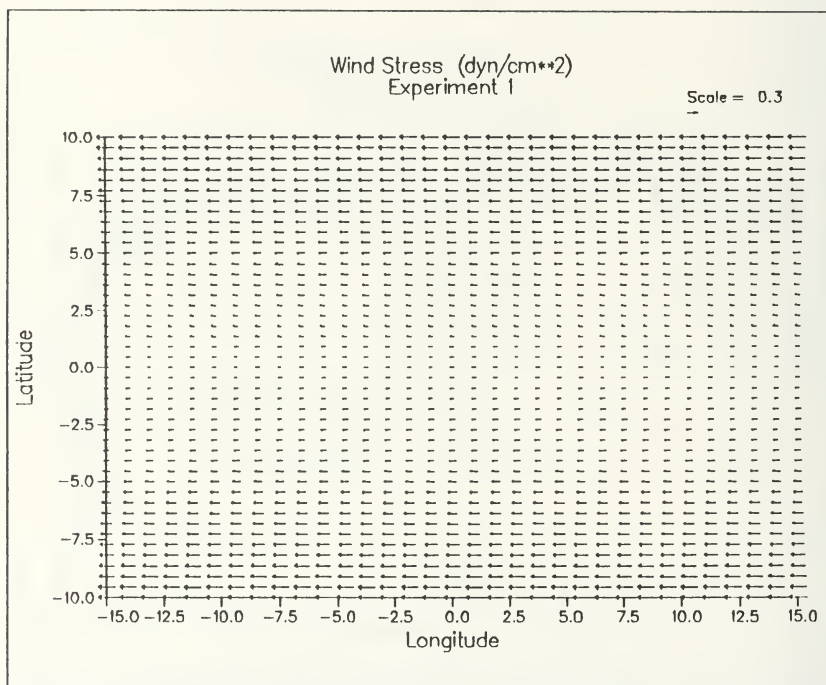


Figure 3.44. Experiment 1 wind stress: zonal component varies meridionally; no meridional component.

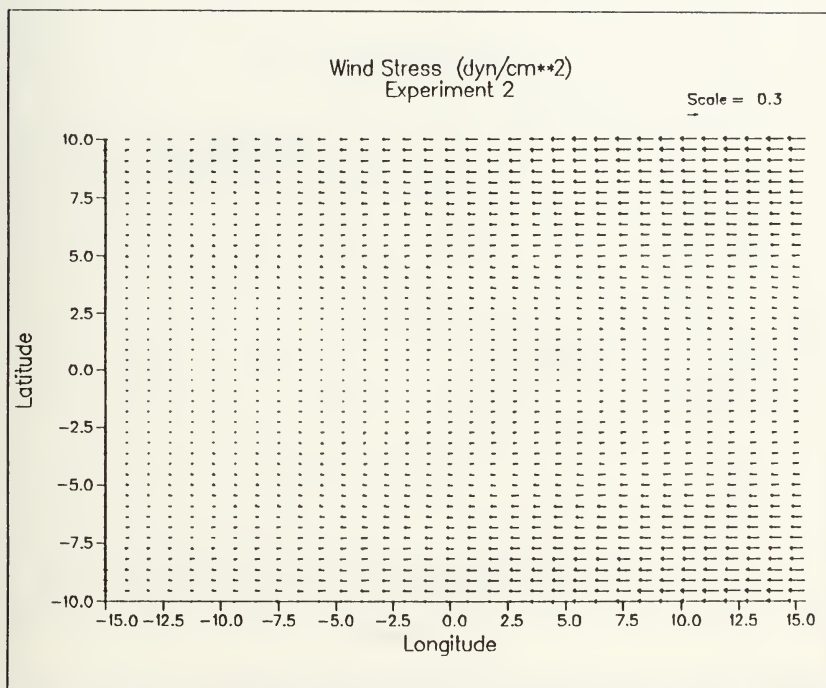


Figure 3.45. Experiment 2 wind stress: zonal component varies zonally and meridionally; no meridional component.

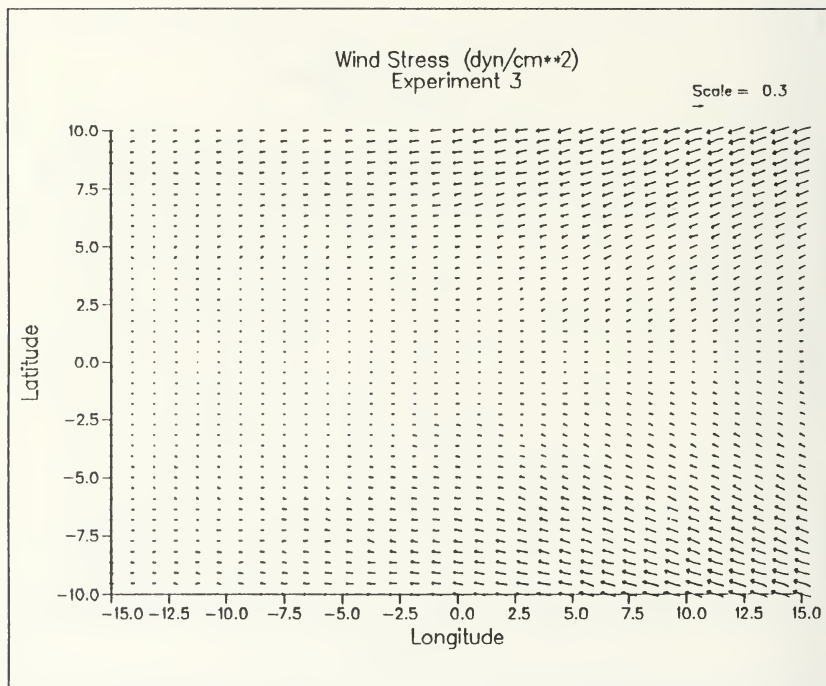


Figure 3.46. Experiment 3 wind stress: zonal and meridional components vary zonally and meridionally.

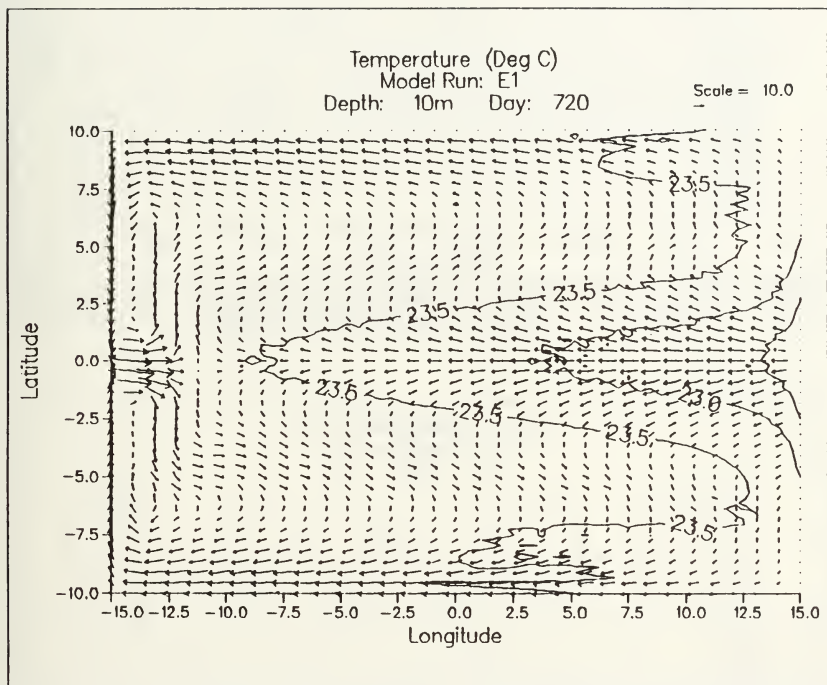


Figure 3.47. Experiment 1 10 m temperature and horizontal currents (cm/s). Contour interval is 0.5°C.

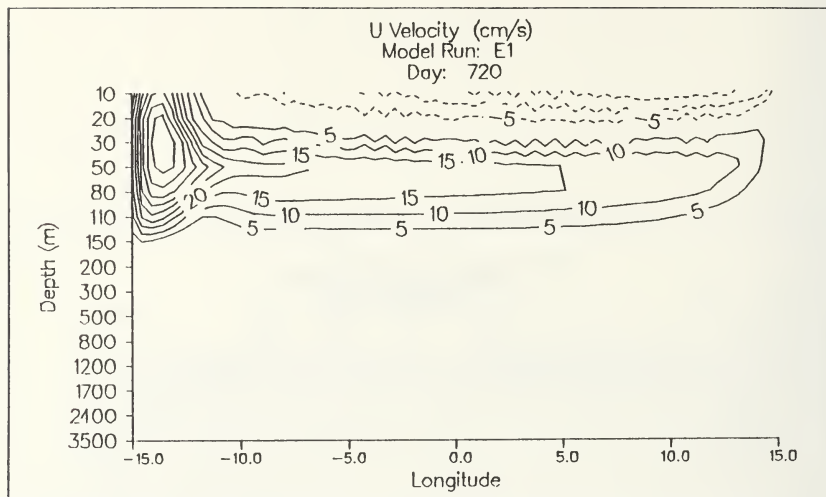


Figure 3.48. Experiment 1 zonal velocity x-z cross section along the equator. Contour interval is 5 cm/s.

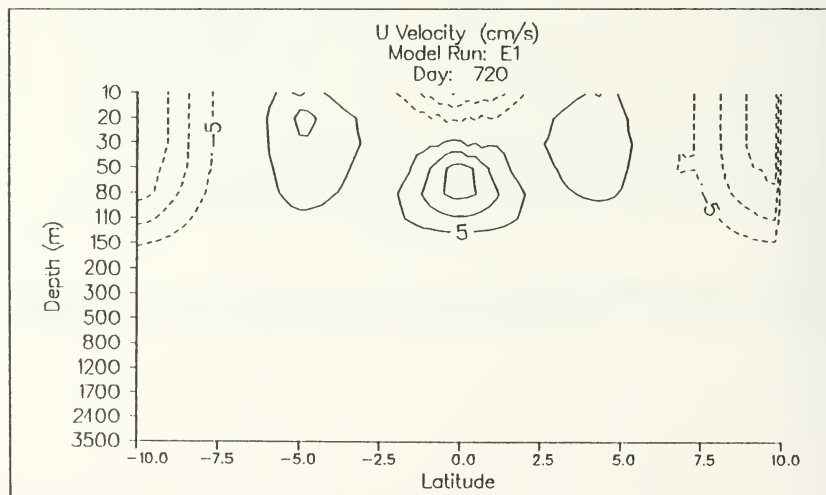


Figure 3.49. Experiment 1 zonal velocity y-z cross section through mid-basin. Contour interval is 5 cm/s.

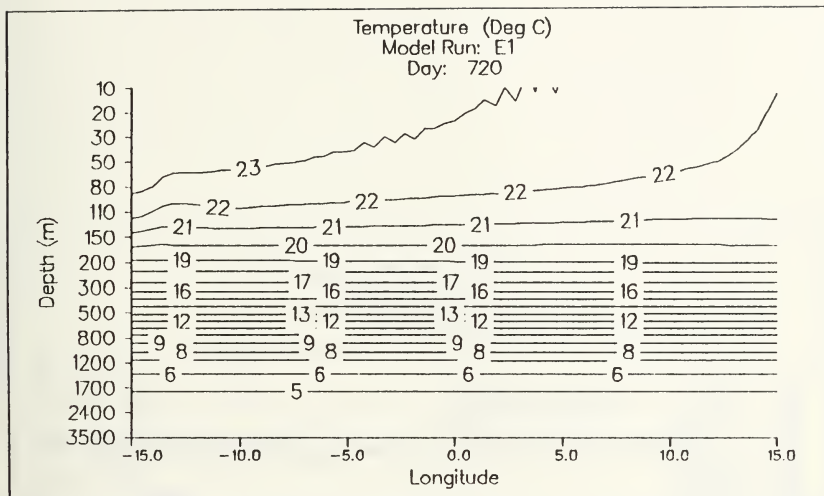


Figure 3.50. Experiment 1 temperature x-z cross section along the equator. Contour interval is 1.0°C.

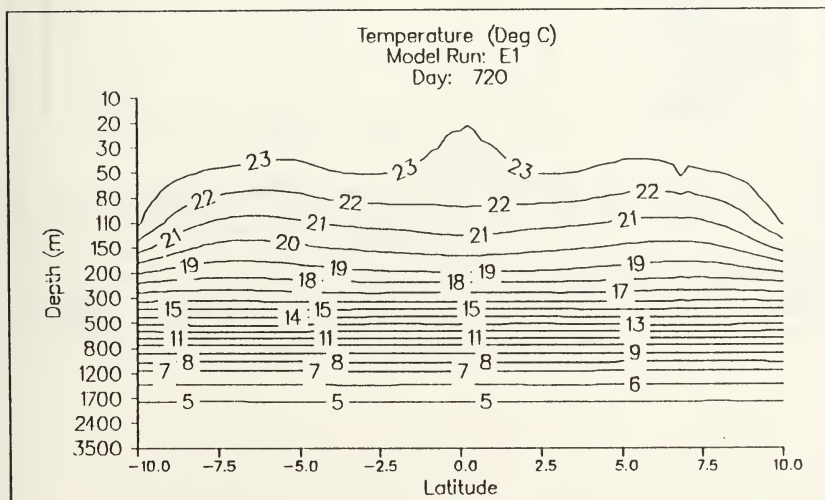


Figure 3.51. Experiment 1 temperature y-z cross section through mid-basin. Contour interval is 1.0°C.

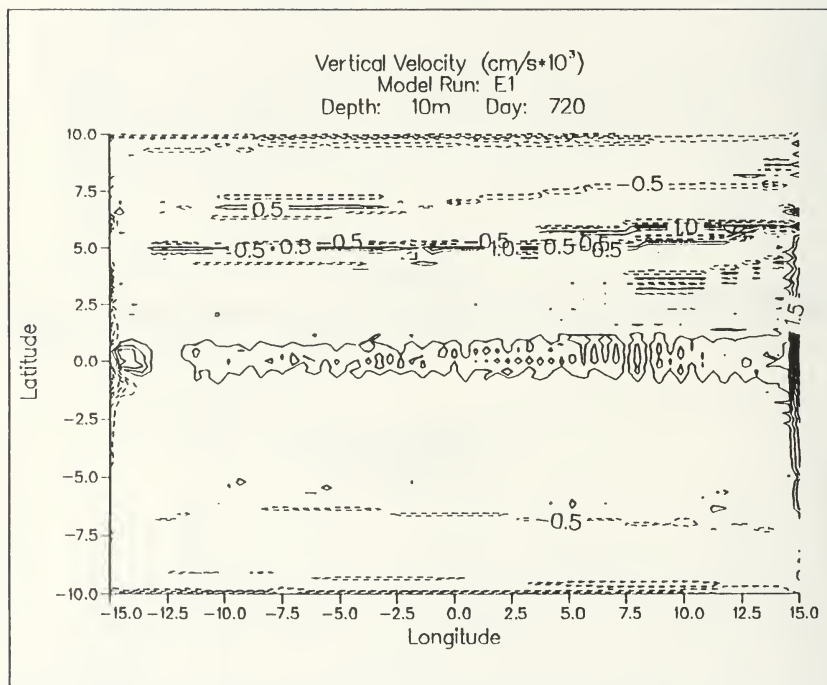


Figure 3.52. Experiment 1 10 m vertical velocity. Contour interval is $0.5 \times 10^3 \text{ cm/s}$. Solid lines depict positive values; dashed lines depict negative values.

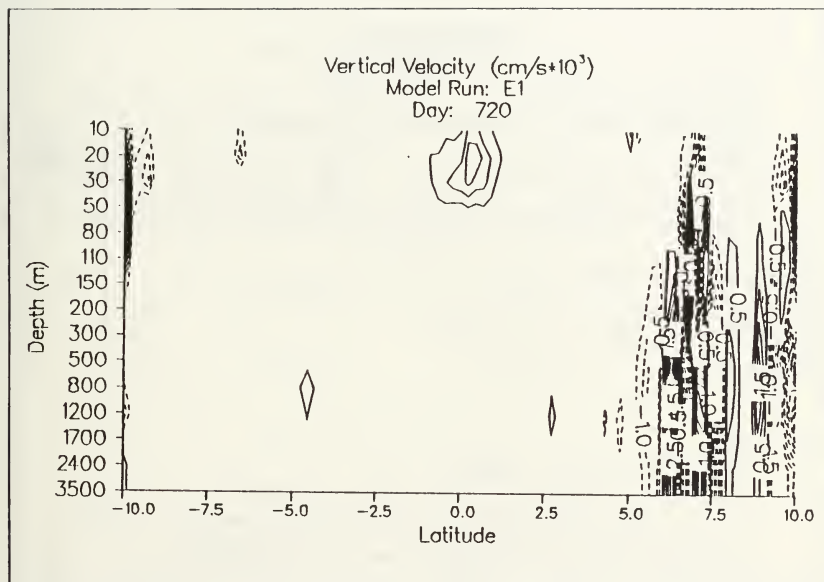


Figure 3.53. Experiment 1 vertical velocity y-z cross section through mid-basin. Contour interval is $0.5 \times 10^3 \text{ cm/s}$. Solid lines depict positive values; dashed lines depict negative values.

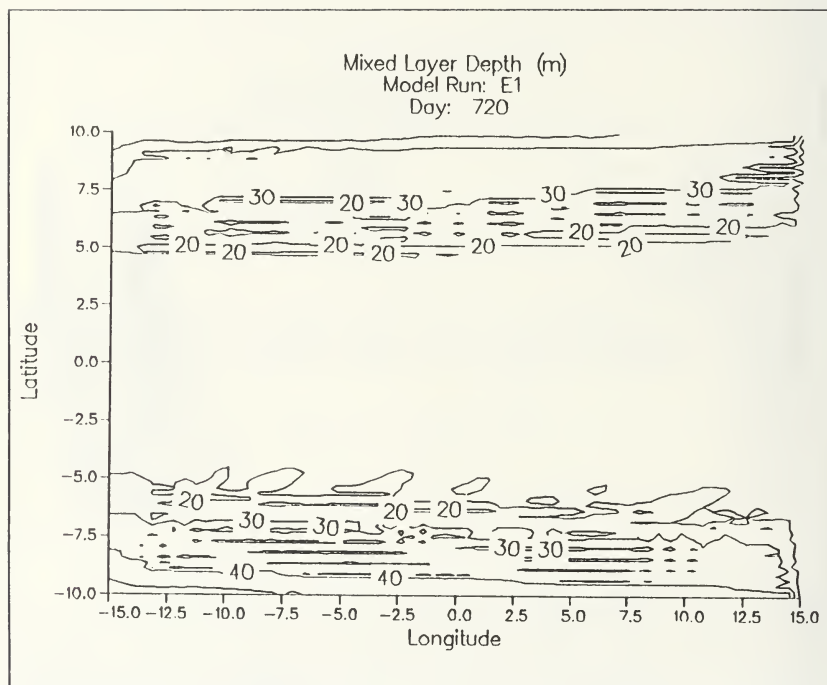


Figure 3.54. Experiment 1 mixed layer depth. Contour interval is 10 m.

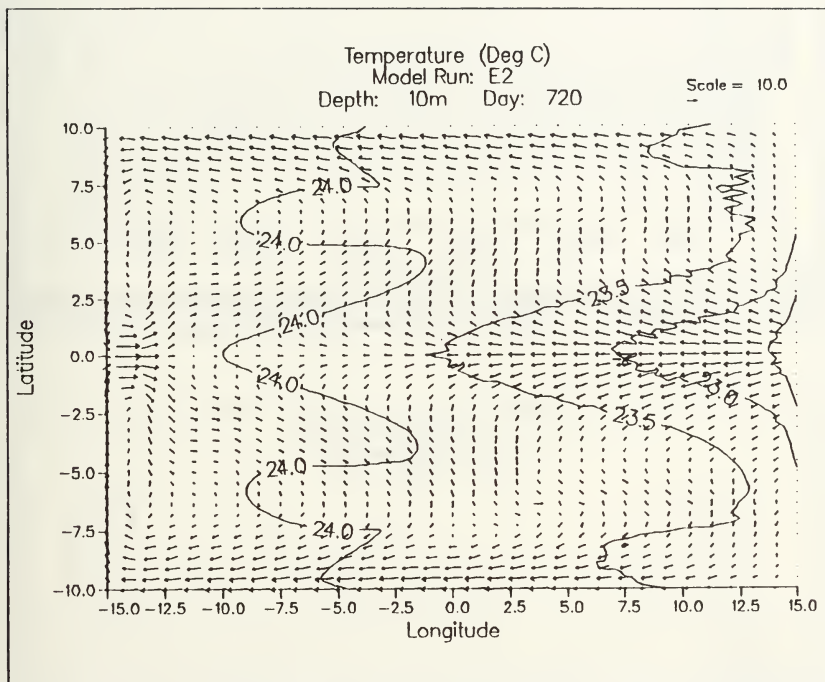


Figure 3.55. Experiment 2 10 m temperature and horizontal currents (cm/s). Contour interval is 0.5°C.

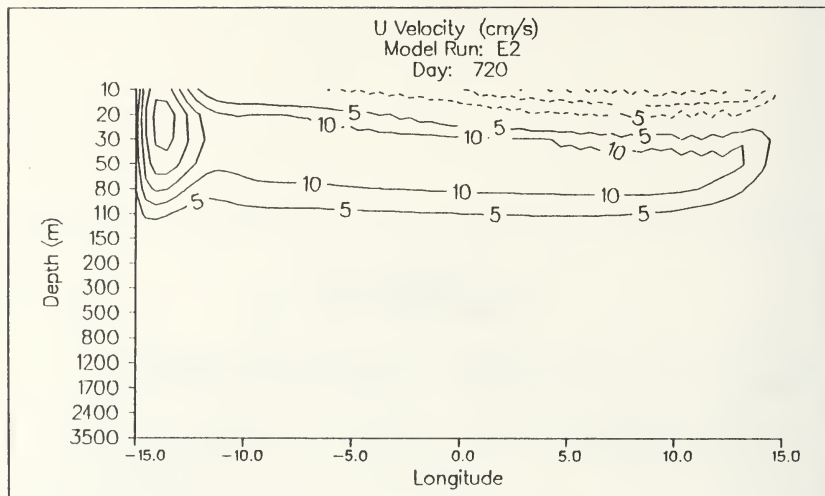


Figure 3.56. Experiment 2 zonal velocity x-z cross section along the equator. Contour interval is 5.0 cm/s.

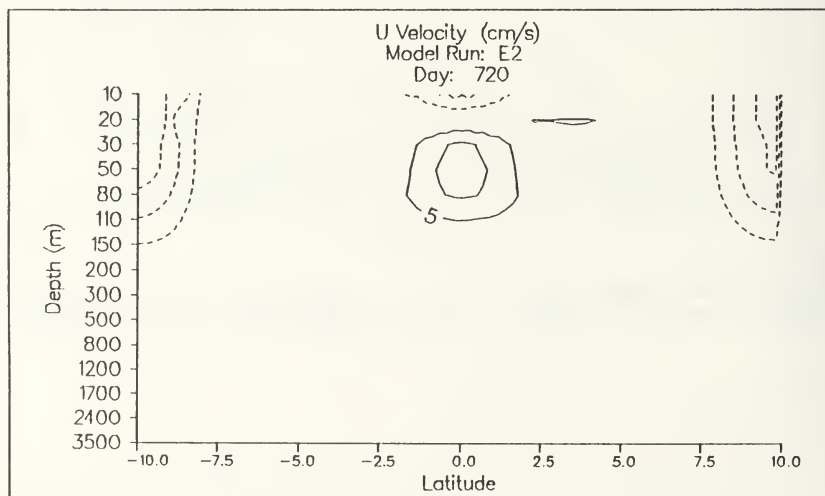


Figure 3.57. Experiment 2 zonal velocity y-z cross section through mid-basin. Contour interval is 5.0 cm/s.

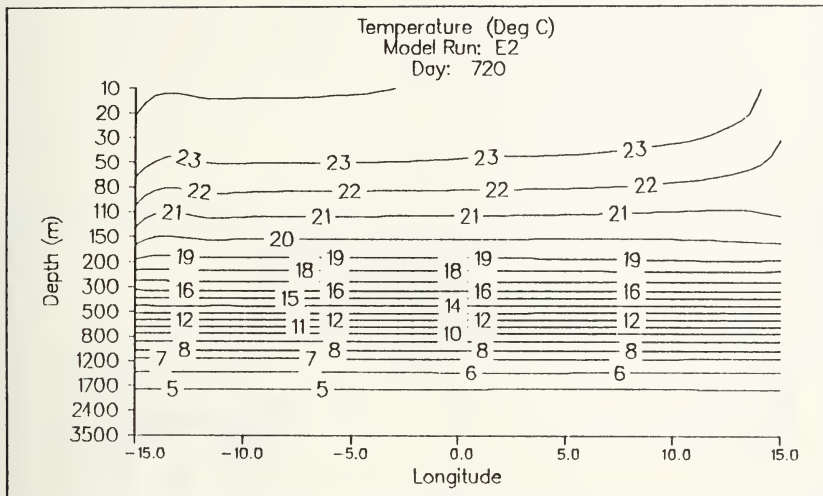


Figure 3.58. Experiment 2 temperature x-z cross section along the equator. Contour interval is 1.0°C .

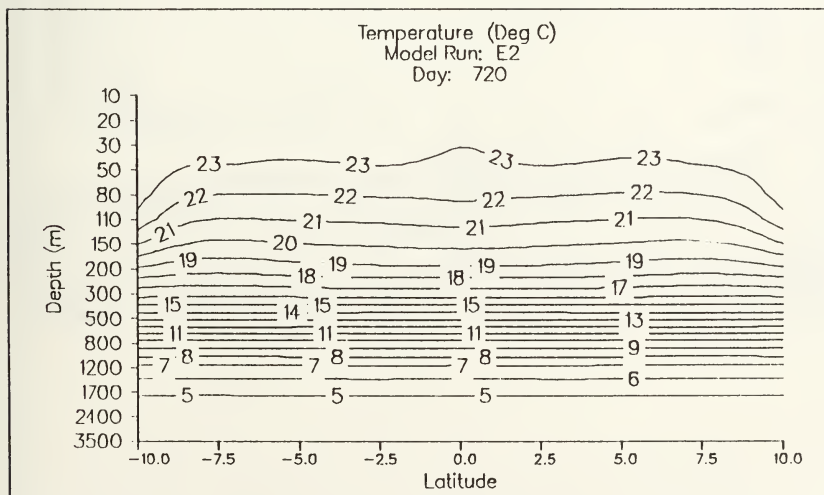


Figure 3.59. Experiment 2 temperature y-z cross section through mid-basin. Contour interval is 1.0°C .

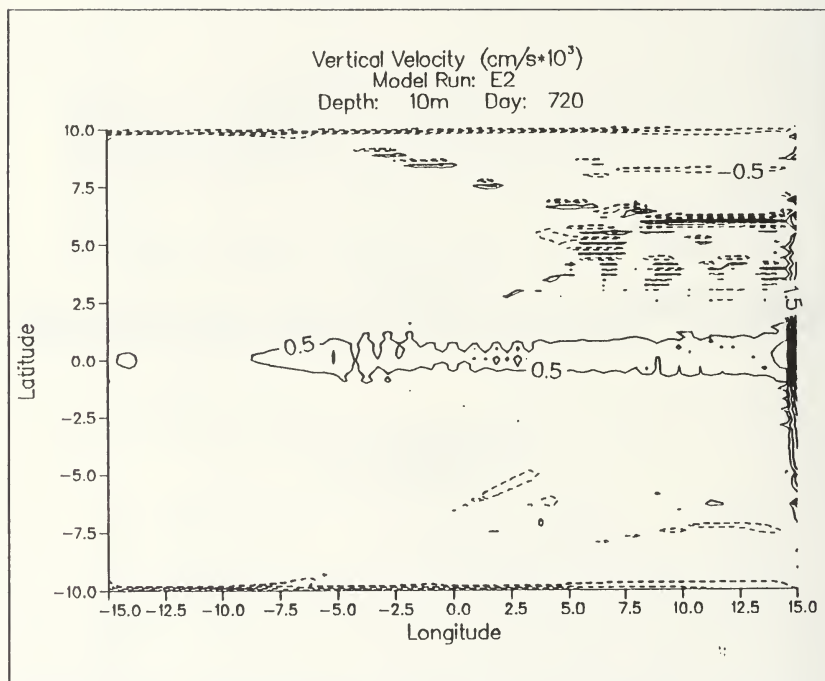


Figure 3.60. Experiment 2 10 m vertical velocity. Contour interval is 0.5×10^3 cm/s. Solid lines depict positive values; dashed lines depict negative values.

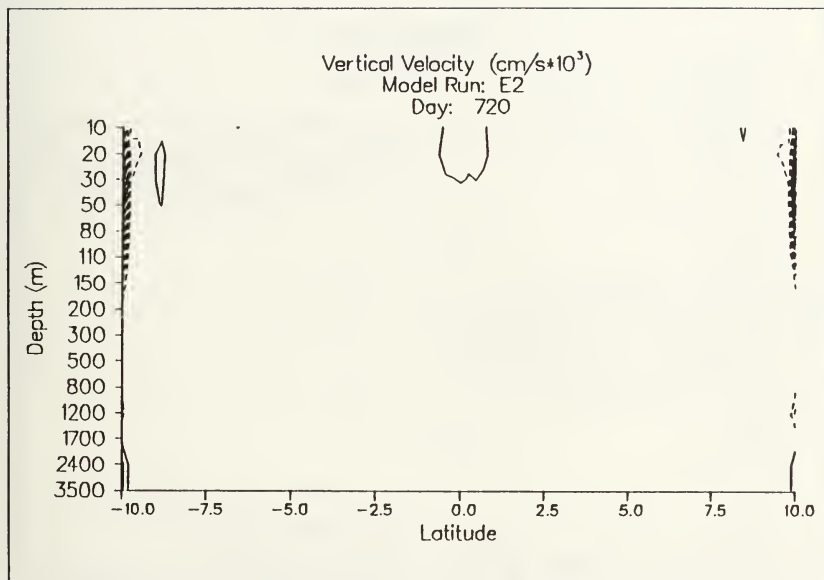


Figure 3.61. Experiment 2 vertical velocity y-z cross section through mid-basin. Contour interval is 0.5×10^3 cm/s. Solid lines depict positive values; dashed lines depict negative values.

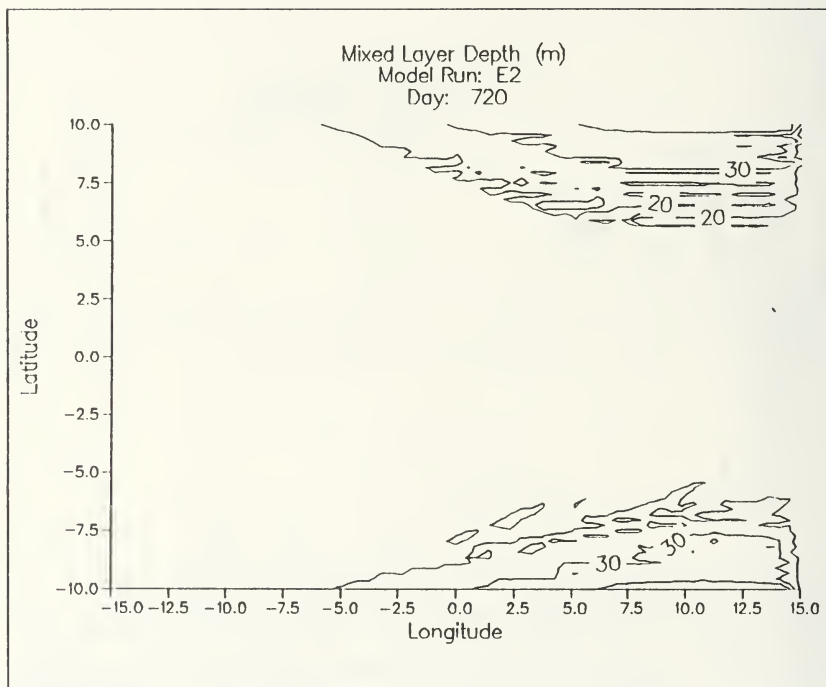


Figure 3.62. Experiment 2 mixed layer depth. Contour interval is 10 m.

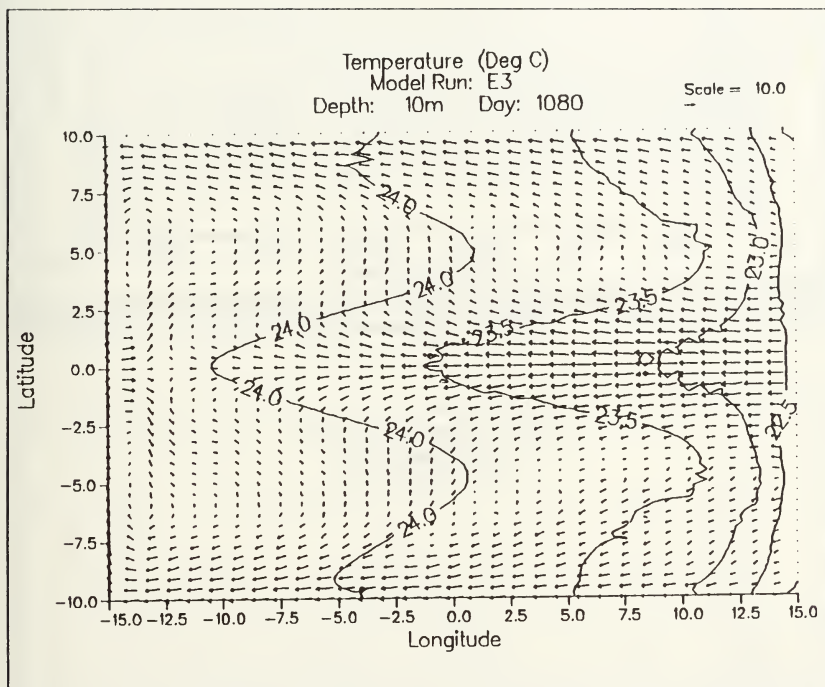


Figure 3.63. Experiment 3 10 m temperature and horizontal currents (cm/s). Contour interval is 0.5°C.

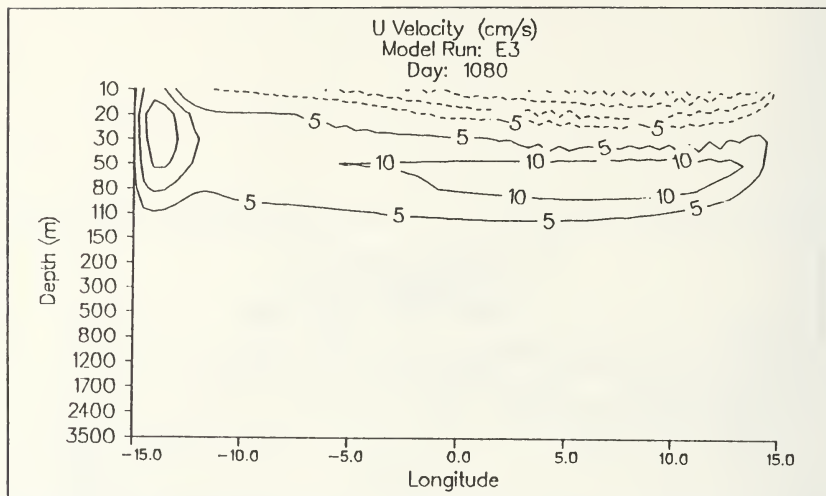


Figure 3.64. Experiment 3 zonal velocity x-z cross section along the equator. Contour interval is 5 cm/s.

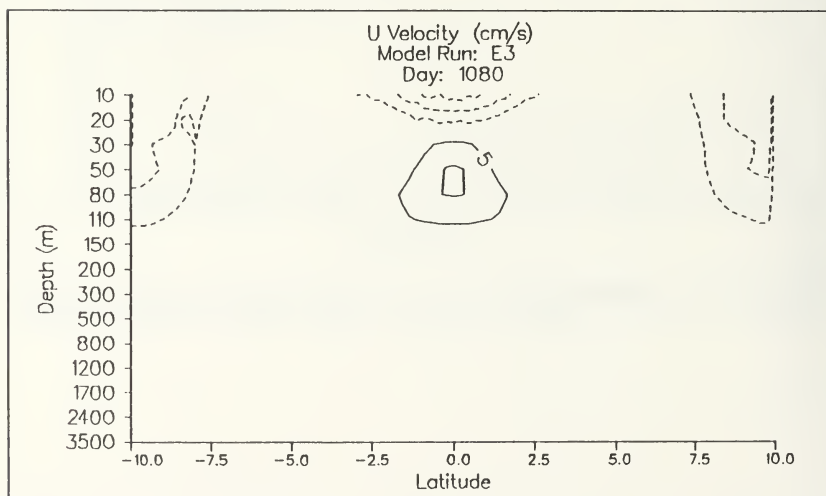


Figure 3.65. Experiment 3 zonal velocity y-x cross section through mid-basin. Contour interval is 5 cm/s.

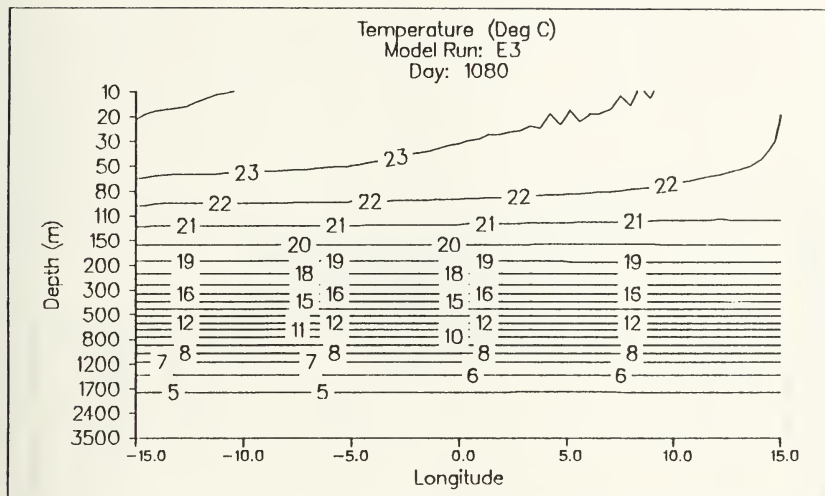


Figure 3.66. Experiment 3 temperature x-z cross section along the equator. Contour interval is 1.0°C .

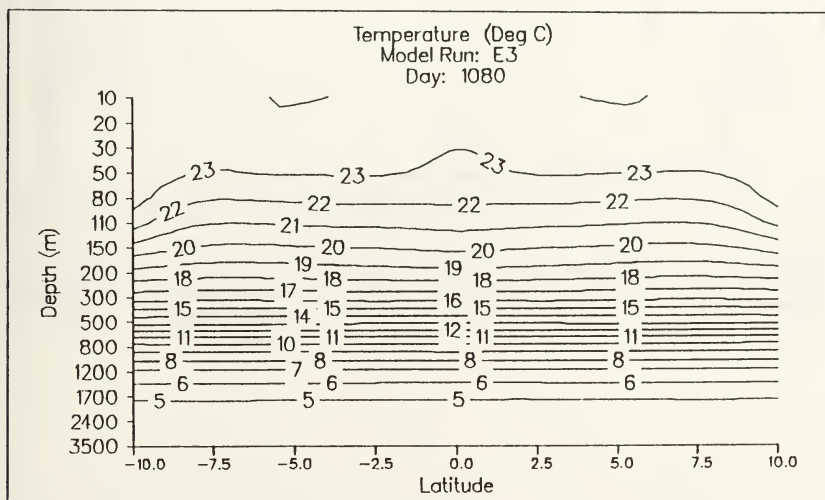


Figure 3.67. Experiment 3 temperature y-z cross section through mid-basin. Contour interval is 1.0°C .

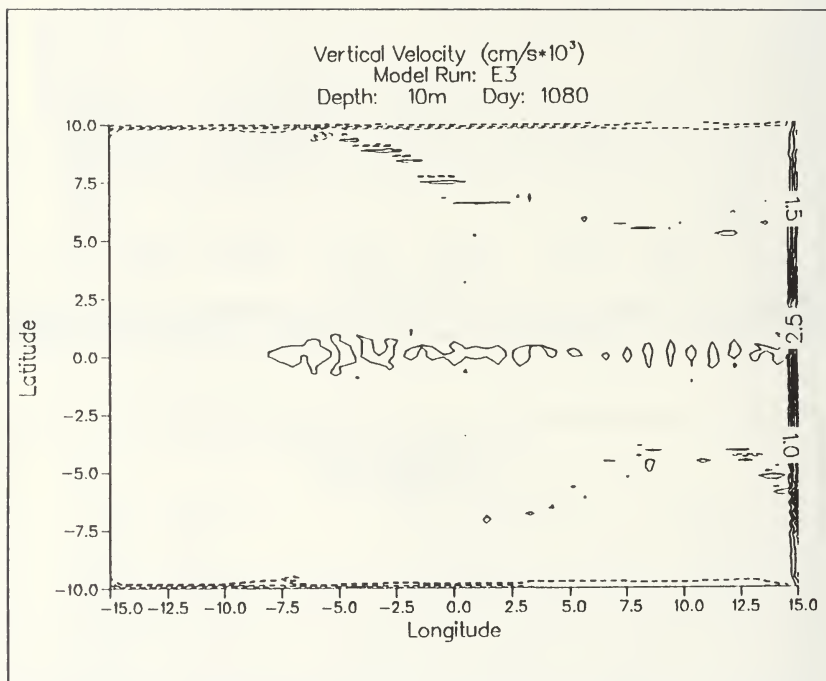


Figure 3.68. Experiment 3 10 m vertical velocity. Contour interval is $0.5 \times 10^3 \text{ cm/s}$. Solid lines depict positive values; dashed lines depict negative values.

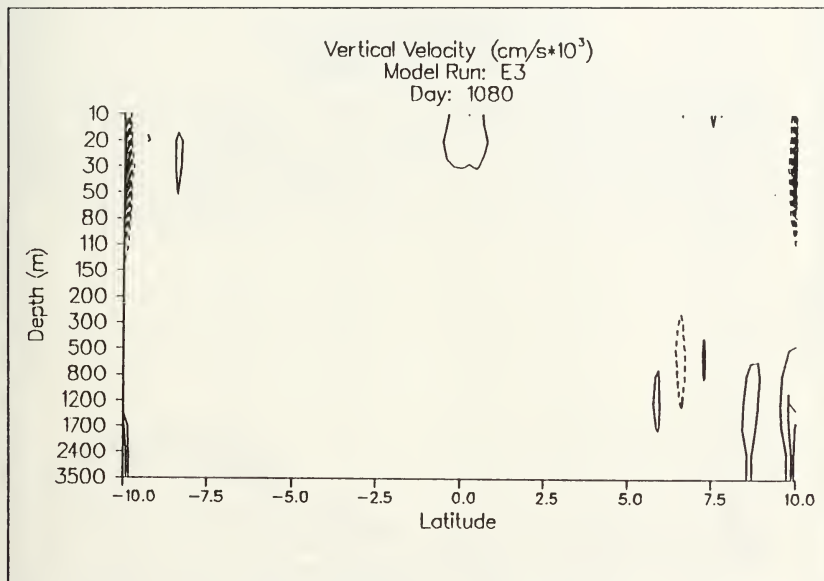


Figure 3.69. Experiment 3 vertical velocity y-z cross section through mid-basin. Contour interval is $0.5 \times 10^3 \text{ cm/s}$. Solid lines depict positive values; dashed lines depict negative values.

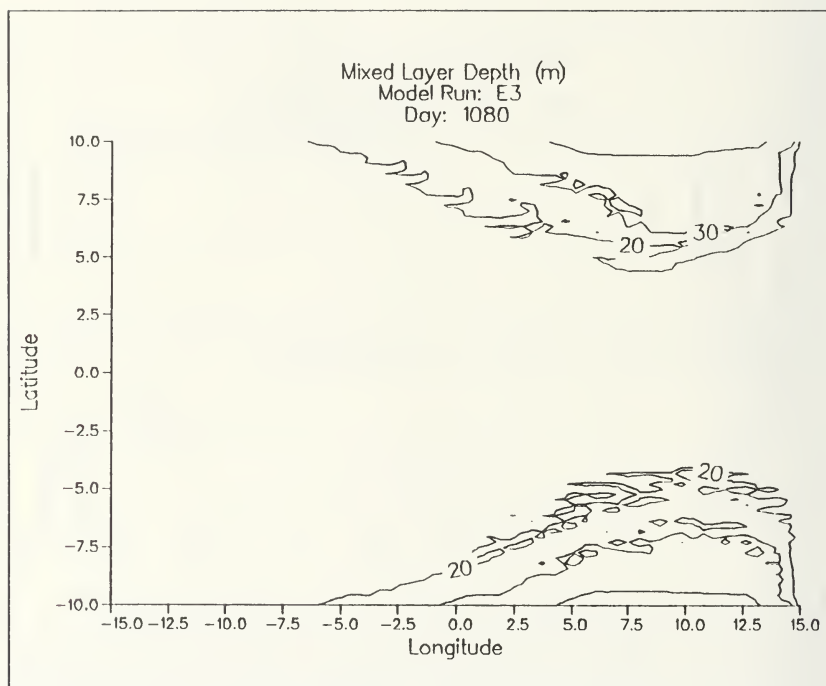


Figure 3.70. Experiment 3 mixed layer depth. Contour interval is 10 m.

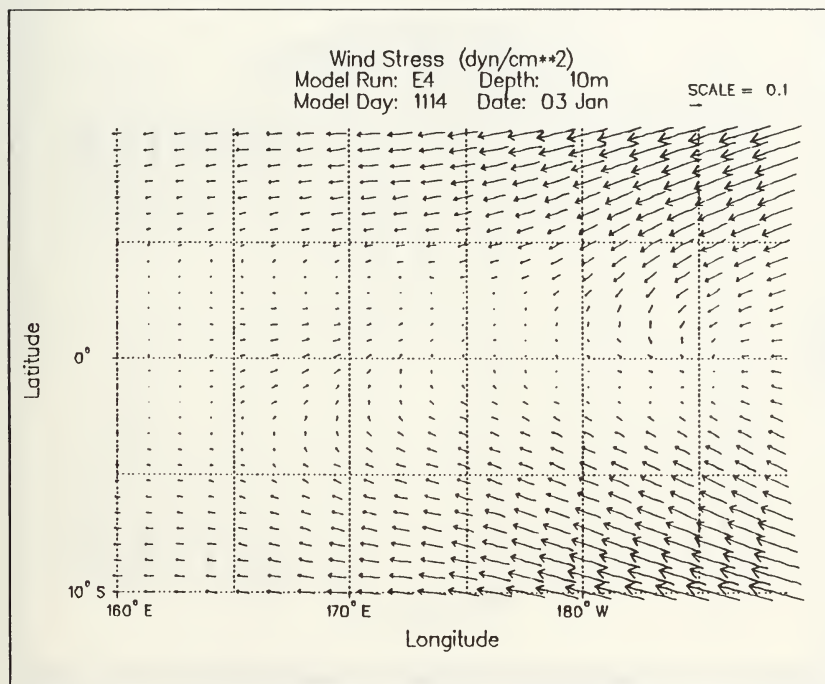


Figure 3.71. Experiment 4 wind stress (dyns/cm²) for model day 1114: Note the westerly wind event in the western basin.

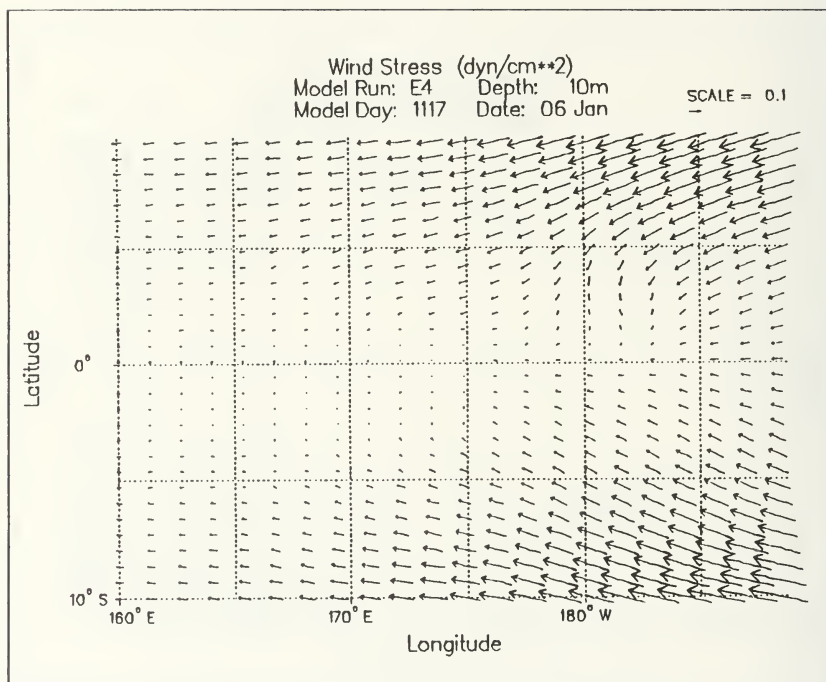


Figure 3.72. Experiment 4 wind stress (dyns/cm²) for model day 1117: Note that the westerly event in the western basin has dissipated.

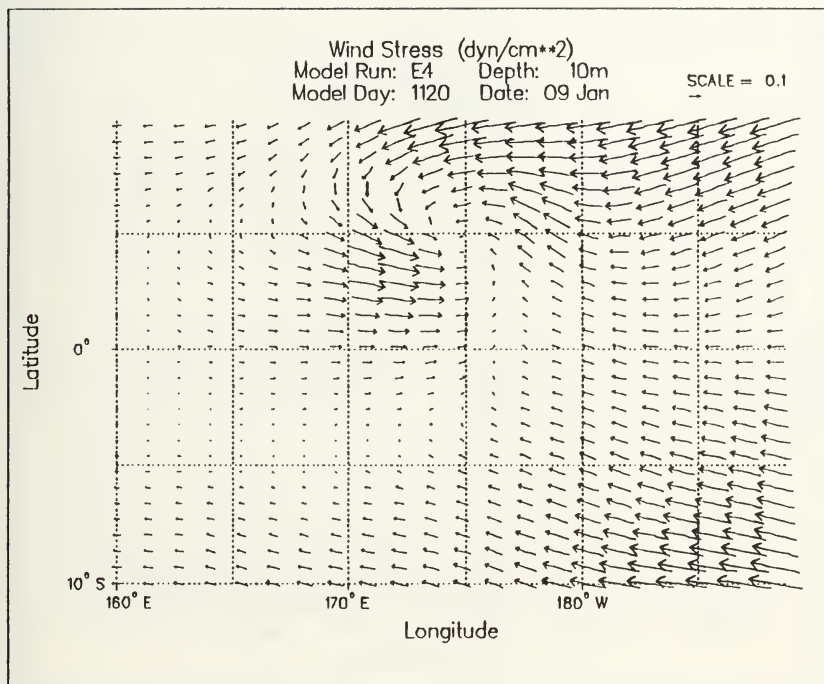


Figure 3.73. Experiment 4 wind stress (dyn/cm^2) for model day 1120: Note the westerly wind event in the mid-basin associated with Typhoon Axel.

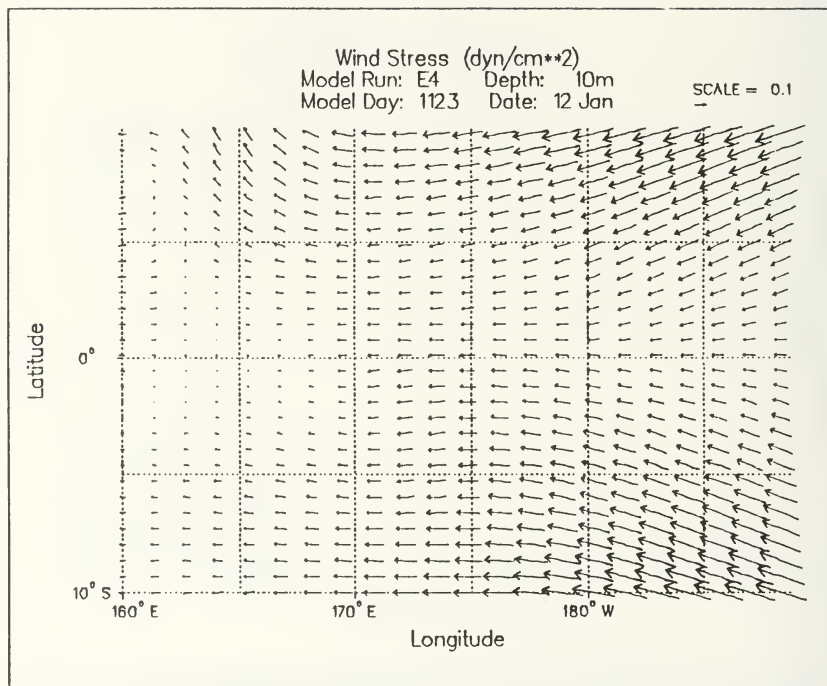


Figure 3.74. Experiment 4 wind stress (dyns/cm²) at model day 1123: Note the resurgence in westward wind stress.

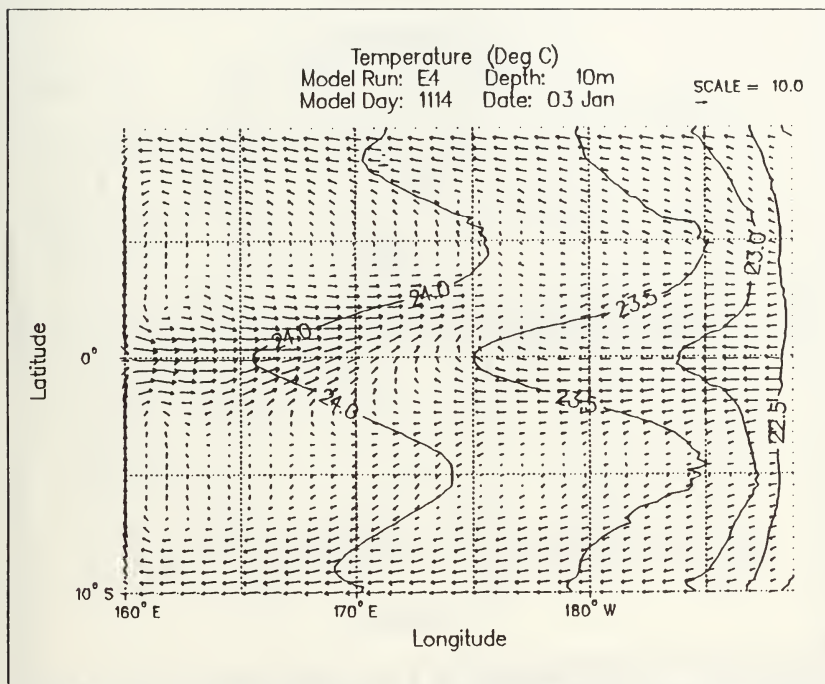


Figure 3.75. Experiment 4 10 m temperature and horizontal currents (cm/s) for model day 1114: Note the reversal of the SEC in the western basin. Contour interval is 0.5°C.

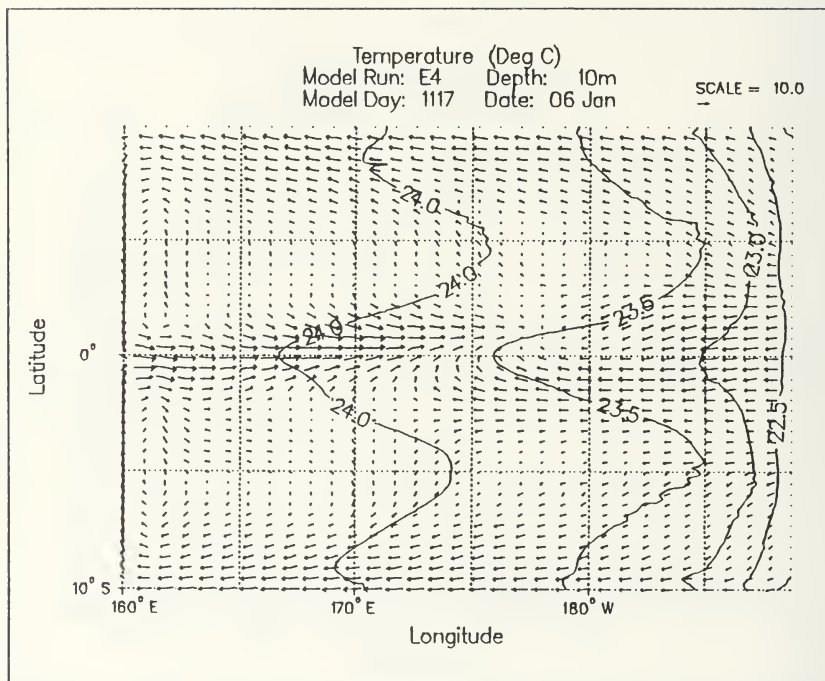


Figure 3.76. Experiment 4 10 m temperature and horizontal currents (cm/s) for model day 1117: Note the diminished reversal of the SEC in the western basin. Contour interval is 0.5°C.

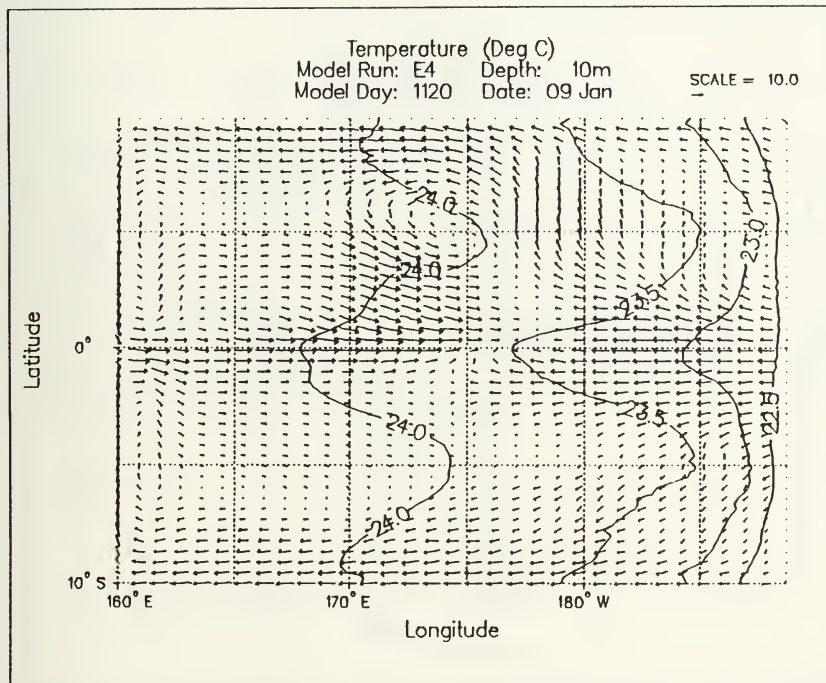


Figure 3.77. Experiment 4 10 m temperature and horizontal currents (cm/s) for model day 1120: Note the eastward currents in the mid-basin region associated with Typhoon Axel. Contour interval is 0.5°C.

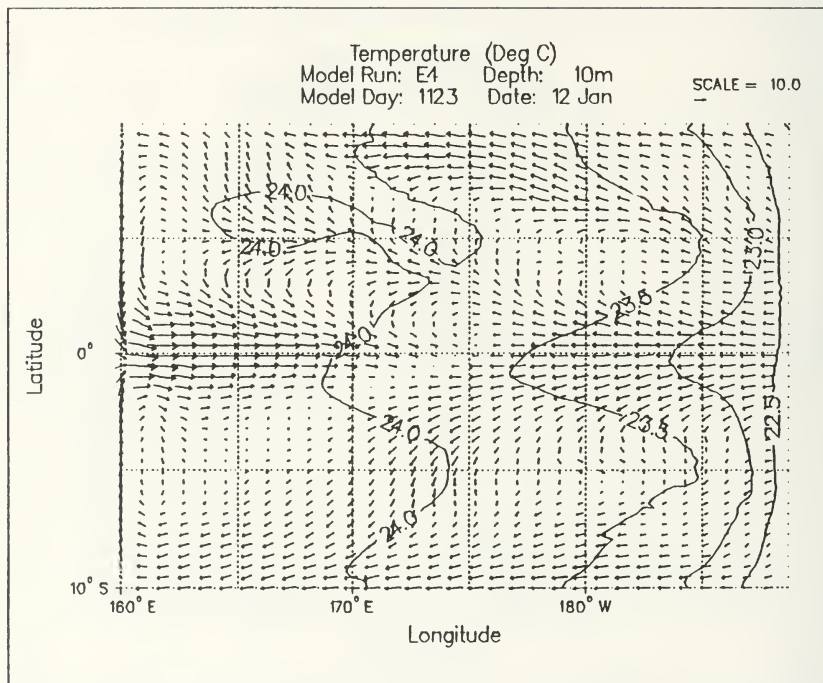


Figure 3.78. Experiment 4 10 m temperature and horizontal currents (cm/s) for model day 1123: Note the cold protrusion along approximately 5°N and the strengthening of the SEC extending from the eastern boundary. Contour interval is 0.5°C.

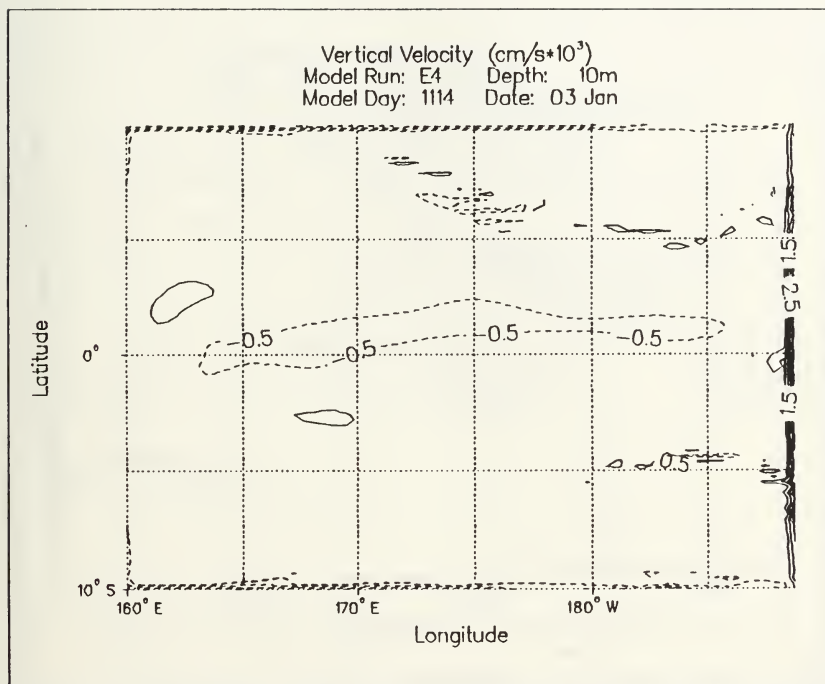


Figure 3.79. Experiment 4 10 m vertical velocity for model day 1114: Note the downwelling area along the equator. Contour interval is 0.5×10^3 cm/s.

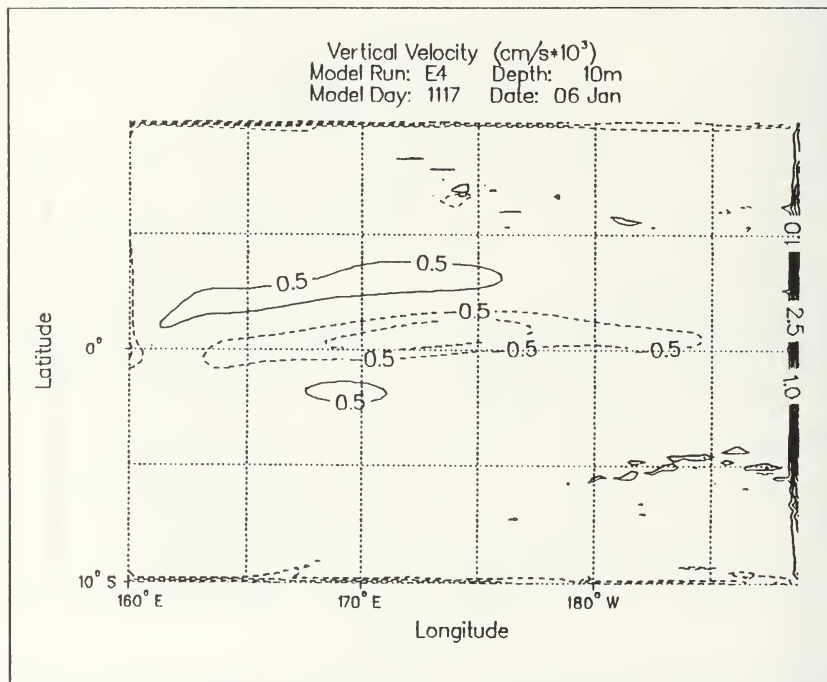


Figure 3.80. Experiment 4 10 m vertical velocity for model day 1117: Note the enhanced downwelling area along the equator near the mid-basin region. Contour interval is 0.5×10^3 cm/s.

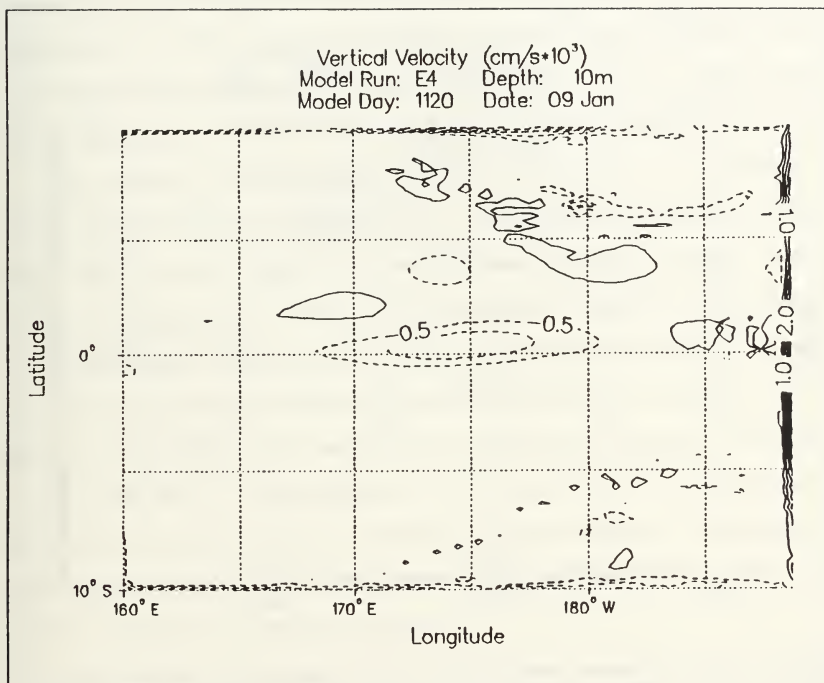


Figure 3.81. Experiment 4 10 m vertical velocity for model day 1120: Note the diminished extent of the downwelling area along the equator and the upwelling/downwelling associated with Typhoon Axel. Contour interval is 0.5×10^3 cm/s.

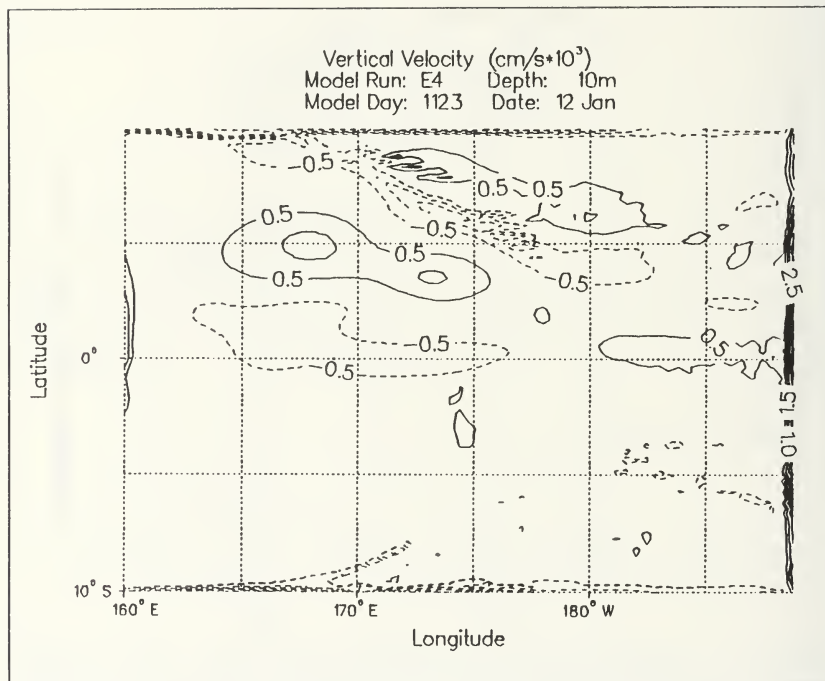


Figure 3.82. Experiment 4 10 m vertical velocity for model day 1123: Note the reduced downwelling in the western basin, enhanced upwelling in eastern basin along the equator, and the upwelling region associated with the cold protrusion shown in Figure 3.78. Contour interval is 0.5×10^3 cm/s.

IV. SUMMARY

A. DISCUSSION

In a planned series of developmental and experimental numerical simulations, a primitive equation ocean general circulation model with embedded mixed layer physics was developed and applied to the equatorial ocean. The upper ocean response to westerly wind events was then investigated.

At the end of the developmental phase, a model formulation was achieved that realistically simulated the steady-state equatorial ocean. The 10 m temperature pattern (Figure 3.21) for developmental run DRM2 (including full mixed layer physics of entrainment and Richardson number mixing) is similar to the results obtained by Semtner and Holland (1980) (Figure 4.1). Zonal and meridional temperature profiles (Figures 3.24 and 3.25) are also comparable to the results of Semtner and Holland (1980) (Figures 4.2a&b). Additionally, the model's depiction of the EUC is similar to Semtner and Holland's work (1980) (Figures 4.3a&b).

Inclusion of mixed layer physics should allow more realistic simulation of time-dependent air-sea interactions than is possible with earlier models. However, the model simulations were not completely without problems. The mixed layer depth field is one of the more noisy model fields. The

mixed layer depth field contained shallow mixed layer cells on a small space scale (Figure 3.20) which may be evidence of numerical instability. However, as the mixed layer depth represents the base of the turbulent boundary layer in the model, the model's mixed layer depth may be more complex and unsteady than alternately defined mixed layer depths (e.g., a mixed layer depth based on a specified temperature gradient). Further investigations of a mixed layer depth field based on a thermocline representation are needed to determine the significance and extent of the problem.

Despite localized problematic features in the mixed layer depth, the model ocean's response to the various wind stresses in the experimental phase was credible. When the wind stress used in experimental run E1 was decreased to a relative minimum on the equator from the horizontally uniform wind stress used in the developmental runs, simulating a westerly wind event, the model produced a reversal in the SEC in the western basin and countercurrents along approximately 5°N and 5°S (Figure 3.47). The zonal profile of zonal velocity along the equator (Figure 3.48) depicts a local maximum in eastward velocity near the western boundary at a depth of approximately 30 m. The EUC also shallowed by approximately 150 m and weakened in maximum intensity by approximately 5 cm/s. The pattern of the mixed layer depths was qualitatively similar to the wind stress field. The mixed layer was deepest near the poleward boundaries, where the wind stress was largest, and

shallower towards the equator, where the wind stress was smallest.

In experimental run E3, the wind stress (Figure 3.46) had sufficient complexity to realistically represent the annual mean wind stress for the western Pacific (Figure 4.4). The westward wind stress decreased from the equator to the poleward boundaries, and from the eastern boundary to the western boundary. The addition of an equatorward meridional component in the wind stress, which also decreased from west to east, produced a weakening of the reversal in the SEC at the western boundary (cf. Figures 3.47 and 3.63). The model's off-equatorial countercurrents, though weaker in magnitude, coincided with the zonally-aligned areas of probable downwelling (Figure 3.67). This pattern corresponds to the downwelling associated with the NECC and SECC in the real ocean (Pond and Pickard, 1983). In addition, the profile along the equator of the zonal velocity (Figure 3.64) shows that the local maximum in eastward velocity near the western boundary has decreased in intensity. The EUC core maximum has also decreased in intensity as well as forming a separate local maximum in the eastern basin where the wind stress magnitude is larger. Again, the mixed layer depth was qualitatively similar to the wind stress. The mixed layer depth decreased from the poleward boundaries towards the equator and also decreased from east to west, as did the wind

stress. Thus, the mixed layer is deeper generally where the wind stress is stronger.

At the western boundary, the model produced equatorward currents in contrast to the poleward western boundary currents that are observed in the real ocean. The convergence in the vicinity of the equator that results from the equatorward western boundary currents may be the cause of the persistent local maximum in eastward flow along the equator in the western basin. This feature is most likely related to the closed boundaries to the north and south.

B. CONCLUSIONS

Smaller domains required more realistic wind stress fields to achieve reasonable current structures. It wasn't until a meridionally-varying wind stress was included in experimental run E1 that off-equatorial countercurrents formed in the small domain. In addition, off-equatorial currents were particularly responsive to changes in the zonal gradient of the wind stress. When the wind stress included only a zonally-varying zonal component in experimental run E2, the model's countercurrents were significantly less developed. However, when a zonally-varying meridional component was added in run E3, the model's NECC and SECC strengthened and had a realistic association with the model's vertical velocity field.

The January 1992 westerly wind events produced both local and remote responses (see Chapter III, Section B). The local responses in the western basin included a reversal in the South Equatorial Current, along with downwelling and a thermocline depression. The reversals in the SEC were approximately coincident in time with the westerly wind events, while the downwelling response and thermocline depression appeared to lag the westerly wind events by a few days. The remote responses across the basin included indications of the excitation of an equatorial Kelvin wave. The model's responses to the January 1992 westerly wind events are consistent with the observational study done by Cooper (1992).

C. RECOMMENDATIONS

Although the model at its current stage of development adequately simulates the equatorial ocean's temperature and current structure, a variety of improvements are recommended, e.g., increasing the domain size of the model to a more realistic extent. Changing the northern and southern boundary conditions to allow realistic western boundary currents to form would greatly enhance model simulations. Additionally, model simulations could be improved through the incorporation of a diurnal heating cycle and a biharmonic diffusion parameterization in place of the current Laplacian diffusion parameterization. The inclusion of salinity could also

improve model simulations, especially in the western domain. These suggested improvements are far from all-encompassing.

As the majority of the effort during this study was on model development, the experimental stage was necessarily brief. Many additional experiments could be performed. For example, the total NOGAPS wind fields could be used to produce a much longer time series for the wind stress surface boundary condition. In addition, NOGAPS boundary layer temperatures could be used to compute the surface heat flux which could be used to thermodynamically force the model in conjunction with the NOGAPS wind fields. During the course of this study, the model has proven to be very resilient and capable of handling sudden strong changes in the wind stress quite well. The relatively successful simulation of the equatorial ocean during this study suggests that the model can be a useful tool in additional studies of tropical air-sea interaction.

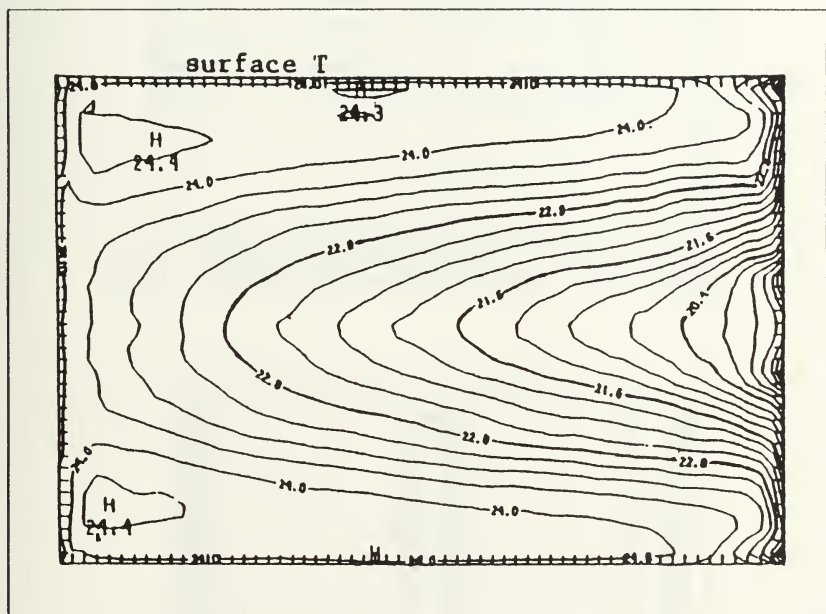


Figure 4.1. Surface temperature contours after Semtner and Holland (1980).

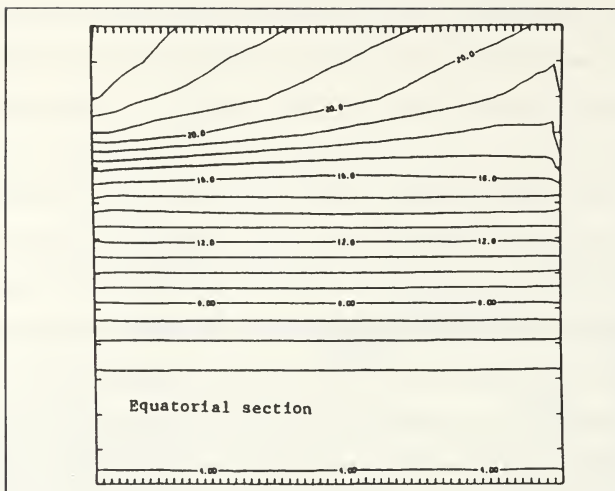


Figure 4.2a. Zonal temperature profile along the equator after Semtner and Holland (1980).

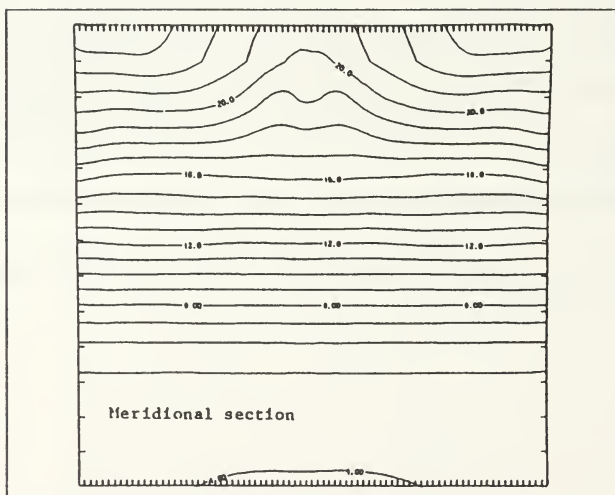


Figure 4.2b. Meridional temperature profile after Semtner and Holland (1980).

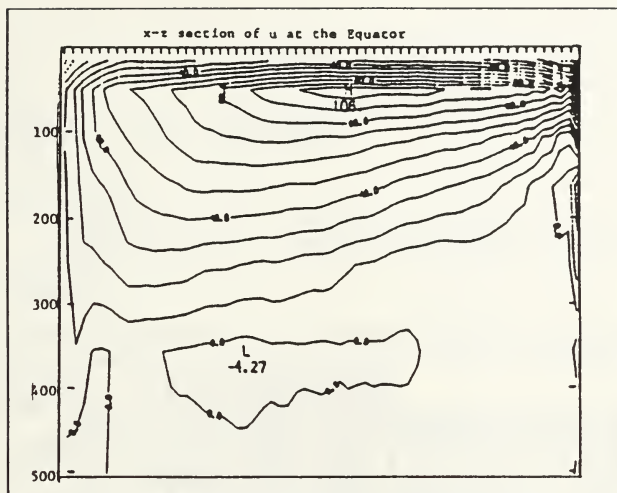


Figure 4.3a. Zonal profile of zonal velocity along the equator after Semtner and Holland (1980).

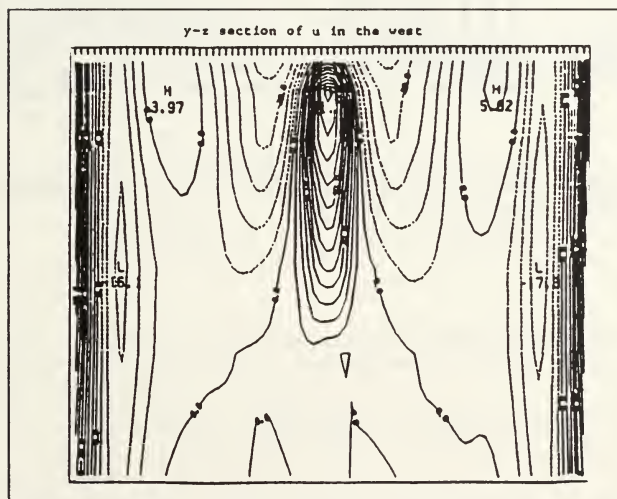


Figure 4.3b. Meridional profile of zonal velocity in the western basin after Semtner and Holland (1980).

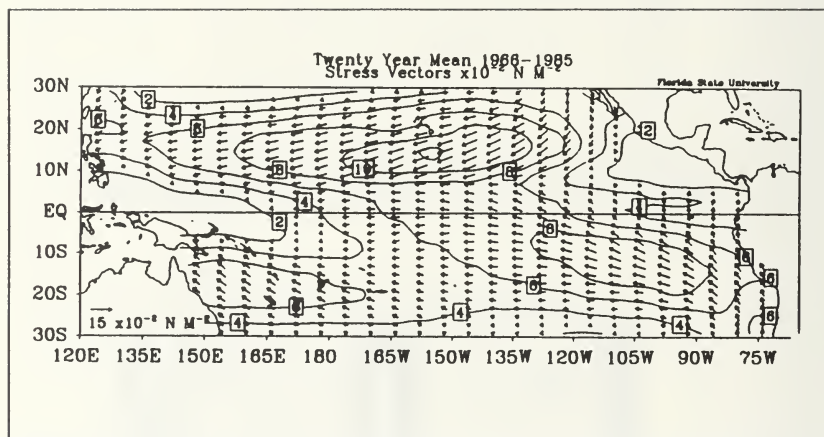


Figure 4.4. Mean wind stress vectors for the tropical Pacific after Stricherz et al. (1992).

APPENDIX

A. EXPERIMENT 1 WIND STRESS CODE

```

PI=4*ATAN(1.0)
DO II=1,44
    TAUXX(II+45) = -.4*SIN(4/3*PI*II/90 - PI/2) - .5
    TAUXX(45-II) = -.4*SIN(4/3*PI*II/90 - PI/2) - .5
END DO
TAUXX(45) = -.1

```

C PCT is the fraction of the two week ramp-in period through
 C which the model has been integrated. PCT is always less
 C than or equal to 1.

```

IF (PCT .LT. 1.) THEN
    TAUXX = TAUXX - PCT*(TAUXX - TAUXX(I,J))
ELSE
    TAUXX = TAUXX(I,J)
END IF

```

B. EXPERIMENT 2 WIND STRESS CODE

```

PI=4*ATAN(1.0)
DO II=1,44
    TAUXX(II+45) = -.4*SIN(4/3*PI*II/90 - PI/2) - .5
    TAUXX(45-II) = -.4*SIN(4/3*PI*II/90 - PI/2) - .5
END DO
TAUXX(45) = -.1
DO II= 1,IM
    COEF(II) = .4*COS((II-1)*PI/65 - PI)+.6
END DO
DO II = 1,IM
    DO JJ = 1,JM
        TAUXX(II,JJ) = COEF(II) * TAUXX(JJ)
    END DO
END DO

```

C PCT is the fraction of the two week ramp-in period through
 C which the model has been integrated. PCT is always less
 C than or equal to 1.

```

IF (PCT .LT. 1.) THEN
    TAUXX = TAUXX - PCT*(TAUXX - TAUXX(I,J))
ELSE
    TAUXX = TAUXX(I,J)
END IF

```

C. EXPERIMENT 3 WIND STRESS CODE

```

PI=4*ATAN(1.0)
DO II=1,44
    TAUXX(II+45) = -.4*SIN(4/3*PI*II/90 - PI/2) - .5
    TAUXX(45-II) = -.4*SIN(4/3*PI*II/90 - PI/2) - .5
END DO
TAUXX(45) = -.1
DO II= 1,IM
    COEF(II) = .4*COS((II-1)*PI/65 - PI)+.6
END DO
DO II = 1,20
    XCOEF(II) = .01 + (II/20.)*.09
END DO
DO II = 21,IM
    XCOEF(II) = .45*COS((II-21)*PI/44 - PI) + .55
END DO
DO JJ=1,JM
    TAUYJ(JJ) = .3*COS(PI*JJ/(JM+1))
END DO
DO II = 1,IM
    DO JJ = 1,JM
        TAUXY(II,JJ) = COEF(II) * TAUXX(JJ)
        TAUYX(II,JJ) = TAUYJ(JJ)*XCOEF(II)
    END DO
END DO

```

C PCT is the fraction of the two week ramp-in period through
C which the model has been integrated. PCT is always less
C than or equal to 1.

```

IF (PCT .LT. 1.) THEN
    TAUX = TAUX - PCT*(TAUX - TAUXY(I,J))
ELSE
    TAUX = TAUXY(I,J)
END IF
IF (RAMP .LT. 1.) THEN
    TAUY = TAUY - RAMP*(TAUY - TAUYX(I,J))
ELSE
    TAUY = TAUYX(I,J)
END IF

```

Note: These segments of code are designed for a domain size with 65 gridpoints in x and 89 gridpoints in y.

REFERENCES

Adamec, D., R. L. Elsberry, R. W. Garwood, Jr., and R. L. Haney, 1981: An embedded mixed-layer--ocean circulation model.

Cane, M. A., 1979: The response of an equatorial ocean to simple wind stress patterns: I. Model formulation and analytic results. *J. Mar. Res.*, **37**, 233-252.

Cane, M. A., 1979: The response of an equatorial ocean to simple wind stress patterns: II. Numerical results. *J. Mar. Res.*, **37**, 253-299.

Chu, P. S., 1988: Extratropical forcing and the burst of equatorial westerlies in the western Pacific: a synoptic study. *J. Meteor. Soc. Japan*, **66**, 549-564.

Chu, P. C. and R. W. Garwood, Jr., 1990: Thermodynamical feedback between clouds and ocean mixed layer. *Adv. Atmos. Sci.*, **7**, 1-10.

Cooper, G. A., 1992: Local and remote response of the equatorial Pacific Ocean to westerly wind bursts: An observational study. Master's Thesis, Naval Postgraduate School, Monterey, California.

Garwood, R. W., 1977. An oceanic mixed layer model capable of simulating cyclic states. *J. Phys. Oceanogr.*, **7**, 455-468.

Garwood, R. W., Jr., P. C. Gallacher, and P. Muller, 1985: Wind direction and equilibrium mixed layer depth: general theory. *J. Phys. Oceanogr.*, **15**, 1325-1331.

Garwood, R. W., Jr., P. Muller, and P. C. Gallacher, 1985: Wind direction and equilibrium mixed layer depth in the tropical Pacific Ocean. *J. Phys. Oceanogr.*, **15**, 1332-1338.

Garwood, R. W., Jr., P. C. Chu, P. Muller, and N. Schneider, 1989: Equatorial entrainment zone: The diurnal cycle. Proceedings Western Pacific international meeting on TOGA COARE, Centre ORSTOM de Noumea, New Caledonia, 435-443.

Giese, B. S. and D. E. Harrison, 1991: Eastern equatorial Pacific response to three composite westerly wind types. *J. Geophys. Res.*, **96**, 3239-3248.

Giese, B. S. and D. E. Harrison, 1990: Aspects of kelvin wave response to episodic wind forcing. *J. Geophys. Res.*, **95**, 7289-7312.

Gill, A. E., 1982: *Atmosphere-Ocean Dynamics*. Academic Press, Inc., San Diego, California, 662 pp.

Gordon, C. and R. A. Corry, 1991: A model simulation of the seasonal cycle in the tropical Pacific Ocean using climatological and modeled surface forcing. *J. Geophys. Res.*, **96**, 847-864.

Haney, R. L., 1971: Surface thermal boundary condition for ocean circulation models. *J. Phys. Oceanogr.*, **4**, 241-248.

Haney, R. L., 1974: A numerical study of the response of an idealized ocean to large-scale surface heat and momentum flux. *J. Phys. Oceanogr.*, **4**, 145-167.

Harrison, D. E. and B. S. Giese, 1991: Episodes of surface westerly winds as observed from islands in the western tropical Pacific. *J. Geophys. Res.*, **96**, 3221-3237.

Harrison, D. E. and B. S. Giese, 1988: Remote westerly wind forcing of the eastern equatorial Pacific; some model results. *Geophys. Res. Lett.*, **15**, 804-807.

Harrison, D. E. and P. S. Schopf, 1984: Kelvin-wave-induced anomalous advection and the onset of surface warming in El Nino events. *Mon. Wea. Rev.*, **112**, 923-933.

Keen, R. A., 1982: The role of cross-equatorial tropical cyclone pairs in the southern oscillation. *Mon. Wea. Rev.*, **110**, 1405-1416.

Latif, M., 1987: Tropical ocean circulation experiments. *J. Phys. Oceanogr.*, **17**, 246-263.

Legeckis, R., W. Pichel, and G. Nesterczuk, 1983: Equatorial long waves in geostationary satellite observations and in a multichannel sea surface temperature analysis. *Bull. Am. Met. Soc.*, **64**, 133-139.

Luther, D. S., D. E. Harrison, and R. Knox, 1983: Zonal winds in the central equatorial Pacific and the onset of El Nino. *Science*, **222**, 327-330.

McCreary, J., 1976: Eastern tropical ocean response to changing wind systems: with application to El Nino. *J. Phys. Oceanogr.*, **6**, 632-645.

- McCreary, J., 1983: A model of tropical ocean-atmosphere interaction. *Mon. Wea. Rev.*, **111**, 370-387.
- McPhaden, M. J., H. P. Freitag, S. P. Hayes, B. A. Taft, S. Chen, and K. Wyrtki, 1988: The response of the equatorial Pacific Ocean to a westerly wind burst in May 1986. *J. Geophys. Res.*, **93**, 10589-10603.
- Miller, A. J., J. M. Oberhuber, N. E. Graham, and T. P. Barnett, 1992: Tropical Pacific Ocean response to observed winds in a layered general circulation model. *J. Geophys. Res.*, **97**, 7317-7340.
- Murakami, T. and W. L. Sumathipala, 1989: Westerly bursts during the 1982/83 ENSO. *J. Climate*, **2**, 71-85.
- Philander, S. G. H., 1981: The response of equatorial oceans to a relaxation of the trade winds. *J. Phys. Oceanogr.*, **11**, 176-189.
- Pond S. and G. L. Pickard, 1983: *Introductory Dynamical Oceanography*, Pergamon Press, Oxford, England, 329 pp.
- Rasmusson, E. M. and T. H. Carpenter, 1982: Variations in tropical sea surface temperature and surface wind fields associated with the Southern Oscillation/El Nino. *Mon. Wea. Rev.*, **110**, 354-384.
- Riehl, H., 1979: *Climate and weather in the tropics*. Academic Press, 611 pp.
- Schopf, P. S. and M. A. Cane, 1983: On equatorial dynamics, mixed layer physics and sea surface temperature. *J. Phys. Oceanogr.*, **13**, 917-935.
- Semnter, A. J. and W. R. Holland, 1980: Numerical simulation of equatorial ocean circulation. Part I: A basic case in turbulent equilibrium. *J. Phys. Oceanogr.*, **10**, 667-693.
- Stricherz, J. N., J. J. O'Brien, and D. M. Legler, 1992: *Atlas of Florida State University tropical Pacific winds for TOGA 1966-1985*. Mesoscale Air-Sea Interaction Group Technical Report, Tallahassee, Florida.
- Trenberth, K. E., J. G. Olson, and W. G. Large, 1989: A global ocean wind stress climatology based on ECMWF analyses. Technical note NCAR/TN-338+STR, National Center for Atmospheric Research, Boulder, Colorado, 1-93.

Webster, P. J. and R. Lukas, 1992: TOGA COARE: The coupled ocean-atmosphere response experiment. *Bull. Amer. Meteor. Soc.*, **73**, 1377-1416.

Wyrtki, K., 1975: El Nino -- The dynamic response of the equatorial Pacific Ocean to atmospheric forcing. *J. Phys. Oceanogr.*, **5**, 572-584.

Zhang, R. H. and M. Endoh, 1992: A free surface general circulation model for the tropical Pacific Ocean. *J. Geophys. Res.*, **97**, 11237-11255.

INITIAL DISTRIBUTION LIST

	No. Copies
1. Defense Technical Information Center Cameron Station Alexandria, VA 22304-6145	2
2. Library, Code 52 Naval Postgraduate School Monterey, CA 93943-5000	2
3. Chairman (Code MR/Hy) Department of Meteorology Naval Postgraduate School Monterey, CA 93943-5000	1
4. Chairman (Code OC/Co) Department of Oceanography Naval Postgraduate School Monterey, CA 93943-5000	1
5. Prof. J. T. Murphree (Code MR/Me) Department of Meteorology Naval Postgraduate School Monterey, CA 93943-5000	1
6. Prof. R. W. Garwood (Code OC/Gd) Department of Oceanography Naval Postgraduate School Monterey, CA 93943-5000	1
7. Ms. A. Guest (Code OC/Gt) Department of Oceanography Naval Postgraduate School Monterey, CA 93943-5000	1
8. LT Claudia S. Whitney NAVOCEANCOMDET Box 154 NAS Cecil Field, FL 32215-0154	1
9. Director Naval Oceanography Division Naval Observatory 34th and Massachusetts Avenue NW Washington, DC 20390	1

10. Commanding Officer 1
Naval Oceanographic Office
Stennis Space Center, MS 39522-5001
11. Superintendent 1
Naval Research Laboratory
NPS Annex
Monterey, CA 93943-5006

144-403

Thesis

W5625 Whitney

C.1 Modeling the tropical
ocean response to westerly
wind forcing.

Thesis

W5625 Whitney

C.1 Modeling the tropical
ocean response to westerly
wind forcing.

DUDLEY KNOX LIBRARY



3 2768 00036277 6